

The Red-Giant Branch Bump: towards a better understanding of the physical nature and efficiency of convective boundary mixing

by

Saniya Khan



A thesis submitted to the
University of Birmingham
for the degree of
DOCTOR OF PHILOSOPHY

Sun, Stars and Exoplanets
School of Physics and Astronomy
University of Birmingham
Birmingham, B15 2TT

July 2021

UNIVERSITY OF
BIRMINGHAM

University of Birmingham Research Archive

e-theses repository

This unpublished thesis/dissertation is copyright of the author and/or third parties. The intellectual property rights of the author or third parties in respect of this work are as defined by The Copyright Designs and Patents Act 1988 or as modified by any successor legislation.

Any use made of information contained in this thesis/dissertation must be in accordance with that legislation and must be properly acknowledged. Further distribution or reproduction in any format is prohibited without the permission of the copyright holder.

Abstract

Several uncertainties are still affecting our ability to model low-mass stars today — with significant implications on studies of exoplanetary systems, and of stellar populations and Galactic evolution. One of these is related to convection, and more specifically to convective overshooting processes which transport chemical elements beyond the formal convective boundary defined using the Schwarzschild criterion. In this respect, the luminosity of the red-giant branch bump can be used as a diagnostic for extra-mixing processes occurring below the envelopes of red-giant stars, and this has been well-studied in former investigations of Galactic globular clusters.

In this thesis, we use a novel set of constraints from asteroseismology to revisit the red-giant branch bump in field stars observed by *Kepler* and APOGEE. We also extend the analysis to clusters in our Galaxy and in the Magellanic Clouds, in order to work towards an envelope overshooting calibration applicable in a wide range of masses and metallicities. Both studies seem to indicate that the extra-mixing efficiency increases as we move towards lower metallicities. This offers interesting leads that are potentially relevant to test convection as a physical process.

Because such tests of stellar evolution theory rely strongly on the accuracy of asteroseismic constraints, we also dedicated a substantial part of the work to comparing asteroseismically-derived parallaxes with estimates from *Gaia* DR2 and EDR3. These analyses provide new estimates of the *Gaia* parallax zero-point in the *Kepler*, *K2*, and TESS fields. They also demonstrate the strong potential of asteroseismology as a way to derive stellar fundamental parameters.

TO RILAKKUMA

Thanks and Acknowledgements

Cette thèse est le fruit d'un travail de 3 ans et 9 mois à l'Université de Birmingham, en théorie — mais, en pratique, plutôt 2 ans et 9 mois à Birmingham, suivis d'une année entière en télétravail à Paris.

Il me vient naturellement à l'esprit de remercier tous mes collègues du groupe SASP (anciennement HiROS) à Birmingham : Bill, Alex D, Eddie, Mat, Tom, Warrick, Guy, Oli, Amaury, Vedad, Yvonne, Ben, Rachel, Steve, Andy, Walter, Matt, George, Ted, Martin, Fiorenzo, Alex L, Tanda, Emma, Andreas, Lindsey, Emily, Lalitha, et Daniel (approximativement par ordre d'apparition).

En particulier, je voudrais remercier Gaël pour une première année de thèse enjouée, et pour m'avoir transmis l'accent belge (bien que je l'aie perdu aujourd'hui !). Merci d'avoir continué à suivre mon parcours, même après ton départ.

Je remercie également Josefina pour les nombreux échanges quasiment nocturnes, que ce soit au bureau (pour déboguer MESA...), en voiture, ou à Laghi's Deli. Cela a été une chance inouïe que de pouvoir approfondir mes connaissances en évolution stellaire à tes côtés.

Mon travail et mes connaissances ont aussi été enrichis, directement ou indirectement, grâce aux rencontres et contacts que j'ai maintenus au-delà de Birmingham.

Il va de soi que je remercie Benoît pour avoir toujours suivi de près ou de loin mes péripéties outre-Manche. Merci d'avoir continuellement pris de mes nouvelles,

même lorsque l'isolement me rendait silencieuse.

Un chaleureux merci à Arlette d'être une grande source d'inspiration, et de faire vivre la science par son enthousiasme et sa passion.

Merci à Leo de m'avoir accueillie pour trois mois fantastiques à Padoue, qui m'ont permis de rencontrer des personnes exceptionnelles : Neven, José, Giorgio, Matilde, Cote, Elena G(reek), Yann, Elena M(exican), Alessandro, et Daniele.

Une pensée pour Anthony, Kévin, David, et Frédéric qui ont rendu la compréhension des subtilités de la mission *Gaia* moins inaccessible.

Je souhaiterais également remercier Raphael de nous avoir fait profiter de ses lumières concernant l'applicabilité des paramétrisations de mélange, lors du passage entre les simulations 2D/3D et les modèles d'évolution stellaire 1D.

Tout récemment, je tiens à remercier les organisateurs du Kavli Summer Program in Astrophysics 2021, qui ont su rendre cette expérience agréable et bénéfique malgré le côté virtuel ; et, tout particulièrement, Pascale qui me partage son savoir théorique et me permet de concrétiser un désir de longue date : me rapprocher des simulations hydrodynamiques ! Je perçois cette école virtuelle comme une belle conclusion à ma thèse, et je me rends compte que les étoiles ont encore tant de secrets pour moi.

Il y a bien évidemment quelqu'un qui m'a accompagnée pendant toute cette thèse, alors mille mercis à Andrea de m'avoir suivie depuis mon stage de Master 1 en 2016. Faire cette thèse à Birmingham m'est paru comme une évidence. L'attrait de la ville de Birmingham en elle-même a rapidement disparu au bout de quelques mois. Mais ces 3 années et 9 mois de thèse ont été très enrichissantes, tant sur le plan scientifique que personnel. Tu m'as donné l'opportunité de travailler sur des sujets variés, et par la même occasion de rencontrer des collaborateurs d'horizons diversifiés. J'ai aussi eu la chance d'être assez libre et indépendante dans mes décisions, que ce soit pour le choix de mes projets ou de mes postdocs ; tu as toujours été à

l'écoute pour me partager des conseils avisés, tout en me laissant maîtresse de mes décisions. Merci d'avoir été remarquablement compréhensif lors de la transition en télétravail, et d'avoir maintenu nos discussions régulières, brisant la monotonie de ces nombreux mois d'isolement durant le début de la crise sanitaire. Pour terminer, je te remercie d'avoir fait de moi l'astrophysicienne que je suis aujourd'hui.

Cette thèse est aussi le fruit de mon environnement, alors merci à Marine de m'avoir soutenue dans mes projets et qui, malgré la distance et le temps qui s'écoule, n'a jamais eu besoin de longues descriptions pour lire l'atmosphère et mes états d'âme. Je remercie Paul, Adrian, et Romain, d'avoir eux aussi donné vie à cette thèse en suivant l'évolution de mes travaux et recherches. Une mention spéciale à Gatts77, LexyBird70, et VirKouik, pour avoir égayé cette dernière année de confinement ; nos parfois longues et tardives sessions m'ont donné la force de toujours fixer l'horizon.

Je remercie ma mère, ma soeur, et mes frères de toujours avoir été présents, et d'avoir trouvé que j'étais une bonne excuse pour planifier des voyages à Birmingham. Merci infiniment à Flavienne d'être fière de moi comme une maman le serait.

Enfin, un grand merci à la personne qui m'accompagne depuis mes débuts en tant que (pas encore astro-) physicienne, qui m'a toujours encouragée à poursuivre mes rêves, qui est venu éclaircir le temps gris et pluvieux de Birmingham à de nombreuses reprises, qui me prépare les meilleurs repas dignes d'un restaurant étoilé après mes sessions de travail nocturnes, qui soigne mes états d'angoisse et m'apprend à être fière de moi et de ce que j'accomplis, et qui est encore à mes côtés aujourd'hui pour notre nouvelle vie à Genève. Je t'aime, Virgile.

Contents

Abstract	ii
Dedication	iii
Thanks and Acknowledgements	iv
List of Figures	ix
List of Tables	xv
Acronyms	xvi
1 Introduction and Thesis Plan	1
2 Stellar Structure and Evolution of Low-Mass Stars	5
2.1 Evolutionary Path of Low-Mass Stars in a Nutshell	6
2.2 Some Uncertainties in Current 1D Stellar Evolution Models of Low-Mass Stars	10
2.2.1 Convection	10
2.2.2 Uncertainties From Poorly-Constrained Chemical Composition Parameters	14
2.2.3 From Uncertain Physical Processes	15
2.2.4 From Numerical Implementation	15
3 Asteroseismology of Solar-Like Oscillators	17
3.1 Observations	18
3.2 Theory of Stellar Oscillations	19
3.2.1 Adiabatic Approximation	19
3.2.2 Solar-Like Oscillations	20
3.3 Asteroseismic Diagnostics	22
3.3.1 Global Asteroseismic Observables	23
3.3.2 Asteroseismic Methods: Scaling Relations and Grid-Based Modelling	28
4 The Red-Giant Branch Bump	31
4.1 The Red-Giant Branch Bump	31
4.1.1 Detailed Reason Behind the Occurrence of the Red-Giant Branch Bump	32

4.1.2	Characteristic Properties	34
4.2	The Red-Giant Branch Bump as Seen by <i>Kepler</i> and <i>APOGEE</i>	40
4.2.1	Introduction	41
4.2.2	Observational and Theoretical Framework	43
4.2.3	Determination of the RGB Bump Location	46
4.2.4	Results	47
4.2.5	Conclusions	52
4.3	The Red-Giant Branch Bump as Seen by Star Clusters	54
4.3.1	Introduction	54
4.3.2	Observational and Theoretical Framework	55
4.3.3	Methods	59
4.3.4	Preliminary Results	67
4.3.5	Future plans	68
4.4	Possible Interpretations for the Overshooting Trend with Metallicity	70
4.4.1	Entrainment Law	71
4.4.2	Pratt et al. (2017) Diffusion Coefficient	73
5	Asteroseismology and <i>Gaia</i>	74
5.1	<i>Gaia</i> DR2 Parallax Zero-Point in the <i>Kepler/K2</i> fields	75
5.1.1	Introduction	75
5.1.2	Observational Framework	79
5.1.3	Detailed Objectives	82
5.1.4	Analysis of the <i>Kepler</i> Field	89
5.1.5	Positional Dependence of the Parallax Zero-Point	104
5.1.6	Joint Calibration of the Seismic Scaling Relations and of the Zero-Point in the <i>Gaia</i> Parallaxes	109
5.1.7	Conclusions	114
5.2	<i>Gaia</i> EDR3 Parallax Zero-Point in the <i>Kepler/K2</i> and TESS-SCVZ fields	116
5.2.1	Introduction	116
5.2.2	Observational Framework	118
5.2.3	Analysis of the <i>Kepler</i> field	119
5.2.4	Analysis of the <i>K2</i> fields	119
5.2.5	Analysis of the TESS-SCVZ field	121
5.2.6	A Global Picture of the <i>Gaia</i> EDR3 Parallax Zero-Point	123
5.2.7	Conclusions	124
6	Conclusions and Future Prospects	129
	Bibliography	133
	Publications and Contributions	143

List of Figures

- 2.1 Left: Kippenhahn diagram for a model of a star with a mass $M = 1.40 M_{\odot}$ and a metallicity $[M/H] = 0.0$ dex, showing the evolution of the stellar structure as a function of age. The space occupied by the convective region is shown in black; while that of the hydrogen-burning shell is in red. The grey dashed line indicates the maximum depth of the convective envelope. Right: Mean molecular weight profile for the same star, at the time of maximum penetration of the convection. The position of the hydrogen-burning shell, at that time, is indicated by the red dashed line. The density changes by about a factor two between the two sides of the hydrogen-burning shell. . . . 9
- 2.2 Hertzsprung-Russell diagram showing models of stars with: $M = 1.0 M_{\odot}$, $[M/H] = 0.0$ dex (black), $M = 1.4 M_{\odot}$, $[M/H] = 0.0$ dex (green), and $M = 1.0 M_{\odot}$, $[M/H] = -1.0$ dex (red). The solid lines correspond to the evolution from the main sequence to the red-giant branch tip, while the dashed lines illustrate the core-helium burning phase. . . . 10
- 3.1 Schematic Hertzsprung-Russell diagram showing the location of several classes of pulsating stars. The solid line indicates the zero-age main sequence. The dot-dashed lines show different features: evolutionary tracks, the horizontal branch, and the white-dwarf cooling curve. The current study focuses on solar-like oscillations. Figure taken from [Mosser \(2015\)](#); [Aerts et al. \(2010\)](#). . . . 18
- 3.2 Solar oscillation spectrum with data from SOHO/GOLF ([Gabriel et al., 1995](#)). Figure taken from [Mosser \(2015\)](#). . . . 21
- 3.3 Power spectrum for KIC 12008916, where the amplitude is normalised to parts per million (ppm). Red symbols represent the radial modes ($\ell = 0$). Examples of the large separation $\langle \Delta \nu \rangle = \nu_{n+1, \ell=0} - \nu_{n, \ell=0}$ between radial modes are shown. The oscillation envelope of power is illustrated and its maximum is labelled as ν_{\max} . Figure taken from [Davies & Miglio \(2016\)](#). . . . 23
- 3.4 Solar squared sound-speed (left) and temperature (right) profiles. The dotted vertical line shows the transition between the radiative interior and the adiabatic envelope. Figures taken from [Mosser \(2015\)](#). 24
- 3.5 Acoustic cut-off frequency (solid line) as a function of the normalised radius, in the outermost parts of a model of the present Sun. Figure taken from [Christensen-Dalsgaard's lecture notes on stellar oscillations](#). 25

3.6	Correction to be applied to the $\langle \Delta\nu \rangle$ scaling relation as a function of ν_{\max} , for a solar metallicity ($[\text{Fe}/\text{H}] = 0.0$). The coloured lines correspond to evolutionary tracks with different masses, from 0.80 to 2.50 M_{\odot} . Figure taken from Rodrigues et al. (2017)	29
4.1	Colour-magnitude diagram (left) and luminosity function, i.e. number of stars per luminosity / magnitude interval (right) of 47 Tuc. Figure taken from Nataf et al. (2013)	32
4.2	Hertzsprung-Russell diagram for a model of a star with a mass $M = 1.40 M_{\odot}$ and a metallicity $[\text{M}/\text{H}] = 0.0$ dex. The inset is zooming on the location of the red-giant branch bump.	33
4.3	Left: $T_{\text{eff}} - \nu_{\max}$ diagram, zoomed near the location of the bump. The coloured points correspond to the data (see Sec. 4.2.2) with a mass $M \in [0.9, 1.1] M_{\odot}$, and different metallicity ranges: $[-0.5, -0.3]$ (brown), $[-0.3, -0.1]$ (purple), $[-0.1, +0.1]$ (grey), $[+0.1, +0.3]$ dex (red). Evolutionary tracks computed using MESA (see Sec. 4.2.2) with $M = 1.0 M_{\odot}$, and $[\text{M}/\text{H}] = -0.4, -0.2, 0.0, +0.2$ dex (from left to right), without envelope overshooting, are shown in black. Right: same diagram with a metallicity $[\text{M}/\text{H}] \in [-0.1, +0.1]$ dex, and different mass ranges: $[0.9, 1.1]$ (blue), $[1.1, 1.3]$ (orange), $[1.3, 1.5]$ (green), $[1.5, 1.7] M_{\odot}$ (pink). Evolutionary tracks with $[\text{M}/\text{H}] = 0.0$ dex, and $M = 1.0, 1.2, 1.4, 1.6 M_{\odot}$ (from right to left), without envelope overshooting, are shown in black.	43
4.4	Probability functions applied to our dataset in the $\log T_{\text{eff}} - \log \nu_{\max}$ (left) and $\log T_{\text{eff}} - \log \langle \Delta\nu \rangle$ (right) planes; with $0.9 \leq M \leq 1.1 M_{\odot}$ and $-0.1 \leq [\text{M}/\text{H}] \leq +0.1$ dex. 2D histograms are plotted, where the colour scale indicates the number of stars and the ellipses show the location of the bump, as determined by the mixture model technique. 1D histograms of $\log \nu_{\max}$ (or $\log \langle \Delta\nu \rangle$) and $\log T_{\text{eff}}$ are also shown in black in the bottom and right plots, respectively. The two components of the RGBb bivariate Gaussian are displayed with blue lines. The brown line correspond to the RGB outliers' rising exponential in $\log \nu_{\max}$ (or $\log \langle \Delta\nu \rangle$); while the red dashed line shows the linear term modelling the RGB background. The small plot at the bottom right corner depicts the difference between $\log T_{\text{eff}}$ and the RGB linear term, hereby illustrating the normal scatter.	46
4.5	Location of the RGBb in ν_{\max} (left) and in $\langle \Delta\nu \rangle$ (right), in our dataset (black; see Sec. 4.2.2), and its corresponding 68% credible region, and simple synthetic populations with different envelope overshooting efficiencies: $\alpha_{\text{ov,env}} = 0.00$ (yellow), $\alpha_{\text{ov,env}} = 0.025$ (purple), and $\alpha_{\text{ov,env}} = 0.05$ (red); as a function of mass, for different metallicity ranges: $[-0.5, -0.3]$, $[-0.3, -0.1]$, $[-0.1, +0.1]$, and $[+0.1, +0.3]$ dex (from top to bottom). The background bands indicate the mass bin, in which the bump position has been estimated.	49
4.6	Same as Fig. 4.5; as a function of metallicity, for different mass ranges: $[0.9, 1.1]$, $[1.1, 1.3]$, and $[1.3, 1.5] M_{\odot}$ (from top to bottom).	50

4.7	Heatmap illustrating the relative variations (%) of the bump's location in ν_{\max} and $\langle \Delta\nu \rangle$, with two different sets of default parameters. Full details are provided in the text.	51
4.8	Colour-magnitude diagrams for NGC 0362 (top panel) and NGC 6441 (bottom panel) with red-giant branch stars in blue and core-helium burning stars in red, circled by their respective selection boxes. The number of red-giant branch and red clump stars is indicated in each individual panel, with the same colour. From left to right, we move from ultraviolet to near-infrared filters.	60
4.9	Left: Probability functions applied to NGC 0362 in the F606W - (F606W-F814W) plane. 2D histograms are plotted, where the colour scale indicates the number of stars and the ellipses show the location of the bump, as determined by the mixture model technique. 1D histograms of F606W and (F606W-F814W) are also shown in black in the bottom and right plots, respectively. The two components of the RGBb bivariate Gaussian are displayed with blue lines. The brown line correspond to the RGB outliers' rising exponential in F606W; while the red dashed line shows the linear term modelling the RGB background. The small plot at the bottom right corner depicts the difference between (F606W-F814W) and the RGB linear term, hereby illustrating the normal scatter. Right: Final colour-magnitude diagram for RGB stars, with the colour scale indicating the RGBb membership probability.	61
4.10	Colour-magnitude diagram zoomed near the horizontal branch for NGC 0362. The observations are shown with grey points. The black line shows the simulated zero-age horizontal branch, and each circle corresponds to a specific mass-loss efficiency. The circles at the brighter (fainter) end corresponds to lower (high) mass-loss efficiencies.	63
4.11	Colour-magnitude diagram zoomed near the turn off for NGC 0362. The observations are shown with grey points. The turn-off fiducial sequence is shown in black, with the vertical dashed line indicating the turn-off colour. The upper main-sequence fiducial sequence is displayed in red, with the vertical and horizontal dashed lines defining the colour (redder by 0.05 than the TO colour) and magnitude of the upper MS point, respectively.	64
4.12	Colour-magnitude diagram zoomed near the turn off for NGC 0362. The observations are shown with grey points. The coloured lines correspond to different isochrones, that have been shifted to match the observed turn-off colour.	64
4.13	Colour-magnitude diagram for Galactic globular clusters. The observations are shown with grey points. The coloured lines correspond to the final isochrone that best fits the observed CMD, from the upper main-sequence to the horizontal branch. (1/3)	65
4.14	Same as Fig. 4.13. (2/3)	66
4.15	Same as Fig. 4.13. (3/3)	67

4.16	Absolute magnitude of the RGBb in the V -band, in our dataset of Galactic globular clusters (red), and best-fit isochrones using PARSEC tracks (black), as a function of metallicity. Data from Nataf et al. (2013) are also shown in grey for comparison.	68
4.17	Squared Brunt-Väisälä frequency profiles for a $1.40 M_{\odot}$ model, with different metallicities: -0.4 (brown), -0.2 (purple), 0.0 (grey), and $+0.2$ dex (red). The x -axis has been normalised by the position of the base of the convective envelope, indicated by the black dashed line.	72
5.1	Relative difference in $\langle \Delta\nu \rangle$, $\delta(\Delta\nu)/\Delta\nu = (\Delta\nu_{\text{other}} - \Delta\nu_{\text{D16}})/\Delta\nu_{\text{D16}}$, between individual frequencies following Davies et al. (2016) (D16) and another method, as a function of ν_{max} as estimated by Mosser et al. (2011a) . The comparison is done with Mosser et al. (2011a) (M11; top) and Yu et al. (2018) (Y18; bottom). RGB and RC stars are in blue and red, respectively. Here, $\Delta\nu$ is used, instead of $\langle \Delta\nu \rangle$, to simplify the notation.	82
5.2	Parallax difference $\varpi_{\text{Gaia}} - \varpi_{\text{seismo}}$ for RGB stars, with the asteroseismic parallax derived from the raw scaling relations, as a function of ϖ_{Gaia} , G , ν_{max} , $G_{\text{BP}} - G_{\text{RP}}$, M_{PARAM} , and $[\text{Fe}/\text{H}]$. The distribution of the N realisations of the RANSAC algorithm is indicated by the grey-shaded region and the yellow line displays the average linear fit, for which the relation is given at the top of each subplot. The values of \bar{X} for RGB stars are given in Table 5.1. The summary statistics are: $(\overline{\Delta\varpi})_{\text{m}} = -6.2 \pm 1.3 \mu\text{as}$, $(\overline{\Delta\varpi})_{\text{w}} = -7.9 \pm 0.8 \mu\text{as}$, and $z = 0.89$. The black dashed lines correspond to the average linear fits when a ± 100 K shift in T_{eff} is applied. An increase in ϖ_{Gaia} corresponds to a decrease in distance, while an increase in G is equivalent to an increase in distance (at fixed absolute magnitude): this means that the two top panels possibly show the same trend but in the opposite direction.	86
5.3	Same as Fig. 5.2 for RC stars. The values of \bar{X} for RC stars are given in Table 5.1. The summary statistics are: $(\overline{\Delta\varpi})_{\text{m}} = -34.6 \pm 1.4 \mu\text{as}$, $(\overline{\Delta\varpi})_{\text{w}} = -35.6 \pm 0.9 \mu\text{as}$, and $z = 0.84$	87
5.4	ϖ_{Gaia} as a function of ϖ_{scaling} (left) and ϖ_{PARAM} (right), for RGB (top) and RC (bottom) stars. The yellow line displays the linear fit, averaged over N realisations, for which the relation is given at the top of each subplot. The black dashed line indicates the 1:1 relation.	89
5.5	Renormalised Unit Weight Error distribution for <i>Kepler</i> RGB and RC stars. The vertical dashed line indicates the threshold adopted: $\text{RUWE} \leq 1.2$	91
5.6	Absolute difference in A_K between the Green et al. (2015) map (left) / RJCE method (right) and PARAM, as a function of PARAM's extinctions.	93
5.7	Same as Fig. 5.2 with the asteroseismic parallax derived from the scaling relations, where a 2.7% correction factor has been applied to the $\langle \Delta\nu \rangle$ scaling. The summary statistics are: $(\overline{\Delta\varpi})_{\text{m}} = -35.8 \pm 1.3 \mu\text{as}$, $(\overline{\Delta\varpi})_{\text{w}} = -35.5 \pm 0.8 \mu\text{as}$, and $z = 0.88$	94

5.8	Same as Fig. 5.2 with the asteroseismic parallax derived from PARAM (Rodrigues et al., 2017). The summary statistics are: $(\overline{\Delta\varpi})_m = -51.4 \pm 1.0 \mu\text{as}$, $(\overline{\Delta\varpi})_w = -51.7 \pm 0.8 \mu\text{as}$, and $z = 1.24$	96
5.9	Same as Fig. 5.8 for RC stars. The summary statistics are: $(\overline{\Delta\varpi})_m = -48.3 \pm 1.1 \mu\text{as}$, $(\overline{\Delta\varpi})_w = -47.9 \pm 0.9 \mu\text{as}$, and $z = 1.23$	96
5.10	Slope of the various $\varpi_{\text{seismo}} - \varpi_{\text{Gaia}}$ relations — using raw scaling relations (crosses; Sect. 5.1.4), a corrected $\langle\Delta\nu\rangle$ scaling relation (circles; Sect. 5.1.4), and PARAM (diamonds; Sect. 5.1.4) — as a function of the weighted average parallax difference for RGB (blue) and RC (red) stars. For RC stars, the line is extended to lower offset values for a better visualisation of how the slope compares with RGB stars when using scaling relations at face value.	99
5.11	ϖ_{Gaia} as a function of ϖ_{scaling} (left) and ϖ_{PARAM} (right), for red giants in the <i>K2</i> Campaign 3 (top) and 6 (bottom) fields. The yellow line displays the linear fit, averaged over N realisations, for which the relation is given at the top of each subplot. The black dashed line indicates the 1:1 relation. The summary statistics are: $(\overline{\Delta\varpi})_m = 28.9 \pm 5.2 \mu\text{as}$, $(\overline{\Delta\varpi})_w = 24.6 \pm 4.0 \mu\text{as}$, and $z = 1.16$ for C3 (scaling); $(\overline{\Delta\varpi})_m = 11.9 \pm 3.6 \mu\text{as}$, $(\overline{\Delta\varpi})_w = 9.5 \pm 2.6 \mu\text{as}$, and $z = 1.01$ for C6 (scaling); $(\overline{\Delta\varpi})_m = -8.1 \pm 4.4 \mu\text{as}$, $(\overline{\Delta\varpi})_w = -6.4 \pm 3.8 \mu\text{as}$, and $z = 1.30$ for C3 (PARAM); $(\overline{\Delta\varpi})_m = -18.6 \pm 3.3 \mu\text{as}$, $(\overline{\Delta\varpi})_w = -16.9 \pm 2.4 \mu\text{as}$, and $z = 1.11$ for C6 (PARAM).	102
5.12	Distribution of the parallax uncertainties in <i>Gaia</i> DR2 (top) and in PARAM (bottom) for the <i>Kepler</i> (red), C3 (orange), and C6 (purple) fields.	103
5.13	Sky map in ecliptic coordinates of the median parallaxes for the full quasar sample, showing large-scale variations of the parallax zero-point. The <i>Kepler</i> (red), C3 (orange), and C6 (purple) fields are displayed. Median values are calculated in cells of $3.7 \times 3.7 \text{ deg}^2$	104
5.14	Weighted average parallax of the quasars selected within a given radius around the central coordinates of the <i>Kepler</i> (red), C3 (orange), and C6 (purple) fields. The black dashed line indicates the average radius of the fields.	105
5.15	Colour-Magnitude Diagrams (CMDs; left and middle) and absolute magnitude M_K normalised histograms (right), where M_K is estimated by means of the <i>Gaia</i> parallax at face value for the <i>Kepler</i> (grey) and C3 (orange) fields. Another CMD, including a shift in parallax, is shown for <i>Kepler</i> (red). We removed stars having a parallax with a relative error above 10% for <i>Kepler</i> , and 15% for C3. The black dashed lines indicate the expected range of values for the magnitude of the clump in the <i>K</i> band.	108
5.16	ϖ_{Gaia} as a function of ν_{max} for RGB (blue) and RC (red) stars in the <i>Kepler</i> sample.	110

5.17	Coefficients (left) and offsets (right) determined via our two-step calibration methodology for RGB (blue) and RC (red) stars, as a function of ν_{\max}	111
5.18	Trends of the parallax difference $\varpi_{\text{EDR3}} - \varpi_{\text{PARAM}}$ with the ecliptic latitude, the G magnitude, the effective wavenumber, the frequency of maximum oscillation, the mass inferred from PARAM, and the metallicity, without (top panel) and with the inclusion of the zero-point correction (bottom panel). The colour scale indicates the mass from PARAM.	120
5.19	Trends of the parallax difference $\varpi_{\text{EDR3}} - \varpi_{\text{PARAM}}$ with the ecliptic latitude, the G magnitude, the effective wavenumber, the frequency of maximum oscillation, the mass inferred from PARAM, and the metallicity, using APOGEE (top panel) or SkyMapper constraints (bottom panel). The colour scale indicates the mass from PARAM.	122
5.20	Top panel: Parallax offsets as estimated from asteroseismology (red circles), the Lindegren et al. (2021b) zero-point correction model (green diamonds), and quasars in each field (grey squares), as a function of the sine of the galactic latitude. Bottom panel: K -magnitude of the red clump as estimated from asteroseismic samples (red circles), <i>Gaia</i> EDR3 samples without (yellow stars) and with the L21 correction (orange stars), and TRILEGAL synthetic populations (purple diamonds), as a function of the sine of the galactic latitude. The black dashed lines show the expected range of values for the magnitude of the clump in the K band. A larger circle (square) size indicates a greater number of stars in the asteroseismic (quasars) samples.	125
5.21	Top left: Sky map showing the location of the C15 field. Top right: CMD with the colour scale showing the density of stars. Bottom: Three different CMDs with the absolute magnitude calculated: by inverting the raw <i>Gaia</i> parallax (left), and adding the extinction (middle), or by applying the L21 correction (right); and the corresponding histograms and KDEs. The brown and green lines show the modes that are taken as references for the magnitude of the clump. The black dashed lines indicate the range of magnitudes that is expected from models.	126
5.22	Hertzsprung-Russell Diagrams of red-giant stars in the <i>Kepler</i> field, using distance estimates from <i>Gaia</i> DR2 (left panel), <i>Gaia</i> EDR3 (middle panel), and PARAM (right panel). The colour scale indicates the mass as inferred from PARAM.	128

List of Tables

4.1	Properties of the Galactic globular clusters considered in this study: age, metallicity, $[\alpha/\text{Fe}]$, reddening, distance, and mass.	58
4.2	Properties of the Magellanic Clouds clusters considered in this study: age, metallicity, location (Large or Small Magellanic Cloud), notes on possible specificities of the clusters, and references providing the age and metallicity values (see references therein for the actual sources). .	59
5.1	Values of \bar{X} (mean value of the stellar parameter X) for RGB (top) and RC stars (bottom).	85

Acronyms

CHeB	Core-Helium burning
CMD	Colour-Magnitude Diagram
GC	Globular Cluster
HB	Horizontal Branch
HRD	Hertzsprung-Russell Diagram
MLT	Mixing-Length Theory
MS	Main Sequence
MSTO	Main Sequence Turn-Off
RGB	Red-Giant Branch
RGBb	Red-Giant Branch bump
ZAHB	Zero-Age Horizontal Branch

Chapter 1

Introduction and Thesis Plan

Nowadays, our understanding of the general evolution of low-mass stars ($M \lesssim 2 M_{\odot}$) may be considered as fairly advanced. Stellar evolution codes are able to model the complete evolution of such stars, from the pre-main sequence to the white dwarf stage. However, if we move from the broad picture to more detailed aspects of the evolution, several weaknesses appear at various evolutionary stages.

One long-standing and crucial deficiency (though not the only one) has to do with the treatment of convection in stellar interiors, which requires the introduction of various approximations. In particular, the occurrence and efficiency of mixing processes beyond formal convective boundaries is poorly known, albeit it directly affects predictions of stellar evolutionary timescales, nucleosynthesis and photospheric abundances (Bressan et al., 2015; Salaris & Cassisi, 2017). Commonly used approaches are simplified parameterisations where the size of the extra-mixed region is left as a free parameter (e.g. Renzini, 1987).

These (uncertain) additional mixing processes affect both e.g. the extent of convective cores (hence stellar lifetimes; Maeder, 1975) and the depth of convective envelopes in giant stars (hence surface abundances). The red-giant branch provides an observational means to constrain these processes, via the red-giant branch bump (Alongi et al., 1991). The latter corresponds to a temporary drop in luminosity as a star evolves on the red-giant branch, leading to a local maximum in the luminosity

function. The occurrence of the bump is related to the hydrogen-burning shell approaching and eventually advancing through the chemical composition gradient left by the first dredge-up, i.e. a phase during which the convective envelope penetrates into deeper layers of the star until a maximum penetration depth, before receding towards the surface. Thus, one can use the luminosity of the bump as a calibrator for extra-mixing processes — the inclusion of overshooting below the convective envelope moves the discontinuity deeper into the star, hence it is met earlier by the hydrogen-burning shell and the bump has a fainter luminosity.

While most studies of the red-giant branch bump were restricted to Galactic globular clusters (e.g. [Di Cecco et al., 2010](#); [Cassisi et al., 2011](#); [Troisi et al., 2011](#)), asteroseismology — the study of stellar pulsations — offers a unique window into the interiors of low-mass stars, with possibilities to probe the internal structure, physical processes, and evolutionary state of stars (see reviews by [Chaplin & Miglio, 2013](#); [Hekker & Christensen-Dalsgaard, 2017](#); [García & Ballot, 2019](#)). Using high-precision long (months) photometric time series, one can detect solar-like oscillations in dwarfs (few, nearby) and giants (tens of thousands). The detected modes can be combined with spectroscopic data to infer radii as precise as a few percent (also masses and, hence, ages). Thus, in this work, we leverage on this novel set of constraints to stress test models of stellar evolution, and more specifically convective boundary mixing processes associated with the luminosity of the red-giant branch bump in field stars. Extending the study of the red-giant branch bump to different stellar populations, such as Galactic globular clusters and Magellanic Clouds clusters, will lead to an envelope overshooting calibration applicable in a wide range of masses and metallicities. By linking all these results with recent advances in 2D/3D hydrodynamical simulations (see, e.g., [Pratt et al., 2017](#); [Cristini et al., 2019](#)), we are gradually working towards a more in-depth physical picture of the occurrence and efficiency of convective boundary mixing in red-giant branch stars.

Since the tests of stellar evolution theory presented in the thesis rely strongly on

the accuracy of asteroseismic constraints, I dedicated a substantial part of the work to testing seismically-inferred stellar properties against independent constraints. This can be done by comparing asteroseismic masses and radii with independent measurements from, e.g., clusters and eclipsing binaries (e.g. [Handberg et al., 2017](#); [Brogaard et al., 2018](#)). In particular, these last few years have witnessed the advent of a new era, marked by the astrometric mission *Gaia* ([Gaia Collaboration et al., 2016a](#)). Fundamental astronomical data, including distances, became available for 2 million sources in *Gaia* DR1, increasing to over 1.4 billion sources in the latest data release, *Gaia* EDR3. *Gaia* had an enormous impact on many fields of astrophysics, leading to a revolution in science from the solar system to the distant universe ([Brown, 2021](#)). Among these, experts in many different fields have compared their distance estimates with *Gaia*, offering a common point of comparison, and hence contributing to the larger question of the cosmic distance ladder (see, e.g., [Riess et al., 2021](#); [Stassun & Torres, 2021](#); [Zinn, 2021](#)). Coupling asteroseismic radii with effective temperatures, we get luminosities that do not rely on any assumption on the mass-luminosity relation. With the addition of information on unreddened apparent brightness, asteroseismic distances are straightforwardly obtained. Hence, comparisons between asteroseismology and *Gaia* are possible, and allow us to constrain biases both in the asteroseismic and the astrometric sides.

The thesis is structured as follows: Chap. 2 broadly summarises our current knowledge about the evolution of low-mass stars up to the core-helium burning phase, and mentions remaining uncertainties in stellar evolution models — and in particular, convection, which is the key thread motivating the studies undertaken during my PhD; Chap. 3 introduces a few concepts behind asteroseismology, a novel method for the estimation of stellar masses, radii, and ages; Chap. 4 presents our studies of the red-giant branch bump, including one that combines asteroseismic and spectroscopic constraints — as opposed to the majority of former analyses being restricted to clusters; Chap. 5 addresses the concern to verify the precision and

accuracy of asteroseismically-derived stellar parameters, which have an impact on stellar evolution studies, with thorough comparisons between distances from asteroseismology and *Gaia*; conclusions and prospects are presented in Chap. 6.

Chapter 2

Stellar Structure and Evolution of Low-Mass Stars

Stellar evolution is a wide field in astrophysics that aims at studying how stars evolve from their birth — from interstellar medium — up until their death — ending their lives as e.g. white dwarfs or supernovae, depending on their initial mass.

Back in the 20th century, our vision of stellar evolution changed considerably, together with our ideas of what a star is. Our knowledge of the structure and evolution of stars is closely linked to the development of physics. Hence, in order to describe stellar evolution, we have to be able to calculate how the stellar interior is constituted, e.g. how do temperature and pressure vary from the outer layers to the centre? how do stars produce, transport, and emit energy? how do they burn and mix chemical elements? Stellar structure and evolution are obviously related. We refer the reader to, e.g., [Gingerich \(1995\)](#); [Cenadelli \(2010\)](#) for historical reviews of stellar evolution.

This chapter briefly reviews the evolution of low-mass stars ($M \lesssim 2 M_{\odot}$). A brief description of the evolutionary and structural changes of low-mass stars is given in Sec. 2.1. We limit ourselves to the few evolutionary phases that are going to be discussed in this thesis, i.e. between the main sequence and the core-helium burning

phase. In Sec. 2.2, we discuss a few uncertainties which are still affecting our ability to model low-mass stars today, with a focus on convection.

For more exhaustive explanations, see, e.g., [Kippenhahn & Weigert \(1990\)](#), [Salaris & Cassisi \(2005\)](#), and [Salaris & Cassisi \(2017\)](#).

2.1 Evolutionary Path of Low-Mass Stars in a Nutshell

Low-mass stars spend a significant amount of their lifetime ($\sim 90\%$) burning hydrogen on the main sequence. In stars with a mass $M \lesssim 1.2 M_{\odot}$ (depending on chemical composition), the main mechanism fusing hydrogen to helium in the radiative core are the pp chains. On the other hand, stars with a slightly higher mass ($M \gtrsim 1.2 M_{\odot}$) develop a small convective core during the central hydrogen-burning phase, the extent of which increases with stellar mass. This is related to the CNO cycle becoming the dominant energy generation process: since the central temperature is higher, the energy production is concentrated towards the centre (the CNO cycle being very sensitive to temperature), and this leads to a steep increase of the radiative gradient — leading to a convectively unstable core, according to the Schwarzschild convective stability criterion ([Schwarzschild, 1906](#)). Nevertheless, for such stars, predictions from models on the precise boundary delimiting the region where convective motions occur, and therefore the extent to which the chemical elements are mixed, are uncertain. Material approaching the Schwarzschild boundary with non-zero momentum can overshoot into the radiative layers below the convective region. Such a phenomenon, referred to as *convective overshooting*, can lead to an increase of the size of the convective core, and extend the burning region (see, e.g., [Maeder, 1975](#), see also Sec. 2.2.1). Because of the additional hydrogen fuel brought to the core, the inclusion of overshooting in stellar models increases the lifetime and luminosity of stars on the main sequence.

When hydrogen is completely depleted in the centre, the star is left with a helium core surrounded by a hydrogen-rich envelope, marking the end of the main sequence. Initially, the temperature in the inner parts of the star is lower than that required for the ignition of helium ($\sim 10^8$ K). In contrast, at the top of the core, the temperature is still high enough for hydrogen-burning to proceed in a thick shell ($\sim 0.2 M_{\odot}$). At the beginning of the subgiant phase, the core mass is much below the Schönberg-Chandrasekhar limit (which defines the upper limit to the mass of an isothermal core which can be in hydrostatic and thermal equilibrium; Schönberg & Chandrasekhar, 1942). Actually, because of the high central density in these low-mass stars, the electron gas in the helium core becomes degenerate and provides the pressure necessary to support the overlying envelope, even when the mass of the inert helium core increases (due to hydrogen being converted into helium in the shell) making the Schönberg-Chandrasekhar limit irrelevant.

During the evolution from the end of the main sequence to the red-giant phase, the shell becomes increasingly thinner as hydrogen is depleted. Due to the expansion and cooling of the outer layers, a large convective region develops in the stellar envelope, as a consequence of the increased opacity at lower temperatures.

At the base of the red-giant branch, the star is constituted of a large ($\sim 80\%$ of the stellar radius) convective envelope on top of a small ($\sim 10\%$ of the stellar radius) radiative core. As stars ascend the red-giant branch, the outer convection zone penetrates deeper into the star — until more than 70% of the total mass is convective — reaching into layers where the chemical composition has been altered by nuclear burning that took place during the main sequence. As a result, part of the chemical elements produced are transported to the surface, increasing the corresponding abundance until the convection reaches a maximum depth in mass. This phase corresponds to the ‘*first dredge-up*’, i.e. chemical elements from deeper layers are dredged up towards the surface. After this phase, the boundary of the

convective envelope recedes towards the surface, because of the steady growth of the helium core which accumulates helium produced by the hydrogen-burning shell. At the same time, the hydrogen-burning shell moves towards more external mass layers that contain fresh hydrogen (see Fig. 2.1, left panel).

A sharp chemical composition gradient, between the homogeneous hydrogen-rich outer layers and the helium-enriched layers below, is left by the convective envelope at its maximum depth, as shown on Fig. 2.1 (right panel). When the hydrogen-burning shell approaches and eventually advances through this discontinuity, the rate at which the star climbs the red-giant branch temporarily drops and even reverses for a while. As a consequence, the star passes three times across a narrow luminosity interval, in which observations have a higher probability of finding stars. One may predict an increase of the star counts, i.e. a peak in the luminosity function, corresponding to the *red-giant branch bump*. The time spent during the red-giant branch bump phase represents about $\sim 5\%$ of the total red-giant branch lifetime.

A large part of my PhD work has been dedicated to the red-giant branch bump, hence more details about this feature in the Hertzsprung-Russell diagram will be given in Chap. 4.

Going forward in the evolution, low-mass stars ignite helium in their central parts through the triple- α reaction, under conditions of strong electron degeneracy, which results in a thermal runaway known as the *helium flash*. Current models predict that the initial and off-centre helium flash is followed by a series of weaker subflashes, that occur closer and closer to the stellar centre, gradually lifting the electron degeneracy. A very large amount of nuclear energy is produced during this short-lived phase: the local luminosity in the helium core reaches a maximum of $\sim 10^{11} L_{\odot}$, which is equivalent to a small galaxy. However, almost none of this energy reaches the surface, as it is absorbed by the non-degenerate layers above.

After the helium flash, low-mass stars move onto a phase of quiet helium burn-

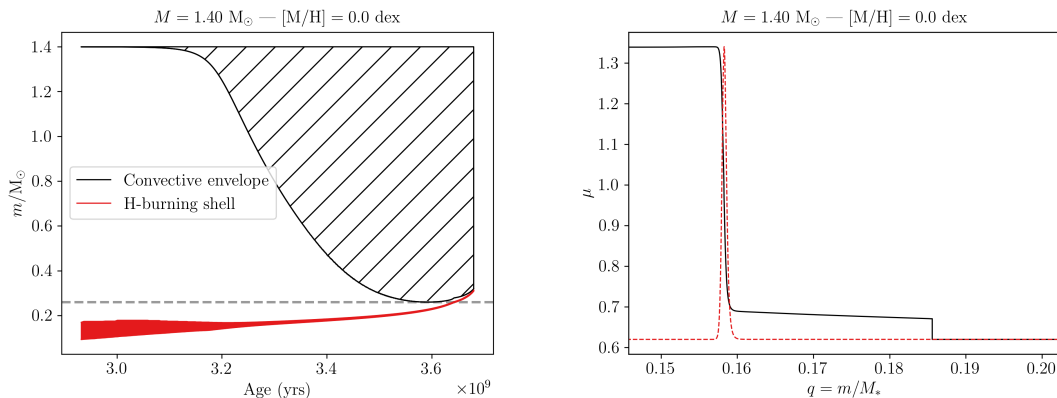


Figure 2.1: Left: Kippenhahn diagram for a model of a star with a mass $M = 1.40 M_{\odot}$ and a metallicity $[M/H] = 0.0 \text{ dex}$, showing the evolution of the stellar structure as a function of age. The space occupied by the convective region is shown in black; while that of the hydrogen-burning shell is in red. The grey dashed line indicates the maximum depth of the convective envelope. Right: Mean molecular weight profile for the same star, at the time of maximum penetration of the convection. The position of the hydrogen-burning shell, at that time, is indicated by the red dashed line. The density changes by about a factor two between the two sides of the hydrogen-burning shell.

ing in the non-degenerate convective core, with very similar helium core masses and, hence, luminosities. Consequently, they settle down on the horizontal branch, with both central helium burning and shell hydrogen burning contributing to the total luminosity budget. Metal-poor stars display an extended horizontal branch, depending on the mass of the hydrogen-rich envelope; while stars with a metallicity close to that of the Sun cluster near the red-giant branch, in what is referred to as the *red clump*. Convective overshooting processes, increasing the size of the core, have also been invoked in the literature for this phase of evolution (see, e.g., [Castellani et al. 1971](#); [Gabriel et al. 2014](#); [Bressan et al. 2015](#) for an overview of these processes; see also Sec. 2.2.1).

A couple of evolutionary tracks are plotted on a Hertzsprung-Russell diagram in Fig. 2.2 to illustrate the different evolutionary phases of low-mass stars described above, as well as the dependence on mass and metallicity. Following the exhaustion of helium in the core, the star enters a phase with two shells, on the asymptotic giant branch. Subsequent evolutionary stages of low-mass stars are beyond the scope of this chapter, and will not be covered here.

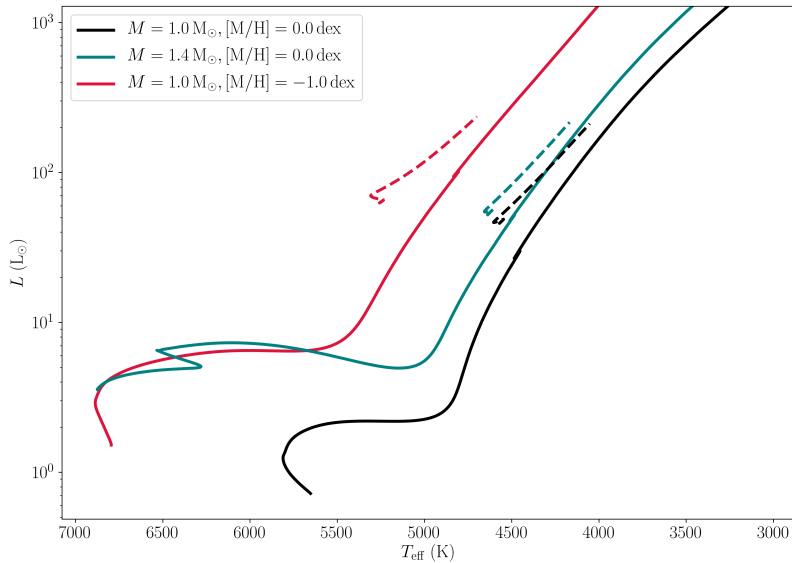


Figure 2.2: Hertzsprung-Russell diagram showing models of stars with: $M = 1.0 M_{\odot}$, $[M/H] = 0.0$ dex (black), $M = 1.4 M_{\odot}$, $[M/H] = 0.0$ dex (green), and $M = 1.0 M_{\odot}$, $[M/H] = -1.0$ dex (red). The solid lines correspond to the evolution from the main sequence to the red-giant branch tip, while the dashed lines illustrate the core-helium burning phase.

2.2 Some Uncertainties in Current 1D Stellar Evolution Models of Low-Mass Stars

Grids of evolutionary tracks play an important role, whether it is in the case of the overshooting calibration via the luminosity bump (Chap. 4) or that of asteroseismic and *Gaia* comparisons (Chap. 5). Uncertainties in stellar evolution models arise both from micro- and macro-physics, and chemical composition. Here, I will only mention convection (Sec. 2.2.1), chemical composition (Sec. 2.2.2), diffusion (Sec. 2.2.3), and numerical issues (Sec. 2.2.4).

2.2.1 Convection

Convection involves macroscopic motions of matter that efficiently transport energy but also chemical elements in the stellar interior. For convection to be included in stellar model computations, one needs to implement a criterion for convection to

occur, as well as a treatment to predict the expressions of the temperature gradient and mixing timescales.

Schwarzschild Criterion

The *Schwarzschild criterion* (Schwarzschild, 1906) is expressed as follows:

$$\nabla_{\text{rad}} > \nabla_{\text{ad}} , \quad (2.1)$$

$$\text{where } \nabla_{\text{rad}} = \left(\frac{d \ln T}{d \ln P} \right)_{\text{rad}} \quad \text{and} \quad \nabla_{\text{ad}} = \left(\frac{d \ln T}{d \ln P} \right)_{\text{ad}} , \quad (2.2)$$

hence it predicts regions to be convective when the radiative temperature gradient ∇_{rad} is larger than the adiabatic temperature gradient ∇_{ad} . For a star in hydrostatic equilibrium, ∇_{rad} describes the temperature gradient when the energy is transported by radiation. While the latter is a spatial derivative, ∇_{ad} is associated with the temperature variation of a gas element adiabatically undergoing a pressure variation.

Mixing-Length Theory

Convection takes place over a large range of lengthscales and timescales, and of pressures, densities and temperatures. It is an intrinsically three-dimensional process and, as such, its inclusion in one-dimensional stellar models can only be done provided that a number of approximations are assumed. The standard model for convection in stellar evolution calculations is the *mixing-length theory*; the most commonly used implementation being from Böhm-Vitense (1958).

In the mixing-length theory picture, convective motions are approximated by hot and cool blobs of gas that move upwards and downwards, respectively. These gas elements are assumed to be travelling over a certain distance before they dissolve in their surroundings. This mean free path is known as the mixing length $\Lambda = \alpha_{\text{MLT}} H_{\text{P}}$, and is proportional to the local pressure scale height H_{P} . The mixing-length parameter, α_{MLT} , is a constant that is usually taken to be equal to the solar-calibrated value. However, several works have pointed at a possible dependence of

α_{MLT} on parameters like luminosity, gravity, and metallicity, based on expectations from 3D simulations and observational evidence (see, e.g., [Trampedach et al., 2014](#); [Magic et al., 2015](#); [Tayar et al., 2017](#); [Salaris et al., 2018](#)).

Overshooting

The Schwarzschild criterion is strictly local, i.e. it can be estimated layer-by-layer without considering what happens in other parts of the star. However, in some cases, non-local effects have to be taken into account. This is, e.g., important for the precise determination of the border of a convective zone, which is located at the layer where $\nabla_{\text{rad}} = \nabla_{\text{ad}}$ if one considers the Schwarzschild criterion. When convective elements come across this boundary, they stop accelerating but they have a non-zero velocity. Therefore, one expects the convective eddies to overshoot by some distance due to their inertia, and additional mixing to be occurring in part of the convectively stable layers.

The occurrence and efficiency of mixing processes beyond formal convective boundaries is poorly known, albeit it directly affects predictions of stellar evolutionary timescales, nucleosynthesis and photospheric abundances ([Bressan et al., 2015](#); [Salaris & Cassisi, 2017](#)). These (uncertain) additional mixing processes affect both e.g. the extent of convective cores (hence stellar lifetimes; [Maeder, 1975](#)) and the depth of convective envelopes in giant stars (hence surface abundances). As illustrated in Chap. 4, the luminosity of the red-giant branch bump can be used as a diagnostic for envelope overshooting happening along the red-giant phase.

Current Treatment of Convective Overshoot in 1D Stellar Evolution Models

Nowadays, different implementations of convective overshooting are available in stellar evolution codes, although they do not necessarily rely on a theoretical background. Commonly used approaches are simplified parameterisations where the size of the extra-mixed region is left as a free parameter (e.g. [Renzini, 1987](#); [Freytag](#)

et al., 1996).

The standard approach is to extend the convectively mixed region beyond the boundary defined by the Schwarzschild criterion. Chemical elements are then mixed instantaneously between the formal convective boundary and the extension fixed at a distance $\lambda_{\text{ov}} H_{\text{P}}$, where λ_{ov} is a free parameter that can be constrained with comparisons of predictions against observations (as implemented in, e.g., Demarque et al., 2004; Pietrinferni et al., 2004; Dotter et al., 2008). Other flavours of instantaneous mixing also exist (e.g. Bressan et al., 1981; VandenBerg et al., 2006).

A diffusive approach to element transport beyond the formal convective boundary also exists, following Freytag et al. (1996) and Herwig (2000). The corresponding diffusion coefficient is given by:

$$D_{\text{ov}} = D_{\text{c}} \exp\left(-\frac{2z}{\alpha_{\text{ov}} H_{\text{P}}}\right), \quad (2.3)$$

where D_{c} is the diffusion coefficient suggested by mixing-length theory near the Schwarzschild boundary ($D_{\text{c}} = 1/3 \Lambda v_{\text{c}} = 1/3 \alpha_{\text{MLT}} H_{\text{P}} v_{\text{c}}$, with the convective velocity v_{c}), H_{P} is the local pressure scale height, z is the distance in the radiative layer with respect to the formal convective boundary, and α_{ov} is a free parameter controlling the overshooting efficiency. The diffusive type of mixing is employed in the MESA stellar evolution code (Paxton et al., 2011), and used in Khan et al. (2018) (Sec. 4.2).

Expected Progress from Hydrodynamical Simulations

In the past, although convective instabilities are intrinsically three-dimensional, the modelling of stellar evolution had been predominantly restricted to 1D because of computational cost. With the now increasing availability of computational resources, 2D and 3D computational fluid dynamics is a gradually expanding field in stellar astrophysics.

However, despite the attractiveness of detailed 2D and 3D simulations, one can-

not simulate the entire evolution of a given star on a hydrodynamic timescale. But it remains possible to construct simple physical models that are consistent with results from 3D simulations and can be used in stellar evolution models. This approach whereby we project 3D to 1D is referred to as ‘321D’ (see, e.g., [Arnett et al., 2015](#)).

Examples of such advanced prescriptions in the case of convective boundary mixing are the entrainment law ([Meakin & Arnett, 2007](#)) and new forms of the diffusive mixing coefficient (e.g. [Pratt et al., 2017](#)). In particular, [Staritsin \(2013, 2014\)](#) has published stellar evolution models that include turbulent entrainment at convective boundaries. We will discuss possible applications of these mixing parameterisations regarding our studies of the red-giant branch bump in Sec. 4.4.

2.2.2 Uncertainties From Poorly-Constrained Chemical Composition Parameters

Solar Abundance Scale

For a given metallicity $[\text{Fe}/\text{H}]$, different choices of solar abundances result in different hydrogen, helium, and metal mass fractions X , Y , and Z via solar model calibration. During this process, one aims at reproducing the observed luminosity, radius, effective temperature and age of the Sun, by calibrating the mixing-length parameter, the initial helium abundance, and the metallicity. Because of this, evolutionary tracks computed with a different solar abundance scale may exhibit similar paths in the Hertzsprung-Russell diagram, but with discrepancies of a few percent in mass ($\sim 2\%$) and age (up to 10%).

See, e.g., [Asplund et al. \(2009, 2021\)](#) for a detailed discussion about the chemical composition of the Sun, and its implications in astronomy.

Helium Content

The initial helium abundance, Y_0 , is either determined by assuming a chemical enrichment law, $\Delta Y/\Delta Z$, from the Galactic chemical evolution, or by adjusting it to

fit the solar calibration. As of now, there is still no consensus on the value of $\Delta Y/\Delta Z$, and literature values can be found within a range as large as 0.8-3.0. Different stellar evolution codes adopt different galactic enrichment ratios. An evolutionary track with a given mass and helium content can be reproduced with a lower helium content, if the mass is slightly increased. This can lead to a different age estimation, older in the latter case, during the main-sequence and red-clump phases.

2.2.3 From Uncertain Physical Processes

Diffusion

If atomic diffusion is at work within a star, present-day surface abundances are not the same as the initial ones. In models including diffusion, the envelope opacity increases due to the enhancement of hydrogen in the envelope. Hence, the envelope is deeper and these tracks are cooler than those which do not take diffusion into account. On the main sequence, the larger central helium abundance (hence, mean molecular weight) results in a luminosity increase, and thus in a shorter main-sequence lifetime. Indeed, previous studies have shown that atomic diffusion reduces the age of low-mass stars at the main-sequence turn off by a few percent, with important consequences for the age-dating of globular clusters (see, e.g., [Jofré & Weiss, 2011](#)).

2.2.4 From Numerical Implementation

There can also be numerical differences between the various stellar evolution codes. As part of the CoRoT/ESTA (Evolution and Seismic Tools Activity) project, [Monteiro et al. \(2006\)](#); [Lebreton et al. \(2008\)](#) have compared the global quantities, physical structure, and oscillation properties produced by five different stellar evolution codes, using the same input physics, and physical and astronomical constants. Using stellar models representative of CoRoT targets, with masses in the range $0.9-5 M_{\odot}$ and following the evolution from the pre-main sequence (or main sequence) to the

subgiant phase, they found very good agreement between the codes, but with noticeable discrepancies in pressure, temperature, luminosity, density, and opacity (at the level of a few percent) resulting from the handling of the equation of state, opacities, and convective boundaries.

Later, this has been addressed again in a series of workshops, entitled *The Aarhus red giants challenge* (Silva Aguirre et al., 2020). For nine stellar evolution codes, using the same set of input physics and physical constants, they computed evolutionary tracks and stellar structure models at a given radius along the red-giant branch for different masses (between 1.0 and 2.5 M_{\odot}), and compared the predicted stellar properties. They found differences of a few tens of K in the predicted effective temperatures, variations of 2-5% (increasing with stellar mass) in predicted ages, a spread of about 10% in the luminosity of the red-giant branch bump, and a spread of ~ 0.1 dex in the [C/N] abundance ratio. They associated these remaining discrepancies between the codes with differences in the energy generation routines and interpolation across opacities. A companion paper has been specifically dedicated to the comparison of pulsation properties, derived with the same oscillation code to investigate how differences in the model calculation affect modelled oscillation frequencies and other asteroseismic diagnostics (Christensen-Dalsgaard et al., 2020).

Chapter 3

Asteroseismology of Solar-Like Oscillators

Until the last few decades, investigations of stellar interiors had been restricted to theoretical studies only constrained by observations of their global properties and surface characteristics (e.g. luminosity and temperature at the photosphere). However, in the last 30 years, the field has been revolutionised by the ability to perform seismic investigations of stellar interiors, starting with the Sun (*helioseismology*) and extending, a few years later, to stars other than the Sun (*asteroseismology*). One can investigate the physical processes involved in the same way that seismologists learn about the Earth's interior by monitoring waves caused by earthquakes.

In this chapter, I focus on solar-like oscillators, variable stars (see Fig. 3.1, displaying the different classes of pulsating stars) defined by the presence of surface convection which can stochastically excite pulsation modes. After a brief overview of asteroseismic observations, I introduce a few key aspects of the theoretical foundation for stellar oscillations. The last part of this chapter is dedicated to global asteroseismic diagnostics, and how they allow us to determine fundamental stellar parameters.

For recent, comprehensive, reviews on the subject, see e.g. [Chaplin & Miglio \(2013\)](#); [Hekker & Christensen-Dalsgaard \(2017\)](#); [García & Ballot \(2019\)](#).

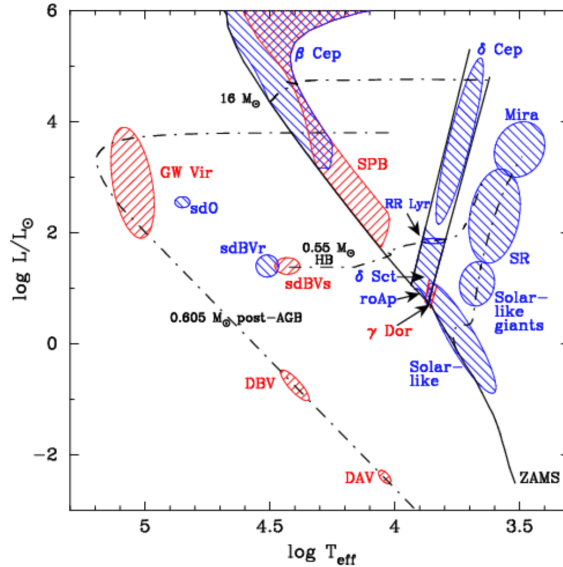


Figure 3.1: Schematic Hertzsprung-Russell diagram showing the location of several classes of pulsating stars. The solid line indicates the zero-age main sequence. The dot-dashed lines show different features: evolutionary tracks, the horizontal branch, and the white-dwarf cooling curve. The current study focuses on solar-like oscillations. Figure taken from [Mosser \(2015\)](#); [Aerts et al. \(2010\)](#).

3.1 Observations

Asteroseismology uses photometric or spectroscopic observations to extract the frequencies, amplitudes and phases of global resonant modes observed at a star’s surface. Because the frequencies of stellar oscillations are determined by the properties of the resonant cavities, they offer a unique opportunity to probe stellar interiors.

Before space-borne observations became possible, the best examples of asteroseismology used to rely on ground-based datasets. Compared to the current standards with the space-borne missions and month-long, or even year-long, continuous time series, these pulsation spectra were derived from short, non-continuous and/or noisy time series in the case of solar-like pulsators (see, e.g., [Bedding, 2014](#), for a review on observations of solar-like oscillations).

In this context, the space missions CoRoT, in 2006 ([Baglin et al., 2009](#)), and *Kepler*, in 2009 ([Borucki et al., 2010](#)), were the major breakthroughs resulting in exquisite quality photometric data on solar-like oscillations, for a huge amount of

solar-type (~ 600) and red-giant stars ($\sim 30,000$). These two missions have provided a wealth of high-quality and long-duration observational data that allow us to measure and characterise stellar oscillations. Furthermore, the re-purposed *Kepler* mission, *K2*, has performed a survey of stars in the ecliptic plane from 2014 to 2018 (Howell et al., 2014). Finally, the ongoing TESS mission (2018) is adding to the harvest of bright Sun-like stars in the solar neighbourhood (Ricker et al., 2015); while PLATO’s launch is planned for 2026, aiming to cover a significantly larger fraction of the sky¹. Thanks to the current missions and the future ones, data for many thousands of stars in many different regions of the Galaxy are becoming available.

3.2 Theory of Stellar Oscillations

3.2.1 Adiabatic Approximation

In order to establish the oscillation equations laying the foundation for asteroseismology, several well-known equations of hydrodynamics come into play: the equation of continuity, the equation of motion, the Poisson equation, the energy equation, the radiative flux equation (treated in the diffusion approximation), the convective flux equation, and the equation of state. Besides, in the case of solar-like oscillations, considerable simplifications in this set of equations are possible. Indeed, the observed solar-like oscillations, defined in the next section, have very small relative amplitudes so they can be treated as small perturbations around a static equilibrium state. The equilibrium structure is spherically symmetric and there is no mean motion because effects of rotation and magnetic fields are ignored.

Moreover, for the purpose of calculating stellar oscillation frequencies, the complications related to the energy equation can be avoided by neglecting the heating term. The latter is generally very small compared with the time-derivative terms. Indeed, a comparison of the physical timescales within the star demonstrates the adiabatic behaviour of the perturbation, i.e. there is no energy exchanged between

¹<https://sci.esa.int/web/plato/-/59252-plato-definition-study-report-red-book>

the wave and fluid. This is justified by the fact that the temporal evolution of the wave is much more rapid than the characteristic time of any mechanism transferring energy as heat between the different fluid elements. In these conditions, the motion occurs adiabatically and this constitutes the foundation for the most frequently used equations in seismology.

Nonetheless, it is still necessary to consider under what circumstances this adiabatic approximation is valid. At great depth, the energy content is so large that the flow of energy over a pulsation period has no effect on the energy content; there is no time for the oscillation to gain or lose energy. This corresponds to the adiabatic case, which applies for most of the star. Very near the surface, however, the density is low and the full energy equation must be taken into account; the oscillation has time to gain or lose energy. This corresponds to the strongly non-adiabatic limit. Non-adiabatic processes need to be considered to understand driving and damping processes, which happen in the superficial layers of stars, as we will see below.

3.2.2 Solar-Like Oscillations

Solar-like pulsators are a class of variable stars defined by the presence of surface convection, which can excite pulsation modes (Fig. 3.1). Their oscillations are intrinsically damped and excited stochastically by the near-surface convection. In these stars, the convective motion near the surface, i.e. in non-adiabatic layers, likely reaches speeds close to that of sound. As a result of this turbulent motion with near-sonic speed, modes are stochastically excited, i.e. turbulent eddies drive ‘randomly’ the normal modes, to the observed amplitude in the uppermost layers of stars where turbulence is important.

The oscillation spectra shown by F-G main-sequence and subgiant stars, as well as F-G-K red-giant stars, are very rich (more than a million of detected modes in the Sun), due to stochastic excitation and the relative ease of mode identification, with multiple overtones excited to observable amplitudes. For illustrative purposes,

the solar oscillation spectrum is shown in Fig. 3.2. One of the quantities describing pulsation modes is the radial order, i.e. the number of nodes between a star’s centre and its surface. Main-sequence and subgiant stars display high-order acoustic modes with periods of a few minutes; whereas, red giants display low to mid-order acoustic modes with periods from a few minutes to a few hours.

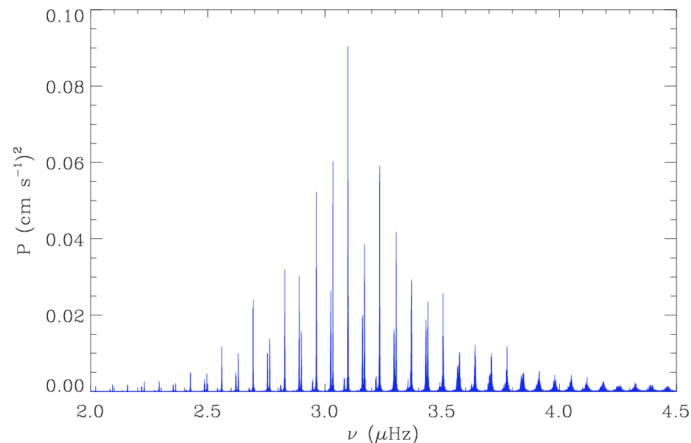


Figure 3.2: Solar oscillation spectrum with data from SOHO/GOLF ([Gabriel et al., 1995](#)). Figure taken from [Mosser \(2015\)](#).

Pressure and Gravity Modes

There are two main sets of solutions to the equation of motion for a pulsating star and these lead to stellar oscillations having their physical origins in two types of standing waves:

- *pressure modes* (p modes), where pressure gradient is the primary restoring force for a star perturbed from equilibrium. These are acoustic waves and have gas motions that are primarily vertical;
- *gravity modes* (g modes), where gravity is the restoring force and the gas motions are primarily horizontal (see Sec. 3.3.2 and Chap. 7 in [Christensen-Dalsgaard’s lecture notes on stellar oscillations](#)). Necessarily, gravity waves cannot propagate in convective regions (Schwarzschild criterion). As g modes have an evanescent behaviour in the convective region, their detection is quite challenging in cool stars ([Belkacem et al., 2009](#)).

Mixed Modes

The distinction made above, between acoustic modes and gravity modes, assumes that the modes are completely trapped in their propagation region. However, when solar-like stars reach the end of the main sequence, this separation is less pronounced, and g modes in the core and p modes in the envelope may coexist. When the evanescent region between the two trapping regions is small enough, a coupling between the p- and g-mode cavities occurs. This leads to *mixed modes*, combining the characteristics of both pressure and gravity modes.

The properties of mixed modes were initially discussed theoretically by [Scuflaire \(1974\)](#). [Kjeldsen et al. \(1995\)](#) reported the first observations of mixed modes in a solar-like oscillator, η Bootis, which were then confirmed later by [Kjeldsen et al. \(2003\)](#). Additional observations of mixed modes followed thanks to the CoRoT and *Kepler* missions (e.g. [Deheuvels et al., 2010](#); [Chaplin et al., 2010](#)). In particular, [Beck et al. \(2011\)](#) first reported the existence of mixed modes in red-giant stars. Shortly after, [Bedding et al. \(2011\)](#) and [Mosser et al. \(2011b\)](#) highlighted the potential of these modes to distinguish between first-ascent red giants burning hydrogen in a shell and red clump stars igniting helium in their core, as suggested by theory in [Montalbán et al. \(2010\)](#).

3.3 Asteroseismic Diagnostics

Asteroseismic techniques for estimating fundamental stellar properties have undergone an important development, providing the means to estimate precise and accurate properties of large numbers of field stars, which before had to rely on spectroscopic or photometric observations of basic surface properties only. Specifically, individual frequencies provide discrimination between stars with different fundamental properties that share similar surface properties ([Bedding et al., 2011](#)). Also, the comparison between the measured oscillation frequencies and those predicted by models improves the input physics of models to a precision that cannot be reached

by any other method (Lebreton & Goupil, 2014).

3.3.1 Global Asteroseismic Observables

The automated analysis codes developed for application to CoRoT and *Kepler* data have enabled efficient extraction of the global characteristics of the oscillation spectra, such that the frequency of the maximum power amplitude (ν_{\max}) or the regularities in frequency ($\langle\Delta\nu\rangle$), shown in Fig. 3.3, on large numbers of stars, which we will introduce in the following sections.

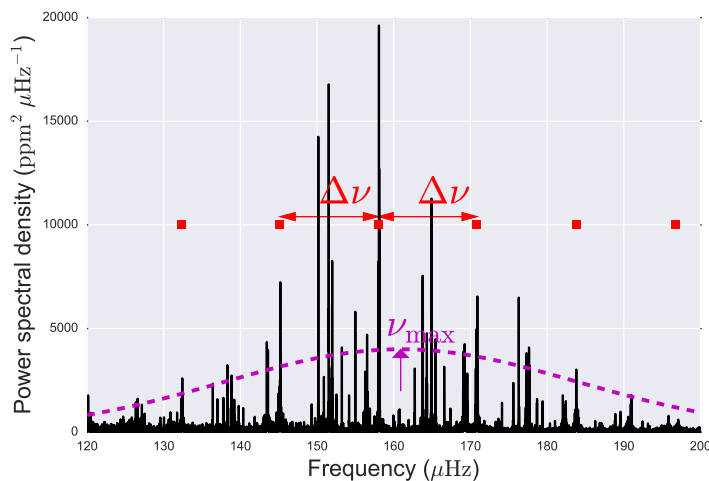


Figure 3.3: Power spectrum for KIC 12008916, where the amplitude is normalised to parts per million (ppm). Red symbols represent the radial modes ($\ell = 0$). Examples of the large separation $\langle\Delta\nu\rangle = \nu_{n+1,\ell=0} - \nu_{n,\ell=0}$ between radial modes are shown. The oscillation envelope of power is illustrated and its maximum is labelled as ν_{\max} . Figure taken from Davies & Miglio (2016).

Frequency of maximum oscillation power (ν_{\max})

The continuous increase of detected stars with solar-like oscillations, and especially observations of solar-like oscillations in members of eclipsing binaries and clusters, have strengthened the empirical relation between the frequency of the maximum in the power spectrum (ν_{\max}) of solar-like oscillations and the acoustic cut-off frequency (ν_c) (Brown et al., 1991; Kjeldsen & Bedding, 1995). Oscillation modes are typically trapped in the stellar interior when their frequency is below that of the cut-off frequency, and become travelling waves when it increases above this critical

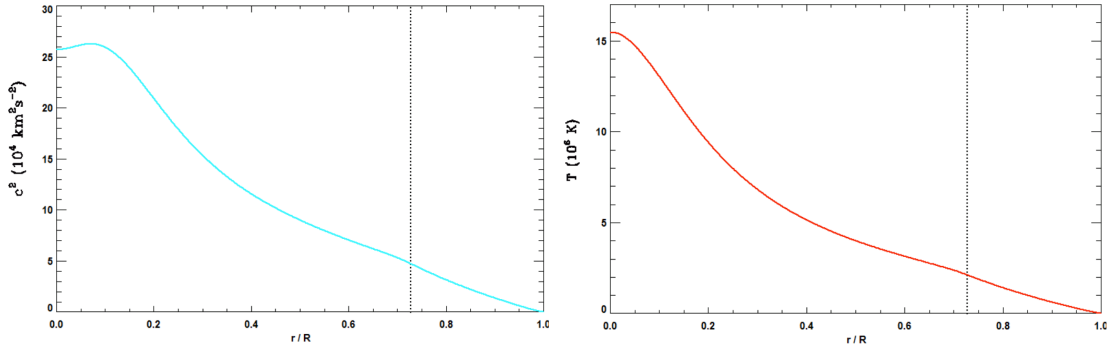


Figure 3.4: Solar squared sound-speed (left) and temperature (right) profiles. The dotted vertical line shows the transition between the radiative interior and the adiabatic envelope. Figures taken from [Mosser \(2015\)](#).

value. However, the underlying physical origin of this scaling relation was poorly understood for a long time.

[Belkacem et al. \(2011\)](#) tried to provide a theoretical basis for the $\nu_{\max} - \nu_c$ scaling relation, examining how ν_{\max} and ν_c depend on the characteristic thermal timescale in the upper convective layers. The depression of the damping rates (see Fig. 1 in [Belkacem, 2012](#)) originates from a destabilising effect in the superadiabatic layers, a resonance between the local thermal timescale in the superadiabatic region and the modal period. They first confirmed that this depression is responsible for the presence of a maximum in the power spectrum. Indeed, the latter results from a balance between the damping and the driving of the modes, depending on the dynamical properties of the convective region. As for the cut-off frequency, it is associated with the mean surface layers properties of the star and the sound speed.

The sound-speed profile (Fig. 3.4, left panel) is defined by

$$c_s^2 \stackrel{\text{def}}{=} \left(\frac{\partial p}{\partial \rho} \right)_S \stackrel{\text{def}}{=} \Gamma_1 \frac{p_0}{\rho_0}, \quad (3.1)$$

where Γ_1 is the adiabatic index. In an isothermal atmosphere, at a temperature T_0 , where the classical non-degenerate perfect gas law is relevant, Eq. (3.1) reduces to

$$c_{\text{PG}}^2 = \frac{\Gamma_1 k_B T_0}{\mu},$$

where k_B is the Boltzmann constant, and μ is the mean particle mass, so that the sound-speed and temperature profiles are closely linked (see Fig. 3.4).

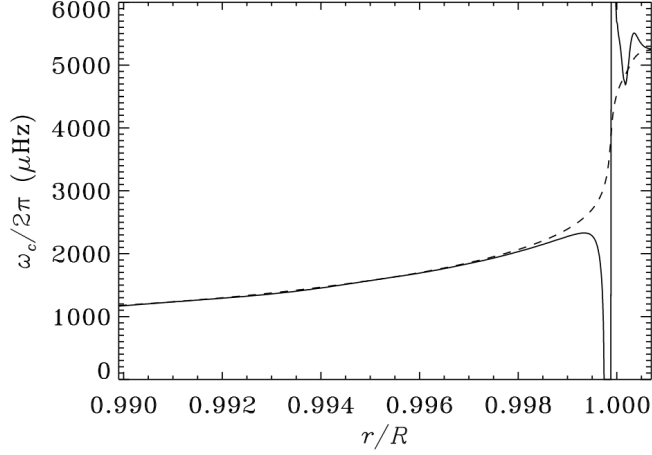


Figure 3.5: Acoustic cut-off frequency (solid line) as a function of the normalised radius, in the outermost parts of a model of the present Sun. Figure taken from [Christensen-Dalsgaard's lecture notes on stellar oscillations](#).

Then, it is possible to infer a theoretical relation for the cut-off frequency:

$$\omega_c = 2\pi\nu_c = \frac{c_s}{2H_\rho} \propto \frac{g}{\sqrt{T_{\text{eff}}}} \propto \frac{M}{R^2\sqrt{T_{\text{eff}}}}, \quad (3.2)$$

where c_s is the sound speed, H_ρ is the density scale height, g is the gravitational field, M is the mass, R is the radius, and T_{eff} is the effective temperature. The acoustic cut-off frequency is the highest frequency for acoustic modes and defines the upper boundary of the p-mode resonant cavities. This frequency is small everywhere except near the surface where it shows large values and a steep profile (Fig. 3.5), ensuring that all waves are approximately reflected at the same location. Since the density variation with altitude is much more important than the sound-speed variation, especially near the surface of the star, the highest value of ω_c is reached at the level where the density scale height is minimum, close to the level where the temperature is minimum. Thereafter, when scaled to the solar case, Eq. (3.2) becomes

$$\nu_c = \left(\frac{M}{M_\odot}\right) \left(\frac{R}{R_\odot}\right)^{-2} \left(\frac{T_{\text{eff}}}{T_{\text{eff},\odot}}\right)^{-1/2} \nu_{c,\odot}, \quad (3.3)$$

with $\nu_{c,\odot} \simeq 5.3$ mHz, and M_\odot , R_\odot , $T_{\text{eff},\odot}$ are the solar values of mass, radius and effective temperature, respectively.

Belkacem et al. (2011) then derived an observed scaling relation between ν_{max} and ν_c :

$$\nu_{\text{max}} \propto \frac{1}{\tau} \propto \left(\frac{\Gamma_1^2}{\chi_\rho \Sigma} \right) \left(\frac{\mathcal{M}_a^3}{\alpha_{\text{MLT}}} \right) \nu_c, \quad (3.4)$$

where $\Gamma_1 = (\partial \ln P / \partial \ln \rho)_{\text{ad}}$, $\chi_\rho = (\partial \ln P / \partial \ln \rho)_T$, $\Sigma = (\partial \ln \rho / \partial \ln T)_{\mu,P}$, μ is the mean molecular weight, $\mathcal{M}_a = v_{\text{conv}}/c_s$ is the Mach number in the uppermost convective region where modes are excited, and α_{MLT} is the mixing-length parameter. The Mach number having a weak dependence on stellar evolution ($\sim g^{-0.012}$; Belkacem et al., 2013), Eq. (3.4) mostly reduces to $\nu_{\text{max}} \propto \nu_c$.

Large frequency spacing ($\langle \Delta \nu \rangle$)

In order to define the large separation ($\langle \Delta \nu \rangle$), it is necessary to introduce the asymptotic relation (Tassoul, 1980), followed by low-degree pressure modes ($\ell \ll n$), that permits us to express modal frequencies ($\nu_{n,\ell}$) as a function of the structure of the star, i.e.

$$\nu_{n,\ell} = \left(n + \frac{\ell}{2} + \varepsilon \right) \Delta \nu + \text{2nd order}, \quad (3.5)$$

where n is the radial order, ℓ is the angular degree, and ε is a constant of order unity. Such an asymptotic analysis assumes that we consider high radial-order modes. Hence, from Eq. (3.5), the large separation, which is defined as the frequency separation between two consecutive radial orders (for a given ℓ), is given by

$$\Delta \nu \equiv \nu_{n+1,\ell} - \nu_{n,\ell} \simeq \left[2 \int_0^R \frac{dr}{c_s} \right]^{-1},$$

and therefore represents the inverse of the sound travel time for a sound wave from the surface of the star to the core and back again, providing an estimate of the

inverse of the acoustic stellar diameter. Still, this requires the condition $n \gg \ell$ to be strictly fulfilled, so that the second-order term of the asymptotic expansion becomes negligible. In fact, such a condition is hardly met since pressure modes are not observed at high frequency, as a result of their stochastic excitation in the upper convective envelope. The highest peaks in the solar oscillation spectrum (Fig. 3.2) have a radial order close to 21, which is not high enough for a strict application of the asymptotic expansion. In more evolved stars, the situation is even worse: 18-22 for main-sequence stars, 15-18 for subgiants, below 15 for red giants, and typically 8 for a red-clump star (Mosser, 2015). So, it is clear that observations do not match the asymptotic conditions and cannot directly provide asymptotic parameters.

Subsequently, adopting the homology relations, the large separation of a given star can also be related to its mean density (Belkacem et al., 2013), such as

$$\Delta\nu = \left(\frac{\bar{\rho}}{\bar{\rho}_{\odot}}\right)^{1/2} \Delta\nu_{\odot} = \left(\frac{M}{M_{\odot}}\right)^{1/2} \left(\frac{R}{R_{\odot}}\right)^{-3/2} \Delta\nu_{\odot}, \quad (3.6)$$

where, as classically found in the literature, the Sun has been used as the reference. Eq. (3.6) demonstrates the scaling relation between $\Delta\nu$ and $\bar{\rho}$ and shows that the only underlying hypothesis is the homology. Nevertheless, as stated in Belkacem et al. (2012), a star breaks all the requirements during its evolution (hydrostatic equilibrium, thermal equilibrium, constitutive equations must be power laws of their arguments), implying a departure from the homology. Thus, this scaling relation needs to be investigated further in order to find out the physical reason explaining precisely the origin of this departure.

Furthermore, since all modes are not necessarily equally spaced, it is recommended to estimate the average large frequency spacing, defined as

$$\langle \Delta\nu_{\ell} \rangle = \frac{\sum_{i=n_1}^{n_2} \nu_{i+1,\ell} - \nu_{i,\ell}}{n_2 - n_1 + 1} = \frac{\nu_{n_2+1} - \nu_{n_1}}{n_2 - n_1 + 1}, \quad (3.7)$$

where the interval $[n_1, n_2]$ spans the visible oscillation modes around n_{\max} , i.e. the radial order at which the frequency of maximum oscillation power occurs. In order to avoid any complication due to mixed modes, we focus our interest on radial modes, in such a way that $\langle \Delta\nu \rangle = \langle \Delta\nu_{\ell=0} \rangle$,

3.3.2 Asteroseismic Methods: Scaling Relations and Grid-Based Modelling

Given the ν_{\max} and $\langle \Delta\nu \rangle$ scaling relations, it is now possible to link seismic global quantities to stellar parameters. If estimates of ν_{\max} and $\langle \Delta\nu \rangle$, along with an independent estimate of T_{eff} , are available, it is then possible to have a ‘direct’ estimation of the stellar mass and radius. Using Eqs. (5.2) and (3.6), we obtain the desired relations (normalised to the solar values):

$$\left(\frac{R}{R_{\odot}} \right) \simeq \left(\frac{\nu_{\max}}{\nu_{\max,\odot}} \right) \left(\frac{\langle \Delta\nu_{nl} \rangle}{\langle \Delta\nu_{nl} \rangle_{\odot}} \right)^{-2} \left(\frac{T_{\text{eff}}}{T_{\text{eff},\odot}} \right)^{1/2} \quad (3.8)$$

$$\left(\frac{M}{M_{\odot}} \right) \simeq \left(\frac{\nu_{\max}}{\nu_{\max,\odot}} \right)^3 \left(\frac{\langle \Delta\nu_{nl} \rangle}{\langle \Delta\nu_{nl} \rangle_{\odot}} \right)^{-4} \left(\frac{T_{\text{eff}}}{T_{\text{eff},\odot}} \right)^{3/2}. \quad (3.9)$$

Even though they are not uniformly fixed in the literature, the solar values are close to $\nu_{\max,\odot} \simeq 3090 \mu\text{Hz}$, $\Delta\nu_{\odot} \simeq 135 \mu\text{Hz}$ and $T_{\text{eff},\odot} \simeq 5777 \text{ K}$. These equations constitute the main frame of what is commonly called *ensemble* asteroseismology, providing us with the tools for a new grip on stellar physics. They are used for diverse applications: model-independent determination of stellar parameters (known as the *direct method*; e.g., [Mosser et al., 2010](#)), constraints on stellar evolution and populations (see, e.g., [Miglio 2012](#) for constraining mass loss at the tip of the red-giant branch; [Miglio et al. 2012b](#) for constraining populations in the Milky Way), distance indicator (e.g., [Miglio et al., 2012a](#); [Silva Aguirre et al., 2012](#)), improved determination of $\log g$ (e.g., [Morel & Miglio, 2012](#)) and T_{eff} (e.g., [Batalha et al.,](#)

2011), among others.

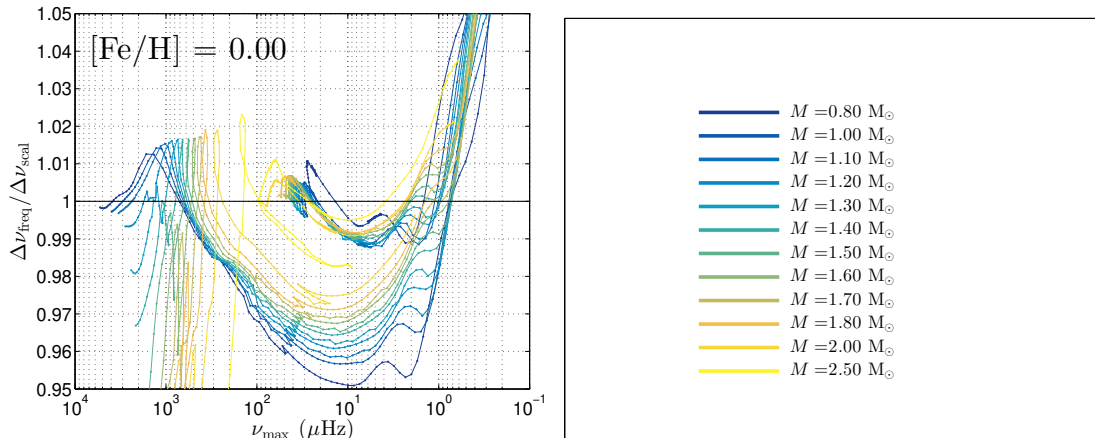


Figure 3.6: Correction to be applied to the $\langle \Delta\nu \rangle$ scaling relation as a function of ν_{\max} , for a solar metallicity ($[\text{Fe}/\text{H}] = 0.0$). The coloured lines correspond to evolutionary tracks with different masses, from 0.80 to $2.50 M_{\odot}$. Figure taken from [Rodrigues et al. \(2017\)](#).

Another approach is to include models of stellar evolution when estimating the masses and radii. This so-called *grid-based method* uses evolutionary tracks computed for a range of masses and metallicities, and searches for a best-fitting model, with ν_{\max} , $\langle \Delta\nu \rangle$, T_{eff} , $[\text{Fe}/\text{H}]$, individual mode frequencies or frequencies combinations as possible input parameters (e.g., [Basu et al., 2010](#); [Rodrigues et al., 2017](#)). It consists in searching for an agreement between observations and model grids, looking for the stellar mass and radius in the grid corresponding to the observed oscillation spectrum.

A significant advantage of this method has to do with the definition of the large frequency spacing $\langle \Delta\nu \rangle$. To a first approximation, $\langle \Delta\nu \rangle$ can be estimated in the models using Eq. (3.6). However, this estimate can be inaccurate because of systematic effects that depend, e.g., on the evolutionary phase and, more generally, on how the sound speed behaves in the stellar interior. A way to go beyond the $\langle \Delta\nu \rangle$ scaling relation is to compute an average large frequency spacing based on individual radial-mode frequencies. This has been done in [Rodrigues et al. \(2017\)](#), where they adopted a $\langle \Delta\nu \rangle$ definition as close as possible to the observational one.

To illustrate this, Fig. 3.6 shows how the $\langle\Delta\nu\rangle$ scaling relation deviates from the one calculated from individual frequencies, in the solar-metallicity case.

More generally, one can use fitting of individual-mode frequencies as a way to go beyond both ν_{\max} and $\langle\Delta\nu\rangle$ scaling relations, as presented in [Rendle et al. \(2019a\)](#) and applied in [Montalbán et al. \(2021\)](#).

Finally, independent measurements of masses and radii have been shown to be within a few percent of those obtained from asteroseismology, based on observations of eclipsing binaries ([Gaulme et al., 2016](#); [Brogaard et al., 2016, 2018](#)), stellar clusters ([Miglio et al., 2016](#); [Stello et al., 2016](#); [Handberg et al., 2017](#)), and stars with precise distances ([Zinn et al., 2019](#); [Khan et al., 2019](#); [Hall et al., 2019](#)). This underlines the strong potential of asteroseismology for the estimation of precise and accurate stellar fundamental parameters.

Chapter 4

The Red-Giant Branch Bump

The entirety of the text in Sec. 4.2 is taken verbatim from the published paper [Khan et al. \(2018\)](#), of which I was first author. In terms of individual work performed, I completed the majority of the work. Oliver J. Hall developed the statistical mixture models used to determine the position of the red-giant branch bump. Andrea Miglio performed the grid-modelling analysis using the `PARAM` code.

The chapter is organised as follows: Sec. 4.1 introduces the red-giant branch bump and its observational properties, as well as former studies primarily based on globular clusters; Sec. 4.2 presents our novel analysis of the bump combining *Kepler* and APOGEE data; Sec. 4.3 features an ongoing analysis of Galactic and Magellanic Clouds clusters stemming from the findings of the preceding section; and, finally, Sec. 4.4 mentions ways of combining all the observational evidence gathered with results from hydrodynamical simulations to go beyond the standard convective overshooting prescriptions.

4.1 The Red-Giant Branch Bump

Observationally, the red-giant branch bump (RGBb) was detected for the first time in the Galactic globular cluster (GC) 47 Tuc by [King et al. \(1985\)](#). The colour-magnitude diagram of 47 Tuc is shown on Fig. 4.1, where the accumulation of stars,

resulting in a local maximum in the luminosity function, is clearly visible.

Before its first empirical confirmation, the bump was already expected through models of low-mass stars showing a temporary luminosity decrease during the evolution on the red-giant branch, with pioneering investigations by [Thomas \(1967\)](#) and [Iben \(1968\)](#). Taking the example of a stellar model with a mass $M = 1.40 M_{\odot}$ and a metallicity $[M/H] = 0.0$ dex, this behaviour is shown by the inset zooming on the red-giant branch bump in the Hertzsprung-Russell Diagram: the luminosity increases, decreases and increases again (Fig. 4.2).

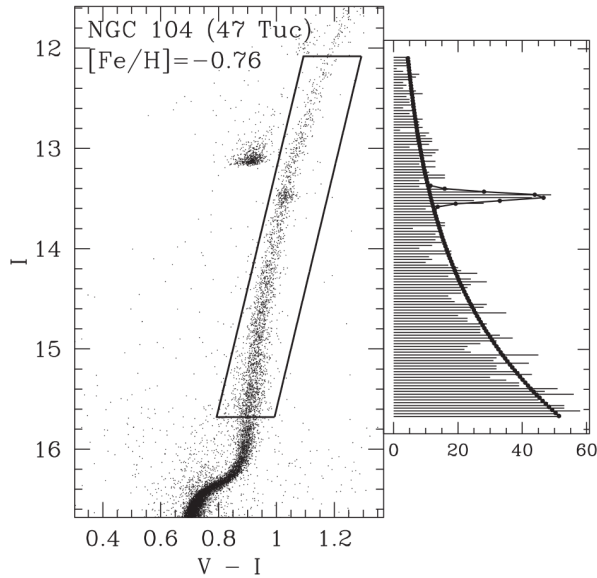


Figure 4.1: Colour-magnitude diagram (left) and luminosity function, i.e. number of stars per luminosity / magnitude interval (right) of 47 Tuc. Figure taken from [Nataf et al. \(2013\)](#).

4.1.1 Detailed Reason Behind the Occurrence of the Red-Giant Branch Bump

The detailed reason behind the bump is still an open issue that has been subject of some discussion. At the time, there is no definitive answer to this question but a few different interpretations are summarised below.

The occurrence has been associated with the direct effect of the increase in

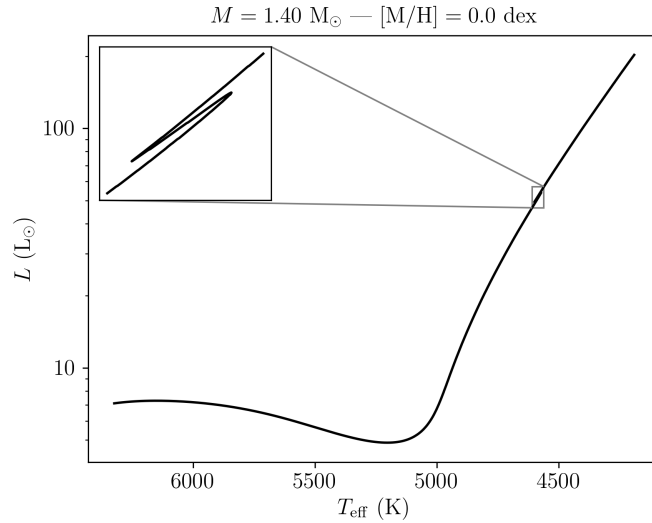


Figure 4.2: Hertzsprung-Russell diagram for a model of a star with a mass $M = 1.40 M_{\odot}$ and a metallicity $[M/H] = 0.0$ dex. The inset is zooming on the location of the red-giant branch bump.

the hydrogen abundance in the hydrogen-burning shell as the latter crosses the composition discontinuity. In this scenario, the star reacts to the sudden increase in available fuel by lowering its surface luminosity and slowing down the evolutionary timescale. After the shell has moved past the discontinuity, the thermal equilibrium is restored and the surface luminosity starts to increase again (see, e.g., [King et al., 1985](#); [Salaris et al., 2002](#); [Riello et al., 2003](#)). This follows the $L \propto \mu^7$ relation (see [Kippenhahn & Weigert, 1990](#), for details on how to derive this).

However, by looking at the evolution in the vicinity of the bump, [Sweigart et al. \(1990\)](#) noted that the luminosity starts dropping before the hydrogen-burning shell actually reaches the chemical discontinuity. Because the shell is as thin as $\sim 0.001 M_{\odot}$ at this point, they rejected the possibility that the hydrogen-burning shell would sense the increase in the fuel available to the nuclear reactions that it has not yet reached. Instead, they pointed to the increase in the opacity just above the shell that results from the larger hydrogen abundance in the envelope.

[Refsdal & Weigert \(1970](#), see also [Kippenhahn & Weigert 1990](#)) carried out a

homology analysis of the properties of the region inside and above the burning shell. They noted a steep increase in the luminosity with the mean molecular weight μ , and pointed out that the increase in the hydrogen abundance outside the composition gradient caused a decrease in μ , and hence in luminosity.

Following [Refsdal & Weigert \(1970\)](#)'s shell homology analysis, [Christensen-Dalsgaard \(2015\)](#) opted for the interpretation that underlines the importance of the variation in mean molecular weight as the main condition leading to the bump. He relates the luminosity excursion in the bump to the effect of the dredge-up composition gradient on the hydrostatic structure of the region immediately above the hydrogen-burning shell — the effective weight of the overlying material being reduced by the decrease in the mean molecular weight above the discontinuity.

More recently, [Hekker et al. \(2020\)](#) explored changes in the specific entropy to investigate the underlying physical reasons for both the mirror principle and the red-giant branch bump. While the mirror principle is in place during most of the evolution along the red-giant branch, they found that at the luminosity maximum of the bump the mirror principle is not in effect anymore and the star is fully contracting. The star then regains its mirror when the hydrogen-burning shell reaches the chemical discontinuity, coinciding with the luminosity minimum of the bump, in line with what [Christensen-Dalsgaard \(2015\)](#) found.

4.1.2 Characteristic Properties

The importance of the red-giant branch bump for testing stellar evolution has long been recognised. Due to their sensitivity to the internal properties of stars, the RGBb luminosity, number counts, and shape (i.e. width in the luminosity distribution) provide robust constraints on the chemical profile inside red-giant structures and demark the maximum downward penetration of the convective envelope during

the first dredge-up. As such, they are excellent probes of the interior structure and mixing of stars.

Luminosity

The red-giant branch bump brightness depends on the maximum depth attained by the convective envelope and on the chemical profile above the advancing hydrogen-burning shell. The deeper the chemical discontinuity is located inside the stellar structure, the fainter the bump luminosity will be. The comparison of the theoretical bump luminosity with observations provides valuable information about the internal structure of low-mass stars at the beginning of their red-giant branch evolution.

In the framework of globular clusters, the bump luminosity is affected by both theoretical (treatment of the convective transport in stellar envelopes) and observational (cluster distances and reddening) uncertainties. As a way to mitigate this effect, [Fusi Pecci et al. \(1990\)](#) suggested using the $\Delta V_{\text{HB}}^{\text{RGBb}} = V_{\text{RGBb}} - V_{\text{HB}}$ parameter, i.e. the difference in apparent visual magnitude between the RGBb and the horizontal branch at the RR Lyrae instability strip. They showed that the $\Delta V_{\text{HB}}^{\text{RGBb}}$ values predicted by theory were 0.4 mag brighter than the empirical estimates in a sample of 11 GCs. [Alongi et al. \(1991\)](#) interpreted this disagreement as evidence of the standard models' limitations in describing the correct location of the red-giant branch bump. In order to reconcile observations and theory, they claimed the occurrence of an additional mixing process at the base of the convective envelope of red-giant stars, i.e. envelope overshooting (see Sec. 2.2.1). Meanwhile, [Straniero et al. \(1992\)](#) called attention to the role of the global metallicity, in the sense that the proper inclusion of the α -enhancement in the computation of the global metallicity could reduce the discrepancy. The latter hypothesis was then confirmed by [Cassisi & Salaris \(1997\)](#), [Zoccali et al. \(1999\)](#), and [Ferraro et al. \(1999\)](#), who argued that there was no significant discrepancy between observations and canonical

stellar models if one accounted for updated input physics and observational uncertainties in $[\text{Fe}/\text{H}]$ and $[\alpha/\text{Fe}]$ abundances. Soon after, [Bergbusch & Vandenberg \(2001\)](#) discussed the failure of their isochrone population function software to generate models matching the observed luminosities of the RGBb in clusters, recording a discrepancy of ~ 0.25 mag. [Riello et al. \(2003\)](#) found a qualitative agreement between theory and observations in a sample of 54 clusters, but claimed that more robust conclusions required more accurate spectroscopic measurements of $[\text{Fe}/\text{H}]$ and $[\alpha/\text{Fe}]$. [Bjork & Chaboyer \(2006\)](#) concluded that their models were consistent with observational results for 19 GCs drawn from [Zoccali et al. \(1999\)](#), with differences within the theoretical uncertainties in stellar evolution as well as within the observational uncertainties in the GC distance modulus and the metallicity scale. The same year, [Meissner & Weiss \(2006\)](#) attempted to simultaneously fit several age indicators of globular cluster CMDs, and the most severe inconsistency with their theoretical models lied in the predicted bump brightness which was too large by up to 0.3 mag.

Despite the wealth of theoretical and observational investigations, finding a common ground as to a discrepancy between standard stellar models' predictions and observations of the RGBb brightness in GCs seemed out of reach. However, there have been new developments since then. Recent studies seem to converge on the significance of this discrepancy and identify overshooting from the bottom of the convective envelope, as suggested by [Alongi et al. \(1991\)](#), as a plausible solution to reproduce the observational constraints. The evidence for a discrepancy between theory and observations of the RGBb started with [Di Cecco et al. \(2010\)](#), who found that the observed $\Delta V_{\text{HB}}^{\text{RGBb}}$ parameters were larger than predicted. Their observational sample included 62 GCs, of which 40% showed discrepancies of 2σ (≈ 0.4 mag) or more, especially in the metal-poor regime ($[\text{M}/\text{H}] \leq -1.6$ dex). A year later, [Cassisi et al. \(2011\)](#) conducted one of the few studies based on $\Delta V_{\text{RGBb}}^{\text{MSTO}} = V_{\text{MSTO}} - V_{\text{RGBb}}$,

i.e. the magnitude difference between the main sequence turn-off and the bump. Their analysis of 12 clusters disclosed a clear discrepancy between theory and observations, since the predicted bump magnitudes were too bright by ~ 0.2 mag on average. Troisi et al. (2011) employed a new parameter $\Delta V_{\text{RGBb}}^{\text{MS}} = V_{\text{MS}} - V_{\text{RGBb}}$, i.e. the difference in magnitude between a given point along the main sequence at the same colour as the bump and the bump itself. Their comparison indicated that the observed $\Delta V_{\text{RGBb}}^{\text{MS}}$ were about 0.4 mag smaller than predicted in the metal-poor regime, supporting previous results about the overestimation of the RGBb luminosity by current evolutionary models. The combination of these three tests with their distinct systematics demonstrates that the discrepancy is not due to factors such as mass loss on the RGBb, incorrectly assumed ages, initial helium abundances, distances, or reddening estimates. Using the most recent empirical RGBb magnitudes from Nataf et al. (2013), Joyce & Chaboyer (2015) found their predicted magnitudes to be too bright in the region $[\text{Fe}/\text{H}] < 1.2$ dex, with a larger discrepancy emerging at the lowest metallicities. Fu et al. (2018)'s models, which included the effect of $[\alpha/\text{Fe}]$, also predicted $\Delta V_{\text{RGBb}}^{\text{MSTO}}$ about ~ 0.1 mag greater than the data points obtained by Nataf et al. (2013).

Star Counts

The brightness of the luminosity function bump is a diagnostic of the maximum extension of the convective envelope reached at the base of the red-giant branch, but it does not provide information on the size of the jump in the mean molecular weight profile left over when the envelope starts to recede. An alternative to comparing luminosity measurements and predictions is to do the same for the normalisation of the RGBb, i.e. the star counts. Since the evolutionary rate dL/dt along the red-giant branch is strongly affected by any change in the chemical composition profile, it is clear that this information can be obtained by analysing star counts in the bump region. Whereas the luminosity of the RGBb accounts for the location

of the abundance discontinuity within the star, the normalisation of the RGBb will be proportional to the amplitude of that discontinuity, as the decreased molecular weight will slow down the efficiency of nuclear burning.

This is a further test for the accuracy and adequacy of canonical red-giant branch models that was first performed by [Bono et al. \(2001\)](#), who introduced a new observable R_{RGBb} measuring the relative enhancement of the number of stars in the RGBb, i.e. the ratio between the number of stars across the bump, $V_{\text{RGBb}} - 0.4 \leq V \leq V_{\text{RGBb}} + 0.4$ mag, and the number of fainter RGB stars, $V_{\text{RGBb}} + 0.5 \leq V \leq V_{\text{RGBb}} + 1.5$. The R_{RGBb} parameter does not depend on the absolute position of the bump and, in turn, on the cluster metallicity. In fact, if the bump becomes fainter, the star counts across the bump increase, but the number of stars in the normalisation region increases as well; thus, a shift in the bump luminosity does not affect R_{RGBb} . As a consequence, the R_{RGBb} parameter can supply tight constraints on the timescale of shell-hydrogen burning during the crossing of the chemical discontinuity left over by the first dredge-up. Parameters that affect R_{RGBb} the most are $[\alpha/\text{Fe}]$, the mixing length, the high-temperature opacities, the helium diffusion, and the low-temperature opacities (see, e.g., [Bjork & Chaboyer, 2006](#)).

[Bono et al. \(2001\)](#) showed that canonical evolutionary models were in fair agreement with observed values, suggesting that red-giant branch models properly accounted for the size of the chemical discontinuity. [Riello et al. \(2003\)](#)'s analysis suggested a very good quantitative agreement between theory and observations of the R_{RGBb} parameter, regardless of the adopted metallicity scale — also because of the weak dependence of this parameter on the cluster metallicity, which minimises the effects related to the uncertainties on the $[\text{M}/\text{H}]$ scale. [Bjork & Chaboyer \(2006\)](#) found R_{RGBb} to be a robust prediction of standard stellar evolution that is in rea-

sonable agreement with observations.

Since then, vast improvements were made in the GC metallicity scale, in both the quality and the quantity of the available photometric data, as well as in the methodology employed to measure the RGBb (Nataf et al., 2013). Unlike the previous works, Nataf et al. (2013) did not use the R_{RGBb} parameterisation: primarily, due to its lower signal-to-noise ratio; secondly, due to its sensitivity to photometric incompleteness. Both drawbacks can be traced to its arbitrary integration limits. To mitigate these issues, they introduced a new normalisation parameter: EW_{RGBb} , the equivalent width of the RGBb feature in the red-giant luminosity function relative to the underlying red-giant continuum. This led Nataf (2014) to revisit the issue: the predictions of EW_{RGBb} were shown to exceed the data, to an extent that depends on the stellar models used. Their results constrained suggested solutions to the issue of the offset between predicted and observed RGBb luminosities in GCs: that problem cannot be resolved by assuming an error in the adopted GC metallicity scale, the issue is more likely to be one pertaining to the physics of stellar models, e.g. the treatment of convection (Alongi et al., 1991).

Shape

For a long time, the only one firm observational evidence of the red-giant branch bump had been found in the metal-rich cluster 47 Tuc (King et al., 1985). This had given rise to questions about the limits of such a theoretical expectation: luminosity bumps had been theoretically produced under the assumption of a sharp discontinuity, but what happens if instead there was actually an extended partially mixed region?

Bono & Castellani (1992) investigated the influence on the bump of a smoothing of the chemical discontinuity, simulating a partial mixing by envelope overshooting from the convective unstable zone. They showed that, under reasonable assumptions

about the extension of the smoothed region, the occurrence of the bump remained a firm theoretical prediction. They also noted that the only sizeable difference was that increasing the smoothing resulted in a decrease of the bump luminosity, as a consequence of the earlier encounter between the hydrogen-burning shell and the increasing hydrogen. Ten years later, theoretical models still did not firmly predict the occurrence and efficiency of mixing processes beyond convective boundaries. This encouraged [Cassisi et al. \(2002\)](#) to study in detail how the sharpness and jump in the chemical composition impacted the RGBb, and more specifically its shape in the luminosity function. They found the change in the shape of the bump as a function of the smoothing length to be quite evident: the bump became more centrally peaked and more symmetric for an increase in the thickness of the smoothing region. This behaviour was associated with the abrupt change of the mean molecular weight, in the region across the chemical discontinuity, and to the strong dependence of the hydrogen-burning efficiency on μ (which then affects the stellar surface luminosity). The change of the hydrogen-burning efficiency was observed to be significantly lower in smoothed models than in canonical ones.

4.2 The Red-Giant Branch Bump as Seen by *Kepler* and *APOGEE*

The red-giant branch bump provides valuable information for the investigation of the internal structure of low-mass stars. Because current models are unable to accurately predict the occurrence and efficiency of mixing processes beyond convective boundaries, one can use the luminosity of the bump — a diagnostic of the maximum extension of the convective envelope during the first-dredge up — as a calibrator for such processes. By combining asteroseismic and spectroscopic constraints, we expand the analysis of the bump to masses and metallicities beyond those previously accessible using globular clusters. Our dataset comprises nearly 3000 red-giant stars

observed by *Kepler* and with APOGEE spectra. Using statistical mixture models, we are able to detect the bump in the average seismic parameters ν_{\max} and $\langle\Delta\nu\rangle$, and show that its observed position reveals general trends with mass and metallicity in line with expectations from models. Moreover, our analysis indicates that standard stellar models underestimate the depth of efficiently mixed envelopes. The inclusion of significant overshooting from the base of the convective envelope, with an efficiency that increases with decreasing metallicity, allows to reproduce the observed location of the bump. Interestingly, this trend was also reported in previous studies of globular clusters.

4.2.1 Introduction

The red-giant branch bump (RGBb) is a key observable that allows investigation of the internal structure of low-mass stars. It corresponds to a temporary drop in luminosity as a star evolves on the red-giant branch (RGB), leading to a local maximum in the luminosity function. The occurrence of the bump is related to the hydrogen-burning shell approaching and eventually advancing through the chemical composition gradient left over by the convective envelope at its maximum depth (see, e.g., [Christensen-Dalsgaard, 2015](#), and references therein). Since current stellar models are unable to accurately predict the occurrence and efficiency of mixing processes beyond convective boundaries, one can use the luminosity of the RGBb as a calibrator for such processes.

An improved description of mixing beyond convective envelopes has wide-ranging applications, e.g. from predicting the dredge-up efficiency on the RGB to a more accurate calibration of mass (hence age) of RGB stars based on the carbon-to-nitrogen ratio ([Salaris et al., 2015](#)). Also, better insights into the physics of mixing processes beyond the Schwarzschild border would have implications for the properties of the tachocline ([Christensen-Dalsgaard et al., 2011](#)) and the lithium depletion (e.g. [Baraffe et al., 2017](#)) in Sun-like stars, the evolution of asymptotic-giant branch

stars (Herwig, 2000; Marigo & Girardi, 2007), as well as the onset of blue loops in intermediate and massive stars (Alongi et al., 1991; Tang et al., 2014).

The RGBb has been known for a long time: first theoretically, through models of low-mass stars showing a temporary luminosity decrease during the evolution on the RGB (Thomas, 1967; Iben, 1968); then observationally, with its first empirical confirmation in the Galactic Globular Cluster (GGC) 47 Tuc by King et al. (1985). In particular, the RGBb characteristic luminosity is a diagnostic of the maximum extension of the convective envelope reached during the first dredge-up. Despite the wealth of theoretical and observational investigations, there is an ongoing debate as to a discrepancy between standard models' predictions and observations of the RGBb brightness in GCs (Fusi Pecci et al., 1990; Cassisi et al., 1997; Zoccali et al., 1999; Riello et al., 2003; Bjork & Chaboyer, 2006). However, recent studies seem to converge on the significance of this discrepancy and identify overshooting from the bottom of the convective envelope as a plausible solution to reproduce the observational constraints (Di Cecco et al. 2010; Cassisi et al. 2011; Troisi et al. 2011; Joyce & Chaboyer 2015 and Fu et al. 2018, who used the most recent empirical RGBb magnitudes from Nataf et al. 2013).

Alternative explanations explored in the literature are, for instance, differences in the chemical composition profile and / or opacities leading to a deeper convective region, together with other types of additional mixing (see, e.g., Bjork & Chaboyer, 2006; Cassisi et al., 2011). Besides, the observed discrepancy is also subject to some numerical influence due to differences among stellar evolution codes.

So far, the comparisons have been carried out primarily using Galactic GCs, hence exploring sub-solar metallicities and old ages only. The possible analysis of the bump with seismic data has been suspected for a while (see, e.g., Kallinger et al., 2010). Thanks to asteroseismic constraints coupled with spectroscopic constraints, we are able to lead a distance-independent study of the RGBb using thousands of field stars, hence exploring a much larger domain of mass, age, and metallicity.

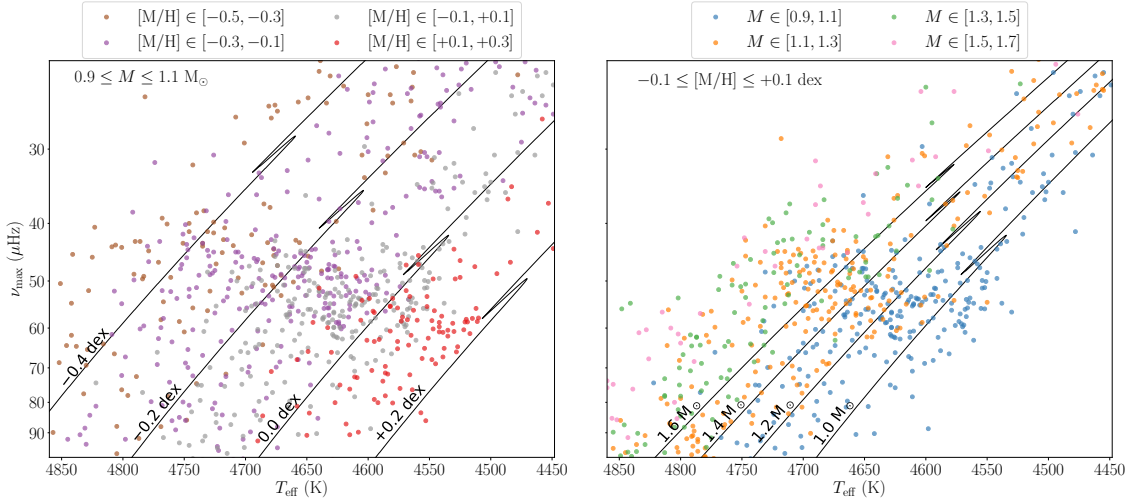


Figure 4.3: Left: $T_{\text{eff}} - \nu_{\text{max}}$ diagram, zoomed near the location of the bump. The coloured points correspond to the data (see Sec. 4.2.2) with a mass $M \in [0.9, 1.1] M_{\odot}$, and different metallicity ranges: $[-0.5, -0.3]$ (brown), $[-0.3, -0.1]$ (purple), $[-0.1, +0.1]$ (grey), $[+0.1, +0.3]$ dex (red). Evolutionary tracks computed using MESA (see Sec. 4.2.2) with $M = 1.0 M_{\odot}$, and $[M/H] = -0.4, -0.2, 0.0, +0.2$ dex (from left to right), without envelope overshooting, are shown in black. Right: same diagram with a metallicity $[M/H] \in [-0.1, +0.1]$ dex, and different mass ranges: $[0.9, 1.1]$ (blue), $[1.1, 1.3]$ (orange), $[1.3, 1.5]$ (green), $[1.5, 1.7] M_{\odot}$ (pink). Evolutionary tracks with $[M/H] = 0.0$ dex, and $M = 1.0, 1.2, 1.4, 1.6 M_{\odot}$ (from right to left), without envelope overshooting, are shown in black.

4.2.2 Observational and Theoretical Framework

Data

Our sample consists of red-giant stars observed by *Kepler* and with APOGEE spectra (Albaret et al., 2017) available (APOKASC collaboration). From the initial list of stars, we select those that are classified as RGB using the method by Elsworth et al. (2017), which uses the morphology of the power spectrum and more specifically the structure of the dipole-mode oscillations showing a mixed character in red-giant stars.

We use the global asteroseismic parameters extracted from the frequency-power spectrum of the light curves by means of Mosser et al. (2011a)’s data analysis method. These global seismic quantities are: the frequency of maximum oscillation power ν_{max} and the average large frequency spacing $\langle \Delta\nu \rangle$. We also make

use of the spectroscopically measured effective temperature T_{eff} , with the required post-calibration (details available online ¹), and of constraints on the photospheric chemical composition $[\text{Fe}/\text{H}]$ and $[\alpha/\text{Fe}]$ from SDSS DR13 (Albareti et al., 2017). Furthermore, for stars showing enhancement in the α elements, we compute a metallicity $[\text{M}/\text{H}]$ using the prescription described by Salaris et al. (1993) (which allows comparing to models calculated with solar-scaled abundances). Our final sample contains ≈ 3000 RGB stars.

Stellar masses are inferred using the Bayesian tool PARAM (Rodrigues et al., 2017). Asteroseismic constraints ν_{max} and $\langle\Delta\nu\rangle$ are included in the modelling procedure in a self-consistent manner, whereby $\langle\Delta\nu\rangle$ is calculated from a linear fitting of the individual radial-mode frequencies of the models in the grid. At this time, this approach has yielded masses / radii which show no systematic deviations to within a few percent of independent estimates (see, e.g., Miglio et al. 2016; Rodrigues et al. 2017; Handberg et al. 2017; Brogaard et al. 2018, who partially revisited the work by Gaulme et al. 2016).

The effects of potential systematic biases in the mass and metallicity scale are discussed in Sec. 4.2.4. In our dataset, the typical random uncertainties are of the order of 1.95% on ν_{max} , 0.05 μHz on $\langle\Delta\nu\rangle$, 70 K on T_{eff} , 0.04-0.07 dex on $[\text{M}/\text{H}]$, and 6-10% on mass.

Models

Evolutionary tracks and interior structures of RGB stars are computed using the stellar evolution code MESA (Paxton et al., 2011, 2013, 2015). We compute evolutionary tracks with M ranging from 1.0 to 1.6 M_{\odot} in steps of 0.2 M_{\odot} , and $[\text{M}/\text{H}]$ spanning from -0.4 to 0.2 dex in steps of 0.2 dex. The initial helium mass fraction Y_0 is determined assuming a linear chemical enrichment law $\Delta Y/\Delta Z$, with $Z_{\odot} = 0.01756$ and $Y_{0,\odot} = 0.26627$. The mixing-length parameter is taken equal to the solar-calibrated value $\alpha_{\text{MLT}} = 1.9658$. For more details about the physical

¹<http://www.sdss.org/dr13/irspec/parameters/>

inputs of the models, we refer the reader to [Rodrigues et al. \(2017\)](#), with the exception that we include diffusive convective core overshooting $\alpha_{\text{ov,core}} = 0.01$ during the main sequence. In this work, we focus on a diffusive type of mixing ([Herwig, 2000](#)), with three different overshooting efficiencies below the lower boundary of the convective envelope: $\alpha_{\text{ov,env}} = 0.00$ (no overshooting), $\alpha_{\text{ov,env}} = 0.025$, and $\alpha_{\text{ov,env}} = 0.05$. These would correspond to models with a fully-mixed overshooting region of the order of $\sim 0.3 H_P$ for $\alpha_{\text{ov,env}} = 0.025$, and $\sim 0.6 H_P$ for $\alpha_{\text{ov,env}} = 0.05$. The temperature gradient in the overshooting region is radiative.

Systematic effects due to different assumptions on the initial helium mass fraction, on the mixing-length parameter, and on convective core overshooting during the main sequence are presented in Sec. 4.2.4.

Lastly, ν_{max} is estimated through the seismic scaling relations, with the following solar references: $\nu_{\text{max},\odot} = 3090 \mu\text{Hz}$ and $T_{\text{eff},\odot} = 5777 \text{ K}$. As for $\langle \Delta\nu \rangle$, we follow the average large frequency definition described by [Rodrigues et al. \(2017\)](#) (see Sec. 4.2.2), where the individual radial-mode frequencies are computed with GYRE ([Townsend & Teitler, 2013](#)).

The $T_{\text{eff}} - \nu_{\text{max}}$ diagrams of the data used in this work, overlaid with a few evolutionary tracks, are displayed in Fig. 4.3, where the RGBb appears as a clear feature in ν_{max} .

It is worth noticing that the *Kepler* and APOGEE target selection was primarily based on colour and magnitude criteria that, for the masses / metallicities explored in this study, are not expected to affect the recovered position of the RGBb (see, e.g., [Farmer et al., 2013](#); [Miglio et al., 2014](#); [Pinsonneault et al., 2014](#)). Moreover, we do not expect significant selection effects due to the length and cadence of *Kepler*'s observations, in the ν_{max} (hence $\log g$) range where we identify the bump. Biases against high- $\log g$ stars are expected if one were to extend the domain to frequencies closer to the Nyquist frequency of *Kepler* long-cadence data ($\nu_{\text{max}} \simeq 283 \mu\text{Hz}$), which falls outside the domain relevant for our analysis. Also, if one were to extend

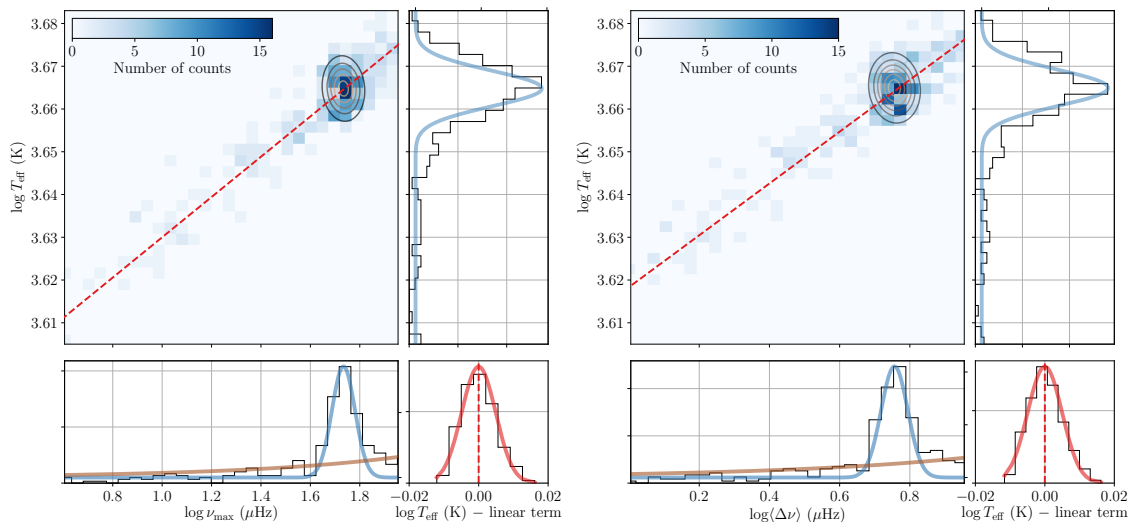


Figure 4.4: Probability functions applied to our dataset in the $\log T_{\text{eff}} - \log \nu_{\text{max}}$ (left) and $\log T_{\text{eff}} - \log \langle \Delta \nu \rangle$ (right) planes; with $0.9 \leq M \leq 1.1 M_{\odot}$ and $-0.1 \leq [M/H] \leq +0.1$ dex. 2D histograms are plotted, where the colour scale indicates the number of stars and the ellipses show the location of the bump, as determined by the mixture model technique. 1D histograms of $\log \nu_{\text{max}}$ (or $\log \langle \Delta \nu \rangle$) and $\log T_{\text{eff}}$ are also shown in black in the bottom and right plots, respectively. The two components of the RGBb bivariate Gaussian are displayed with blue lines. The brown line correspond to the RGB outliers' rising exponential in $\log \nu_{\text{max}}$ (or $\log \langle \Delta \nu \rangle$); while the red dashed line shows the linear term modelling the RGB background. The small plot at the bottom right corner depicts the difference between $\log T_{\text{eff}}$ and the RGB linear term, hereby illustrating the normal scatter.

to low- $\log g$ values, considerably lower than the red clump (e.g. $\nu_{\text{max}} \lesssim 10 \mu\text{Hz}$), biases may start to be significant due to the limited duration of the observations and to the target selection being biased against intrinsically luminous stars (see, e.g., [Farmer et al., 2013](#); [Pinsonneault et al., 2014](#)).

It is also worth stressing that we have a sample that is little, if at all, contaminated by non-RGB stars, since core-helium burning stars have been identified and removed from the sample using the evolutionary-dependent signature of gravity modes in the oscillation spectra ([Bedding et al., 2011](#); [Elsworth et al., 2017](#)).

4.2.3 Determination of the RGB Bump Location

To detect and characterise the RGBb, we use a statistical mixture model ([Hogg et al., 2010](#)) to estimate its position in ν_{max} and $\langle \Delta \nu \rangle$.

The mixture model approach is a statistical framework allowing simultaneous consideration of multiple models, or hypotheses, with reference to a single dataset. In this context, they are a means of distinguishing inliers, the RGBb overdensity, and outliers, the RGB background, i.e. the remaining stars not belonging to the bump. We apply our fitting method in the $\log T_{\text{eff}} - \log \nu_{\text{max}}$ and $\log T_{\text{eff}} - \log \langle \Delta \nu \rangle$ planes, where the RGBb appears as a dense and slightly sloping horizontal strip in a restricted bin of mass and metallicity.

We employ one common strategy for our dataset and for simple synthetic populations — mono-mass, mono-metallicity — derived from MESA models. In both cases, three probability functions are at work: the RGBb foreground is described by a bivariate normal distribution with a negative correlation; while a rising exponential in $\log \nu_{\text{max}}$ (or $\log \langle \Delta \nu \rangle$) and a linear term with a normally distributed scatter are used for the remaining population of RGB outliers. These probability functions are depicted in Fig. 4.4. Notably, considering $1/\nu_{\text{max}}$ as a proxy of the luminosity ($1/\nu_{\text{max}} \propto R^2$, where R is the radius), one can appreciate that the behaviour of the RGB background follows the same trend as the luminosity function of GCs (with a decreasing number of stars with increasing luminosity).

The mixture model likelihood function is then marginalised using a Markov Chain Monte-Carlo process, by means of the Python package `emcee` (Foreman-Mackey et al., 2013), producing posterior probability distributions for our set of ten parameters: the RGBb location in $\log \nu_{\text{max}}$ (or $\log \langle \Delta \nu \rangle$) and $\log T_{\text{eff}}$, the corresponding RGBb standard deviations, the correlation of the bivariate Gaussian, the exponential parameter, the linear term’s slope, intercept and standard deviation, and the mixture model weighting factor.

4.2.4 Results

As the RGBb properties are expected to be highly dependent on stellar parameters, we divide our sample in the following intervals of mass: $[0.9, 1.1]$, $[1.1, 1.3]$,

[1.3, 1.5], and [1.5, 1.7] M_{\odot} ; and metallicity: $[-0.5, -0.3]$, $[-0.3, -0.1]$, $[-0.1, +0.1]$, and $[+0.1, +0.3]$ dex. Out of all 16 mass and metallicity bins, we can detect and robustly characterise the RGBb position in both ν_{\max} and $\langle\Delta\nu\rangle$ in nine of them, with the main limiting factor being the low number of stars in some of the bins. The typical uncertainties (68% credible region) on the RGBb position in ν_{\max} and $\langle\Delta\nu\rangle$ go from 1% to 5% for the most poorly populated bins.

Trends with Mass and Metallicity

We investigate the location of the observed RGBb as a function of M and $[M/H]$. Both the ν_{\max} and $\langle\Delta\nu\rangle$ of the RGBb decrease with increasing stellar mass and decreasing metallicity (Fig. 4.5 and 4.6).

From theoretical models, one expects that hotter stars, as a result of a higher mass or a lower metallicity, have a shallower convective envelope, hence a higher RGBb luminosity. This increase in luminosity is typically accompanied by an increase in radius. The latter explains the decrease in ν_{\max} and $\langle\Delta\nu\rangle$, which are strongly dependent on R ($\nu_{\max} \propto R^{-2}$, $\langle\Delta\nu\rangle \propto R^{-3/2}$).

In conclusion, whether in terms of ν_{\max} or $\langle\Delta\nu\rangle$, the data show a RGBb having trends with mass and metallicity that are qualitatively consistent with expectations. We now proceed to a quantitative comparison between observations and predictions.

A Preliminary Calibration of the Envelope Overshooting Parameter

We generate simple synthetic populations — mono-mass, mono-metallicity — from MESA models (see Sec. 4.2.2). For each track, we create a population of 3000 stars, assuming a uniform age distribution from the base to the tip of the RGB, and we interpolate in age to get ν_{\max} , $\langle\Delta\nu\rangle$, and T_{eff} . A normally distributed noise is then added, using the typical uncertainties on each of these properties (see Sec. 4.2.2). Because we consider a uniform age distribution in restricted mass ranges ($[0.9, 1.1]$, $[1.1, 1.3]$, $[1.3, 1.5]$, and $[1.5, 1.7]$ M_{\odot}), the Galactic star-formation rate should not have an influence on our results.

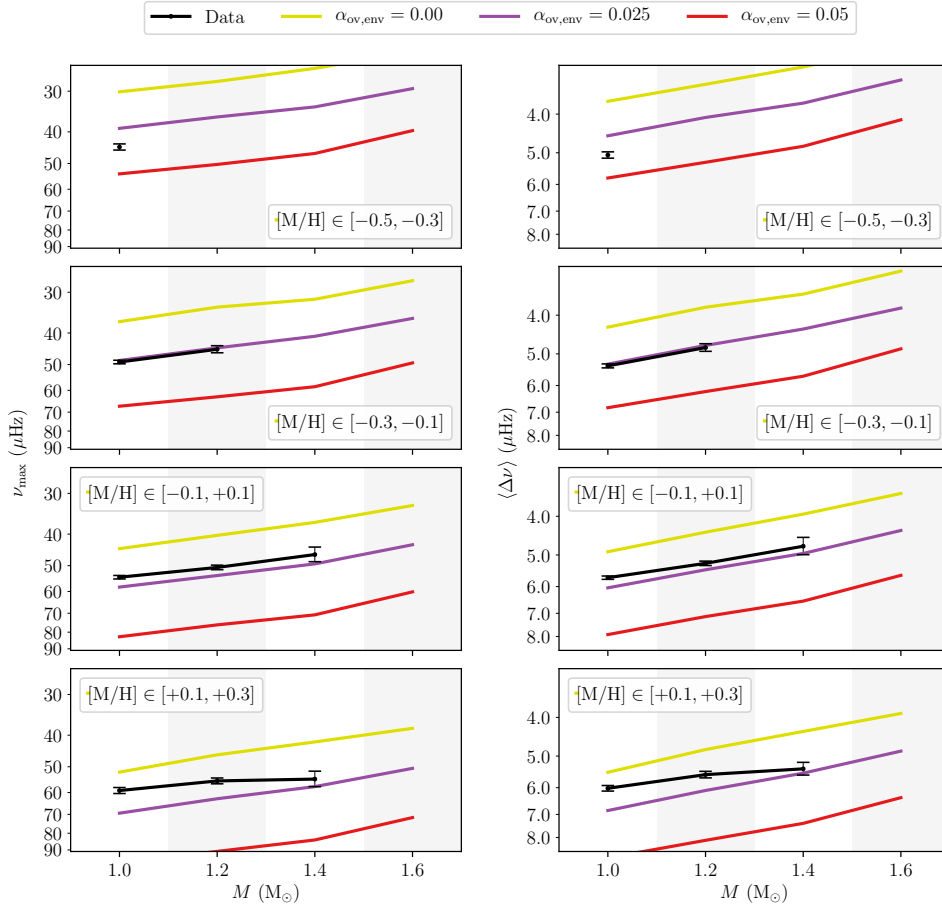


Figure 4.5: Location of the RGBb in ν_{\max} (left) and in $\langle \Delta \nu \rangle$ (right), in our dataset (black; see Sec. 4.2.2), and its corresponding 68% credible region, and simple synthetic populations with different envelope overshooting efficiencies: $\alpha_{\text{ov,env}} = 0.00$ (yellow), $\alpha_{\text{ov,env}} = 0.025$ (purple), and $\alpha_{\text{ov,env}} = 0.05$ (red); as a function of mass, for different metallicity ranges: $[-0.5, -0.3]$, $[-0.3, -0.1]$, $[-0.1, +0.1]$, and $[+0.1, +0.3]$ dex (from top to bottom). The background bands indicate the mass bin, in which the bump position has been estimated.

We then compare the RGBb observed locations with those that are predicted by theory, for different envelope overshooting efficiencies. To take into account the latter, we use a diffusive type of mixing in MESA, characterised by an adjustable parameter $\alpha_{\text{ov,env}}$ (see Sec. 4.2.2).

The comparison of the observed and predicted RGBb mean value in ν_{\max} and $\langle \Delta \nu \rangle$, as a function of mass and metallicity, is displayed on Fig. 4.5 and 4.6. First and foremost, it is clear that one would need to consider models with significant

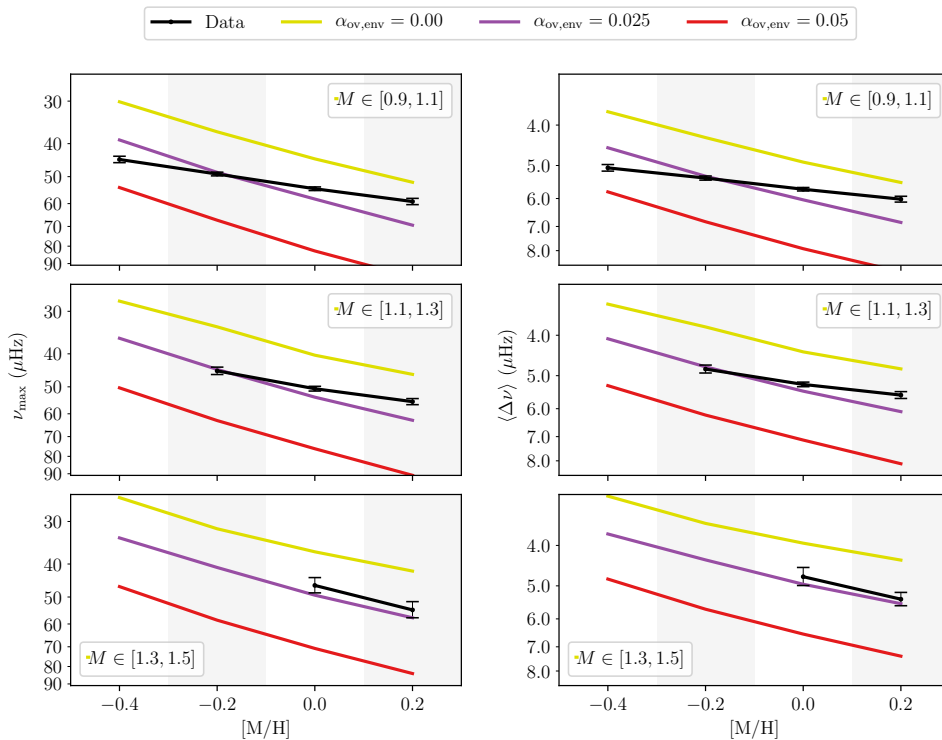


Figure 4.6: Same as Fig. 4.5; as a function of metallicity, for different mass ranges: $[0.9, 1.1]$, $[1.1, 1.3]$, and $[1.3, 1.5]$ M_{\odot} (from top to bottom).

overshooting from the base of the convective envelope to reproduce the observations for both global seismic parameters. This conclusion holds whether we tackle the issue in terms of mass (Fig. 4.5) or metallicity (Fig. 4.6).

Subsequently, focusing our attention on ν_{\max} , we note that the most metal-poor stars are likely to suggest a slightly more substantial overshooting efficiency, which would be close to $\alpha_{\text{ov,env}} = 0.025$ or even greater than that for stars with $[M/H] \in [-0.5, -0.3]$. Besides, we also checked whether the trend at low metallicity is dominated by α -rich stars, yet only considering stars with $[\alpha/\text{Fe}] < 0.05$ dex had no influence on the observed trends. As we go towards higher metallicities, a shallower envelope overshooting ($\alpha_{\text{ov,env}} < 0.025$) is suggested. Similar conclusions are reached from $\langle \Delta \nu \rangle$. Our analysis clearly shows that, for the models considered here, the extra-mixing efficiency for low-mass stars ($M \leq 1.3 M_{\odot}$) decreases as metallicity increases.

Finally, it is also apparent that the suggested overshooting efficiency never goes as far as $\alpha_{\text{ov,env}} = 0.05$ — equivalent to a fully-mixed overshooting region of $\sim 0.6 H_{\text{P}}$ — within the limits of our dataset, implicitly defining an upper bound for the extent of mixing needed. This might change if we were to consider masses and metallicities similar to those of RGB stars in globular clusters.

Assessing Other Systematic Effects

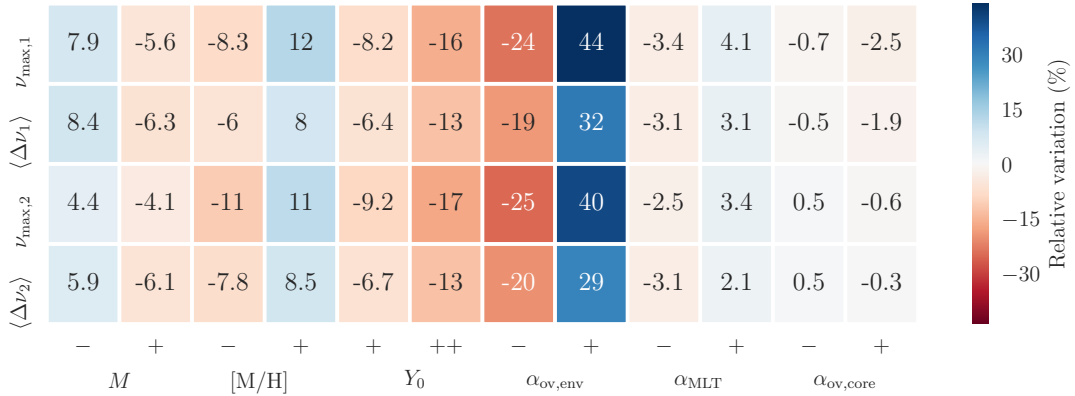


Figure 4.7: Heatmap illustrating the relative variations (%) of the bump’s location in ν_{max} and $\langle \Delta \nu \rangle$, with two different sets of default parameters. Full details are provided in the text.

Uncertainties on additional parameters, other than the extent of mixing beyond the convective envelope, could also affect the position of the RGBb in ν_{max} and $\langle \Delta \nu \rangle$. For this reason, we aim to assess the bias on the estimation of ν_{max} and $\langle \Delta \nu \rangle$ induced by each of the following parameters: M , $[M/H]$, Y_0 , $\alpha_{\text{ov,env}}$, α_{MLT} , and $\alpha_{\text{ov,core}}$. To that end, all parameters are fixed excluding the one whose effect we wish to quantify. We test two sets of default parameters:

1. $M = 1.40 M_{\odot}$, $[M/H] = 0.0$ dex;
2. $M = 1.20 M_{\odot}$, $[M/H] = -0.2$ dex.

A variation of 10% in mass affects the ν_{max} and $\langle \Delta \nu \rangle$ of the bump in the order of 6%. Changing the metallicity (± 0.1 dex) or the initial helium mass fraction (+0.02, 0.04) has more impact on ν_{max} than on $\langle \Delta \nu \rangle$: 10% and 8.5% against 7% and

6%, respectively. As expected, as Y_0 increases, stars are hotter and brighter (e.g. [Fagotto et al., 1994](#)), and the RGBb ends up at a higher luminosity. Unquestionably, the envelope overshooting efficiency (± 0.025) has the most significant effect on the position of the bump, again greater for ν_{\max} : about 34% compared to $\sim 25\%$ in $\langle \Delta\nu \rangle$. The mixing-length parameter (± 0.1) has a mild repercussion, of a few percent, whether on ν_{\max} or $\langle \Delta\nu \rangle$. Moreover, both fits of colour-magnitude diagrams with GCs and hydrodynamics simulations do not suggest changes in α_{MLT} significantly larger than ± 0.1 (see, e.g., [Trampedach et al., 2014](#); [Salaris et al., 2018](#)). Finally, the convective core overshooting efficiency (± 0.01) during the main-sequence phase does not have any notable effect on the RGBb position for a mass and a metallicity up to $1.4 M_{\odot}$ and 0.3 dex, which draw the limits of the current work’s dataset. The relative variations are portrayed with a heatmap in Fig. 4.7.

A combination of each of these parameters might be able to account for the discrepancy between the observed and predicted RGBb position, but it seems unlikely.

The helium-to-metals enrichment ratio (see Sec. 4.2.2) may have a significant effect on the estimate of the extra mixing required to fit the observations. Indeed, at fixed Z , an increase in $\Delta Y/\Delta Z$ induces a greater initial helium abundance, thus a decrease in the ν_{\max} and $\langle \Delta\nu \rangle$ of the bump (see Fig. 4.7). This Y_0 increase is further amplified at high metallicities, hence the corresponding conclusions might suggest a greater amount of overshooting from the lower boundary of the convective envelope. If one were to explore lower values of Y_0 , the discrepancy would be reduced but these would have to be sub-big-bang-nucleosynthesis values (see [Troisi et al., 2011](#)).

4.2.5 Conclusions

First of all, we report the detection of the RGBb in stars observed by *Kepler* with APOGEE spectra, corresponding to the widest mass and metallicity domain explored thus far. Previous studies of the bump in GGCs could hardly illustrate the expected trends of the RGBb luminosity with mass and metallicity, because of their

analysis being restricted to predominantly clusters with sub-solar metallicities. The combination of asteroseismology and spectroscopy provides us with the resources required to finally overcome this barrier.

We show that the observed RGBb location in ν_{\max} and $\langle\Delta\nu\rangle$ reveals trends with mass and metallicity in line with expectations from models. However, we note that models without envelope overshooting are in disagreement with observations. This result is confirmed whether we approach the problem in terms of ν_{\max} or $\langle\Delta\nu\rangle$. Indeed, the most metal-poor stars seemingly suggest a mixing extent of $\alpha_{\text{ov,env}} \geq 0.025$; while a lower amount of overshooting, $0.00 \leq \alpha_{\text{ov,env}} \leq 0.025$, seems more appropriate for their metallicity-enhanced counterparts. Hence, for both seismic observables, we see hints of a possible dependence of the extra-mixing efficiency on metallicity. Finally, for the sample considered in this work, a strong efficiency such as $\alpha_{\text{ov,env}} = 0.05$ can be set aside, showing that there is an upper limit to the extent of mixing needed to bring an agreement between models and observations. However, if we were to consider stars in globular clusters with masses $\sim 0.85 M_{\odot}$ and metallicities $[M/H] \sim -1 - -2$ dex, it could be that we would find even larger overshooting efficiencies.

Interestingly, similar evidence for additional mixing is found in GCs. [Cassisi et al. \(2011\)](#) and [Fu et al. \(2018\)](#) mentioned that the offset between predicted and observed RGBb would disappear with the inclusion of overshooting in the order of $0.25 H_p$ at the base of the convective envelope. These works, as well as [Di Cecco et al. \(2010\)](#), [Troisi et al. \(2011\)](#) and [Joyce & Chaboyer \(2015\)](#), also found an increasing discrepancy when moving from metal-rich to metal-poor GCs. To alleviate this discrepancy, [Fu et al. \(2018\)](#) mentioned the genuine possibility for the extra-mixing efficiency to be larger than their adopted value in metal-poor stars. This assumption seems to tally with our preliminary finding of a possible dependence of envelope overshooting on metallicity. The following sections in this chapter stem from this result: Sec. 4.3 aims at expanding the metallicity range of our envelope

overshooting calibration by studying Galactic and Magellanic Clouds clusters, and Sec. 4.4 discusses ways of relating all the observational evidence with expectations from hydrodynamical simulations, to work towards a more physically-motivated prescription of convective overshooting.

Furthermore, our conclusion is strengthened by an assessment of systematic effects on the RGBb position in ν_{\max} and $\langle\Delta\nu\rangle$, presented in Sec. 4.2.4. That said, it is crucial to bear in mind that further tests are needed for a robust calibration of the amount of extra mixing from the base of the convective envelope. These tests should exhaustively consider all conceivable systematic biases, including the comparison among various stellar evolution codes and, e.g., different helium-to-metals enrichment rates $\Delta Y/\Delta Z$.

In this regard, the second Data Release of *Gaia* will allow a significant step forward in characterising the bump. With precise and accurate parallaxes available, one can use additional diagnostics to avoid, or mitigate, theoretical and observational uncertainties, e.g. by comparing the RGBb luminosity with that of the zero-age horizontal branch or the main-sequence turn off.

Moreover, by considering the full *Kepler* dataset, and data from K2 and TESS, it will soon be possible to couple astrometric and spectroscopic constraints with asteroseismic data in significantly larger samples of stars, thus providing further insights into the efficiency of internal mixing processes in cool stars.

4.3 The Red-Giant Branch Bump as Seen by Star Clusters

4.3.1 Introduction

The findings of [Khan et al. \(2018\)](#) (Sec. 4.2), regarding a possible trend of the overshooting efficiency with metallicity, motivated additional work in this direction to further constrain convective boundary mixing processes below the envelope of red-

giant stars. In this respect, star clusters in the Milky Way and in the Magellanic Clouds provide a wealth of data for expanding the study of the red-giant branch bump to populations with metallicities lower than that of field stars observed by *Kepler* (see also Sec. 4.1.2 for a discussion of former studies having analysed the RGBb in globular clusters).

4.3.2 Observational and Theoretical Framework

Data

Globular Clusters Observations for globular clusters are taken from the public catalogue by [Nardiello et al. \(2018\)](#). The latter contains high-precision stellar astrometry and photometry (F275W, F336W, F438W, F606W, and F814W) from WFC3/UVIS and ACS/WFC observations of 56 GCs, mainly based on images collected within the ‘*HST* Legacy Survey of Galactic Globular Clusters: Shedding UV Light on Their Populations and Formation’ (GO-13297, PI: Piotto), and the ‘ACS Survey of Galactic Globular Clusters’ (GO-10775, PI: Sarajedini).

For each cluster, we only keep objects with a probability membership higher than 90%, in order to separate cluster stars from field stars. In each photometric band, we also remove stars with negative magnitude values (-99) which probably indicate that a measurement was not possible in this specific band. To go further, one could also make a more specific selection of well-measured stars depending on which photometric band is being used. This would be performed as done by [Nardiello et al. \(2018\)](#), see also [Milone et al. 2012](#)). At the current stage of this work, however, this latter selection has not been applied yet as it would require further tests to properly select stars that satisfy each individual criterion described in these papers.

Magellanic Clouds Clusters Observational data for clusters in the Magellanic Clouds were provided by Leo Girardi (private communication). All clusters have photometry in the F555W and F814W bands, again based on images from the Hubble Space Telescope. Some of them have magnitudes in additional photometric

bands: F160W, F336W, and F435W; but we will not use them within this work. The data files were already cleaned from likely non-stellar objects, but could still be slightly contaminated by stars in the Large Magellanic Cloud field. A workaround to this is to remove stars in the outskirts of each cluster, and see if the results remain unchanged.

Models

On the other side, we compute simulations of each cluster, either in the form of isochrones or synthetic populations, with TRILEGAL (TRIdimensional modeL of thE GALaxy; [Girardi et al., 2005](#)), a population synthesis code for simulating the photometry of any Galaxy field. TRILEGAL allows one to generate mock stellar catalogues for a galaxy or any stellar object at a fixed distance (e.g. cluster), with high flexibility in the inputs: grids of stellar evolutionary tracks, tables of bolometric corrections, initial mass function, star-formation rate and age-metallicity relation, and the geometry of the Galaxy components (if appropriate).

In our case, two main sets of evolutionary tracks, spanning the evolution from the pre-main sequence to the first thermal pulse, are considered (although, in the remainder of this section, only PARSEC tracks have been used for now):

- PARSEC tracks ([Bressan et al., 2012](#)), which are computed for a scaled-solar composition and follow the $Y = 0.2485 + 1.78Z$ chemical enrichment relation. The present solar metal content is $Z_{\odot} = 0.0152$. Regarding envelope overshooting, they use $\Lambda_e = 0.05 H_P$ for $M < M_{O1}$, $\Lambda_e = 0.7 H_P$ for $M > M_{O2}$, and a smooth transition between the two critical masses M_{O1} and M_{O2} (see Fig. 3 in their paper to see how these masses vary with metallicity).
- MESA tracks ([Paxton et al., 2011, 2013, 2015, 2018](#)), which are computed for a scaled-solar composition (although we are planning to also compute α -enhanced tracks in the near future) and follow the $Y = 0.2485 + 1.16Z$ chemical

enrichment law. The present solar metal content is $Z_{\odot} = 0.01493$. The main difference with PARSEC tracks is that because we compute MESA tracks ourselves, we can also vary the type and efficiency of convective boundary mixing, as detailed in Sec. 2.2.1.

We use the library of bolometric corrections OBC described in [Girardi et al. \(2002\)](#), and expanded by [Marigo et al. \(2017\)](#).

Since we are only interested in clusters, we use simplified relations for the star-formation rate and age-metallicity distributions, given that stars within a cluster have the same age and chemical composition. Namely, at fixed metallicity, we use a gate function $y = f(\tau)$ where:

$$y = 1 \text{ for } \tau_{\text{cluster}} - 0.05 \leq \tau \leq \tau_{\text{cluster}} + 0.05, \quad (4.1)$$

$$y = 0 \text{ for } \tau < \tau_{\text{cluster}} - 0.05 \text{ or } \tau > \tau_{\text{cluster}} + 0.05, \quad (4.2)$$

with τ_{cluster} being the cluster age.

Finally, the initial mass function does not matter here as we are only interested in red-giant stars spanning a very small mass range, and we do not have to specify the geometry of the Galaxy components either since we are looking at clusters. Instead, we specify that we want to simulate an object at fixed distance, with several input values.

Observational Constraints from the Literature In the case of globular clusters in our Galaxy, we follow [Baumgardt & Hilker \(2018\)](#) and use observational constraints from different sources:

- ages from [Baumgardt \(2017\)](#), which includes ages from [VandenBerg et al. \(2013\)](#) and from the literature;
- metallicities from [Carretta et al. \(2009\)](#) and $[\alpha/\text{Fe}]$ abundances reported in

Cluster	Age (Gyr)	[Fe/H]	[α /Fe]	E(B–V)	Distance (pc)	Mass (M_{\odot})
NGC 7078	12.75	-2.33	0.40	0.10	9900	4.53×10^5
NGC 5272	11.75	-1.50	0.34	0.01	10060	3.94×10^5
NGC 6584	—	-1.50	—	0.10	13180	9.07×10^4
NGC 5904	11.50	-1.33	0.38	0.03	7500	3.72×10^5
NGC 0362	10.75	-1.30	0.30	0.05	9400	3.45×10^5
NGC 1261	—	-1.27	—	0.01	15490	1.67×10^5
NGC 1851	11.00	-1.18	0.38	0.02	11400	3.02×10^5
NGC 2808	11.00	-1.18	0.33	0.22	9800	7.42×10^5
NGC 6723	12.50	-1.10	0.50	0.05	8200	1.57×10^5
NGC 6362	12.50	-1.07	—	0.09	8000	1.47×10^5
NGC 6171	12.00	-1.03	0.49	0.33	6090	8.70×10^4
NGC 6838	11.00	-0.82	0.40	0.25	6600	4.91×10^4
NGC 0104	11.75	-0.76	0.42	0.04	4410	7.79×10^5
NGC 6352	—	-0.62	0.20	0.22	5890	9.38×10^4
NGC 6496	—	-0.46	—	0.15	11690	1.06×10^5
NGC 6388	11.75	-0.45	0.22	0.37	11000	1.06×10^6
NGC 6441	11.00	-0.44	0.21	0.47	12000	1.23×10^6
NGC 6624	11.25	-0.42	—	0.28	7000	7.31×10^4
NGC 6304	—	-0.37	—	0.54	9400	2.77×10^5
NGC 5927	10.75	-0.29	—	0.45	8400	3.54×10^5

Table 4.1: Properties of the Galactic globular clusters considered in this study: age, metallicity, [α /Fe], reddening, distance, and mass.

Table A1 of [Carretta et al. \(2010\)](#) (which come from various sources);

- reddenings from [Harris \(1996, 2010 edition\)](#);
- distances from literature and a few fitted by [Baumgardt & Hilker \(2018\)](#);
- and masses from [Baumgardt & Hilker \(2018\)](#).

Additional effects related to the presence of multiple populations in GCs have not been considered in this study (see, e.g., [Lagioia et al., 2018](#); [Fu et al., 2018](#)).

Meanwhile, for Magellanic Clouds clusters, we currently have a reduced dataset with ages and metallicities coming from various sources, that is nevertheless sufficient to compute isochrones.

Summaries of the observational parameters for the Galactic globular clusters and Magellanic Clouds clusters considered in this study are given in Tables 4.1 and 4.2.

Cluster	Age (Gyr)	[Fe/H]	Location	Notes	Reference
NGC 1806	0.50	-0.71	LMC	—	Dirsch et al. (2000)
NGC 0419	1.40	-0.70	SMC	dual clump	Cabrera-Ziri et al. (2020)
NGC 1846	1.73	-0.49	LMC	dual clump	Rubele et al. (2013)
NGC 1783	1.80	-0.45	LMC	dual clump	Zhang et al. (2018)
NGC 1751	1.40	-0.44	LMC	dual clump	Rubele et al. (2011)
NGC 1978	2.00	-0.38	LMC	—	Piatti & Bailin (2019)

Table 4.2: Properties of the Magellanic Clouds clusters considered in this study: age, metallicity, location (Large or Small Magellanic Cloud), notes on possible specificities of the clusters, and references providing the age and metallicity values (see references therein for the actual sources).

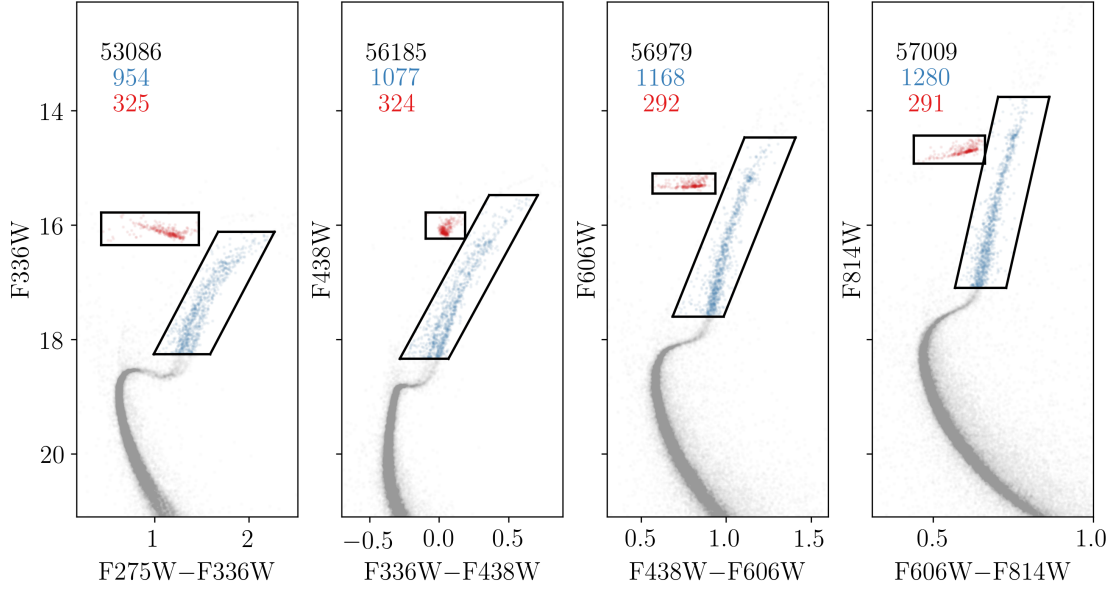
4.3.3 Methods

Determination of the Red-Giant Branch Bump and Red Clump Locations

First, we need to separate between first-ascent red-giant branch stars and core-helium burning stars. This distinction is done by eye, by drawing shapes around the red-giant branch and the core-helium burning phases. In some cases, these two selections can overlap, hence we have to be careful in how much to trust the reliability of this distinction. It could be that for some clusters, the overlap is so important that we cannot reliably apply this approximate selection. Examples are shown in Fig. 4.8 for NGC 0362 and NGC 6441.

The plan after that is to use a similar method as the one described in [Khan et al. \(2018\)](#) to extract the position of the bump. However, since we are now looking at colour-magnitude diagrams and clusters (in opposition to seismic diagrams and field stars), it would be relevant to adapt the different probability functions to the new distributions in magnitude and colour. Preliminary results from statistical mixture models are shown in Fig. 4.9. The statistical method is able to estimate the position of the bump for NGC 0362, although the probability functions assumed in the model are not perfectly suited to the observed distributions. In some other cases (e.g. NGC 6441), the method struggles more and fails at finding the overdensity that actually corresponds to the RGBb. One of the issues is that when separating the RGB and

Number of stars before selection criteria (membership probability): 144319



Number of stars before selection criteria (membership probability): 394279

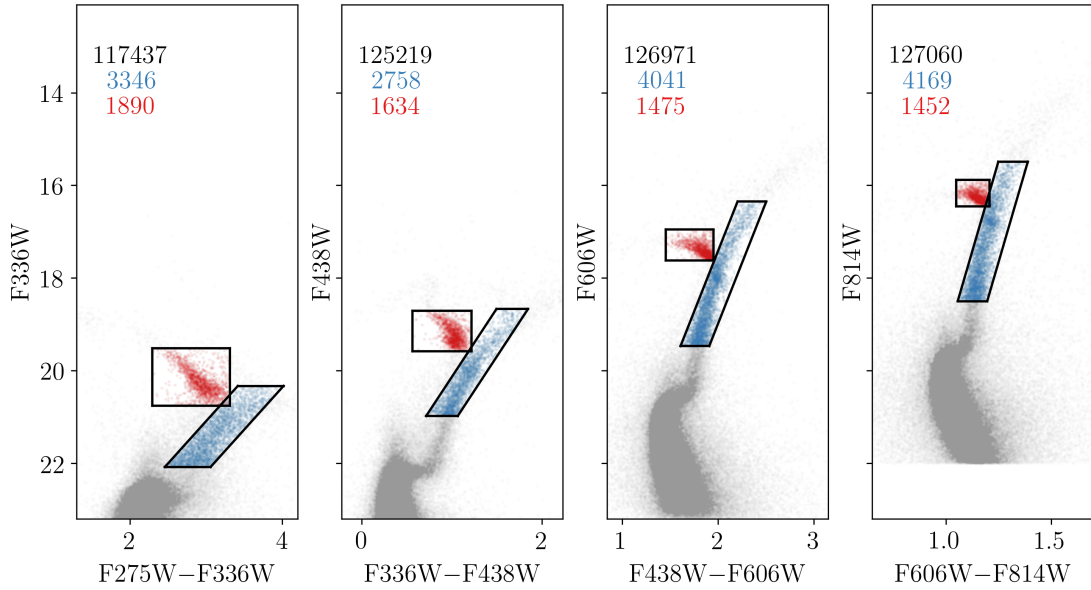


Figure 4.8: Colour-magnitude diagrams for NGC 0362 (top panel) and NGC 6441 (bottom panel) with red-giant branch stars in blue and core-helium burning stars in red, circled by their respective selection boxes. The number of red-giant branch and red clump stars is indicated in each individual panel, with the same colour. From left to right, we move from ultraviolet to near-infrared filters.

the RC, part of the RGBb is lost and/or mixed up with the clump, which can lead to an apparent sharp cutoff at the blue end of the CMD. These preliminary results encourage us to refine our method, so that it is more adapted to the parameter space

covered by clusters. This will be done in a future work.

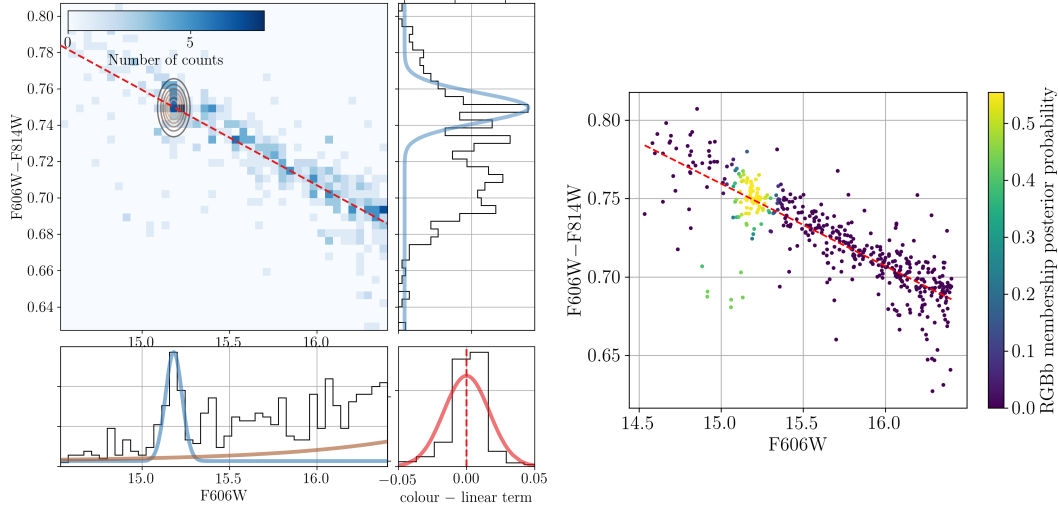


Figure 4.9: Left: Probability functions applied to NGC 0362 in the $F606W - (F606W - F814W)$ plane. 2D histograms are plotted, where the colour scale indicates the number of stars and the ellipses show the location of the bump, as determined by the mixture model technique. 1D histograms of $F606W$ and $(F606W - F814W)$ are also shown in black in the bottom and right plots, respectively. The two components of the RGBb bivariate Gaussian are displayed with blue lines. The brown line correspond to the RGB outliers’ rising exponential in $F606W$; while the red dashed line shows the linear term modelling the RGB background. The small plot at the bottom right corner depicts the difference between $(F606W - F814W)$ and the RGB linear term, hereby illustrating the normal scatter. Right: Final colour-magnitude diagram for RGB stars, with the colour scale indicating the RGBb membership probability.

Population Synthesis and Isochrone Fitting with TRILEGAL for Galactic Globular Clusters

As discussed in Sec. 4.3.2, in principle we have all the observational constraints we need to simulate a detailed synthetic population for each Galactic globular cluster of interest. Nevertheless, in practice, the simulations do not exactly fit the observations. In particular, the agreement with observations is worse in the case of ultraviolet passbands — the shape of the CMD starts to be significantly different. As it is, the current simulations aim at generally reproducing the density of stars in each evolutionary phase, but potential scatter induced by observational errors is not considered yet and will be added in a future step.

As a temporary workaround, we decided to focus first on fitting simple isochrones, instead of more detailed synthetic populations that depend on many different inputs. For each cluster, we generate a series of isochrones with ages from 10 to 13 Gyr, with a step of 0.5 Gyr, a metallicity fixed at the cluster’s observed value, and a V -band extinction equal to zero so that we can adjust it later. These isochrones are also generated for different mass-loss efficiencies ranging from 0 to 1, with a step of 0.05. The mass-loss prescription adopted here is that of [Reimers \(1975\)](#). The zero-age horizontal branch sequence (ZAHB) is defined by keeping the first core-helium burning model of the 10-Gyr isochrone for each mass-loss efficiency considered. For all isochrones (10-13 Gyr), we then consider the evolutionary stages corresponding to the main sequence, the subgiant branch, and the red-giant branch, with a mass-loss efficiency $\eta = 0.2$.

In the case of observations, we apply flags on the membership probability ($> 90\%$) and on the photometric uncertainties (< 0.03 , and if more than 25000 stars remain we further constrain the selection to < 0.015). In addition, we also get rid of clear outliers, removing objects that are 10σ away from the median colour. Finally, we de-redden the magnitudes in the passbands considered, i.e. F606W and F814W in our case.

Our isochrone-fitting procedure follows the method described in [VandenBerg et al. \(2013\)](#). First, we adjust the distance modulus so that the simulated ZAHB agrees well with the fainter end of the observed horizontal branch (Fig. 4.10). Then, we determine the observed turn-off colour, by defining two fiducial sequences near the turn off and the upper main sequence, as illustrated in Fig. 4.11. The turn-off colour is taken as the bluest point of the corresponding fiducial sequence, while the upper main-sequence magnitude is taken as the point that is 0.05 redder than the turn off. Following this, we overlay all the shifted isochrones on the observed colour-magnitude diagram, in order to determine which isochrone best fits the observations

(see Fig. 4.12). Finally, we end up with Figs. 4.13, 4.14 and 4.15, where we show the best-fit isochrone overlaid on the observed CMD for all the Galactic globular clusters contained in our sample.

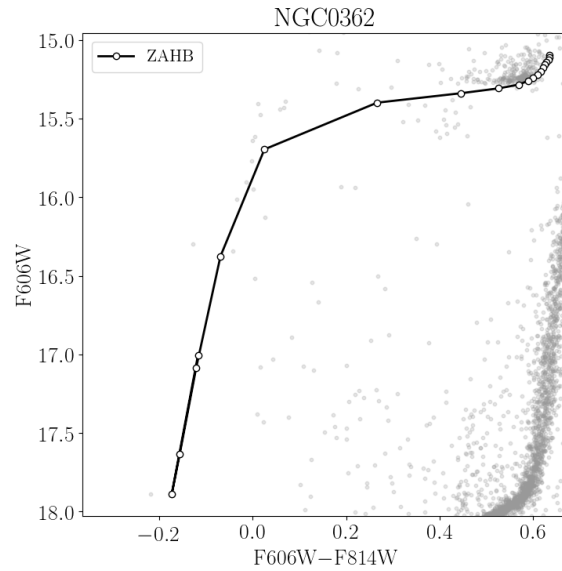


Figure 4.10: Colour-magnitude diagram zoomed near the horizontal branch for NGC 0362. The observations are shown with grey points. The black line shows the simulated zero-age horizontal branch, and each circle corresponds to a specific mass-loss efficiency. The circles at the brighter (fainter) end corresponds to lower (high) mass-loss efficiencies.

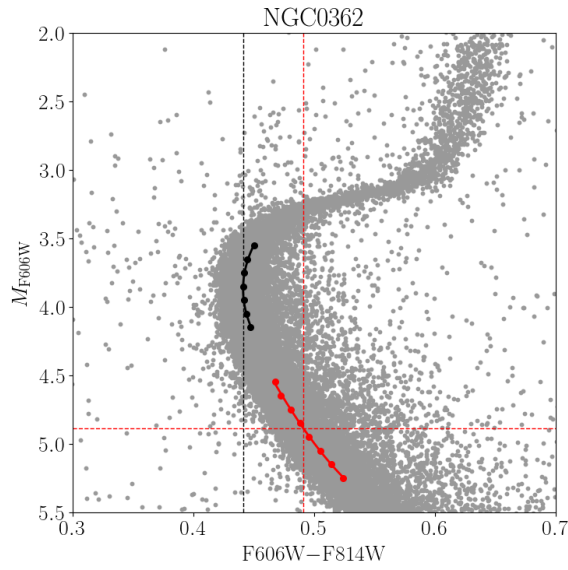


Figure 4.11: Colour-magnitude diagram zoomed near the turn off for NGC 0362. The observations are shown with grey points. The turn-off fiducial sequence is shown in black, with the vertical dashed line indicating the turn-off colour. The upper main-sequence fiducial sequence is displayed in red, with the vertical and horizontal dashed lines defining the colour (redder by 0.05 than the TO colour) and magnitude of the upper MS point, respectively.

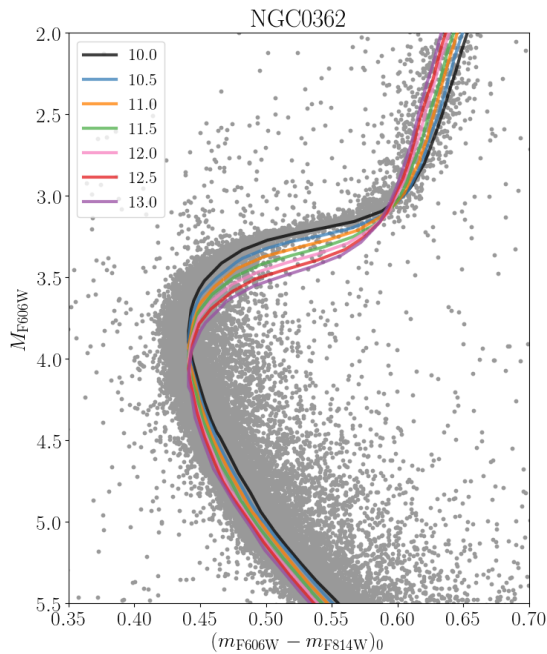


Figure 4.12: Colour-magnitude diagram zoomed near the turn off for NGC 0362. The observations are shown with grey points. The coloured lines correspond to different isochrones, that have been shifted to match the observed turn-off colour.

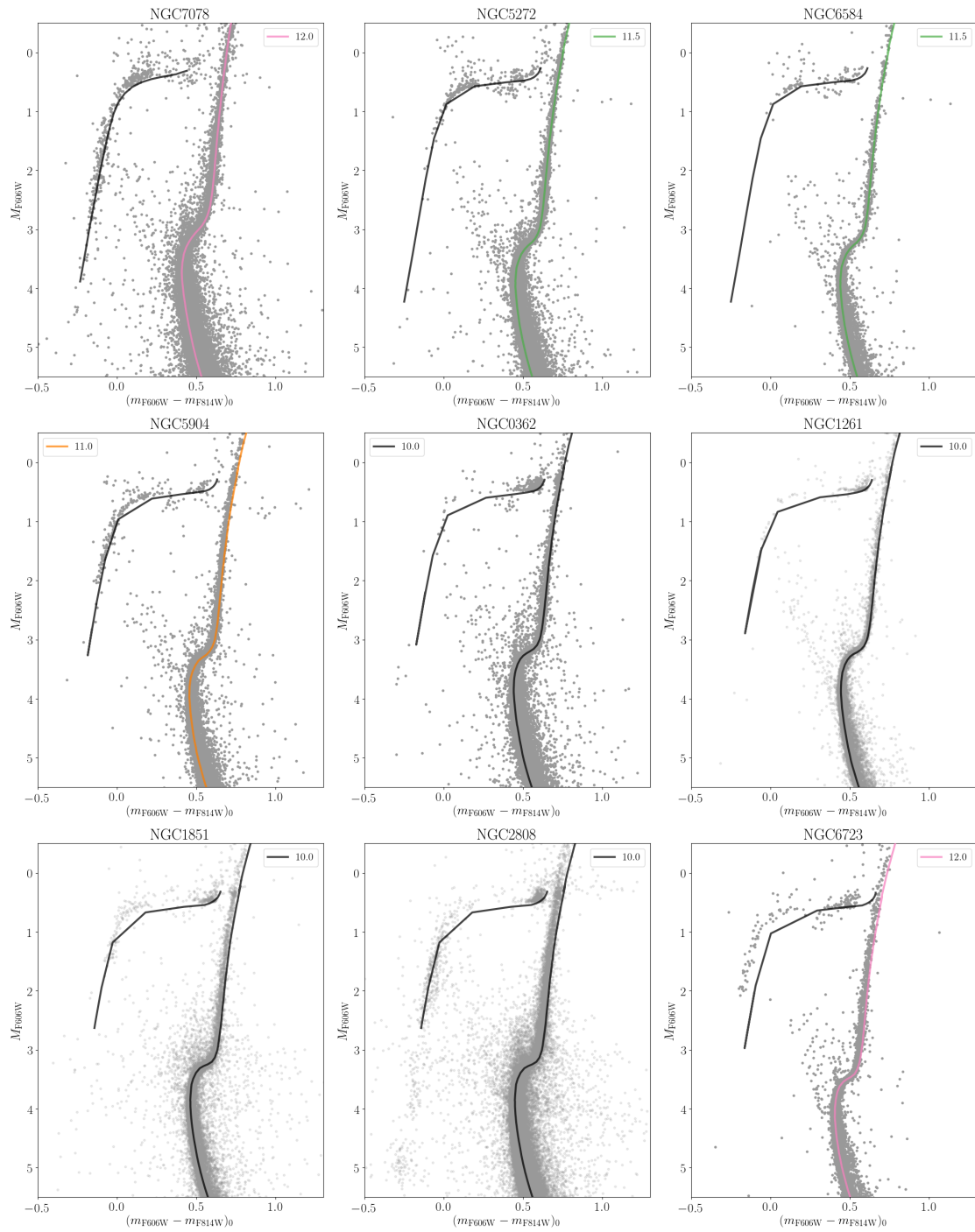


Figure 4.13: Colour-magnitude diagram for Galactic globular clusters. The observations are shown with grey points. The coloured lines correspond to the final isochrone that best fits the observed CMD, from the upper main-sequence to the horizontal branch. (1/3)

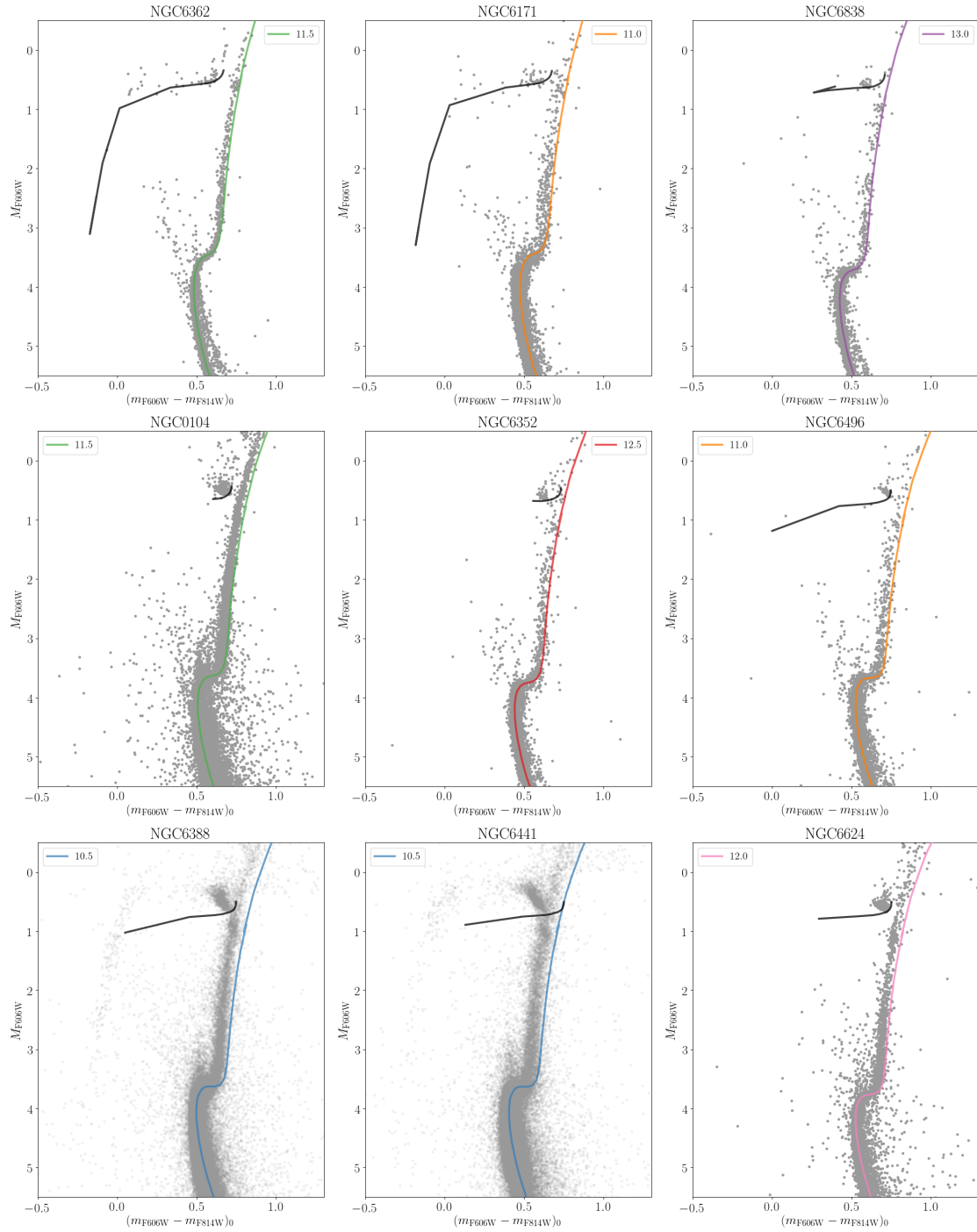


Figure 4.14: Same as Fig. 4.13. (2/3)

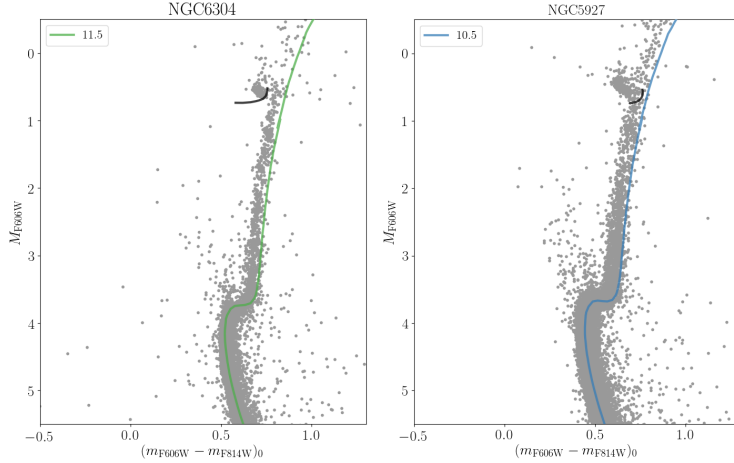


Figure 4.15: Same as Fig. 4.13. (3/3)

4.3.4 Preliminary Results

In Fig. 4.16, we show a preliminary comparison between the observed and expected positions of the red-giant branch bump in Galactic globular clusters. The observed location of the bump is extracted as outlined in Sec. 4.3.3, while the theoretical one is approximately estimated from the best-fitting isochrones using PARSEC tracks. Both observed and predicted RGBb magnitudes are converted from the F606W to the V -band photometric system, to allow for a comparison with the literature (Nataf et al., 2013). This is done by estimating the bolometric corrections in these two passbands, at the $\log g$, $[\text{Fe}/\text{H}]$, and T_{eff} associated with the bump brightness for each cluster, using Casagrande et al. (2014)’s code.

Although PARSEC tracks use a variable overshooting efficiency at the base of the convective envelope, stars at the magnitude of the bump have a mass below $M_{\text{O}1}$ in most (if not all) globular clusters considered here, based on the isochrones. Thus, it is fair to assume that the predictions shown in Fig. 4.16 correspond to an extra-mixing efficiency of $\Lambda_e = 0.05 H_P$. Based on this, we see that the discrepancy between observations and predictions becomes larger as we go towards lower metallicities, suggesting a higher overshooting efficiency for more metal-poor clusters. This preliminary finding, showing an apparent trend of the extra-mixing

efficiency with metallicity, is in line with results from [Khan et al. \(2018\)](#), see also Sec. 4.2). As discussed in Sec. 4.3.5, further work is required in order to strengthen our analysis and quantify this trend, but this is already very promising in our quest for improving the physical background behind convective boundary mixing (see Sec. 4.4).

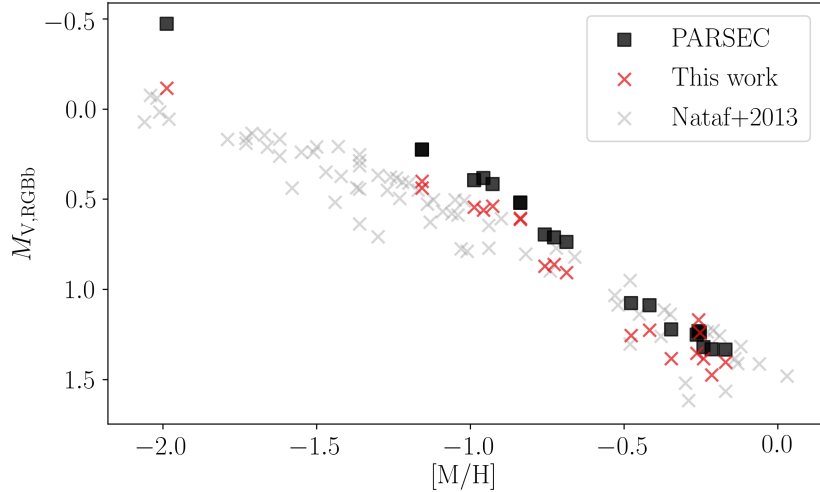


Figure 4.16: Absolute magnitude of the RGBb in the V -band, in our dataset of Galactic globular clusters (red), and best-fit isochrones using PARSEC tracks (black), as a function of metallicity. Data from [Nataf et al. \(2013\)](#) are also shown in grey for comparison.

4.3.5 Future plans

Isochrone-Fitting in Other Photometric Bands

At the current stage of this work, we are able to apply isochrone-fitting to all Galactic globular clusters in the $(F606W - F814W) - F606W$ plane. It should be straightforward to apply the same method to the other passbands, i.e. $(F438 - F606W) - F438W$, $(F336W - F438W) - F336W$, and $(F275W - F336W) - F275W$.

Isochrone-Fitting of Magellanic Clouds Clusters

For these younger clusters, series of isochrones are computed for ages between 0.5 and 3 Gyr. Besides, defining a zero-age horizontal branch can be done for Galactic globular clusters which are old and metal-poor, but Magellanic Clouds clusters are

much younger and more metal-rich (although still metal-poor with respect to the Sun) and do not display a horizontal branch — instead, they may even have a dual red clump. For this reason, we will have to figure out a different way to determine their distance modulus.

Adding different model grids to TRILEGAL

As of now, we have only used the default PARSEC evolutionary tracks that were already available in TRILEGAL. The idea is to include additional grids of models from MESA, some of which have already been computed. By using our own grids, we will be able to more flexible in the followings inputs:

- adjusting the envelope overshooting efficiency, using the diffusive mixing prescription (as in [Khan et al., 2018](#));
- including other types of mixing parameterisations, e.g. entrainment law (see Sec. 4.4 for more details);
- compute α -enhanced tracks, using Aaron Dotter’s code² that generates a file with the list of isotopes and their corresponding mass fraction, from the initial $[\text{Fe}/\text{H}]$ and $[\alpha/\text{Fe}]$, as well as an optional $\Delta Y/\Delta Z$.

These grids will have to be converted in the format that is required by TRILEGAL. In general terms, these formatted files will contain information about the ‘critical points’ for each evolutionary track, namely specific phases during the evolution such as the beginning of the MS, the turn off, the base of the RGB, the RGB bump, the RGB tip, the ZAHB, the AGB bump, and the AGB thermal pulse. These files are assembled in such a way that they facilitate the grid interpolation within TRILEGAL.

²https://github.com/aarondotter/initial_xa_calculator

Moving to detailed synthetic populations

We are able to find the best-fitting isochrone for each cluster, following the method described by [VandenBerg et al. \(2013\)](#). A step forward would be to use the suggested distance modulus and age, and combine them with metallicity, reddening, and cluster mass to continue towards more refined synthetic populations. Thanks to the isochrone-fitting method, we have removed the simulation’s dependence on two parameters, and therefore fitting a more detailed population should now be within reach.

Refining the statistical method to determine the RGB bump location

As discussed in Sec. 4.3.3, the method we used in [Khan et al. \(2018\)](#) cannot directly be used on the clusters analysed in this study. A few adjustments are necessary on the different probability functions at work, so that they become more suited to the parameter space covered by clusters.

Once these future steps are carried out, we will be able to draw further conclusions regarding the type and efficiency of convective boundary mixing that is suggested by clusters in the Milky Way and in the Magellanic Clouds, and whether they continue to support the trend with metallicity, as suggested by [Khan et al. \(2018\)](#).

4.4 Possible Interpretations for the Overshooting Trend with Metallicity

Results from [Khan et al. \(2018\)](#) and former studies based on globular clusters (including our preliminary findings) suggest a possible dependence of the extra-mixing efficiency with metallicity. This has been found by testing different ‘fixed’ values for the overshooting efficiency, either using the standard instantaneous or diffusive mixing parameterisations. However, it would be extremely interesting to see if a more

advanced mixing parameterisation, that depends on physical properties of the stellar interior structure, would be able to reproduce this trend with metallicity. A way to move forward in this direction is to link all the observational evidence gathered with expectations from hydrodynamical simulations, that provide a more detailed picture of fluid dynamics in stars. Hence, in this section, we discuss possible approaches to explain this trend with metallicity, based on novel mixing prescriptions inspired by 2D and 3D simulations.

4.4.1 Entrainment Law

An interesting mixing parameterisation to look at is the entrainment law, proposed by [Meakin & Arnett \(2007\)](#), which has the following form:

$$E = \frac{v_e}{v_c} = A \text{Ri}_B^{-n}, \quad (4.3)$$

where v_e is the entrainment velocity (the time rate of change of the boundary position through turbulent entrainment), v_c is the velocity representing the large-scale fluid elements, Ri_B is the bulk Richardson number, and A and n are constants.

Based on this, a first potential interpretation of the reduced mixing with increasing metallicity would be the increasing stiffness / more rapidly increasing Brunt-Väisälä frequency N below the convection zone. Fig. 4.17 shows that the increase in N^2 displays a steeper slope in the case of the most metal-rich model, hence a greater stiffness that is susceptible to reduce the envelope overshooting efficiency.

To go even further in this approach, it would be interesting to draw the link with 3D hydrodynamical simulations. For instance, [Cristini et al. \(2016\)](#) presented initial results of a study on convective boundary mixing in massive stars. They quantified the stiffness of convective boundaries using the bulk Richardson number:

$$\text{Ri}_B = \frac{\Delta B \mathcal{L}}{v_c^2/2}, \quad (4.4)$$

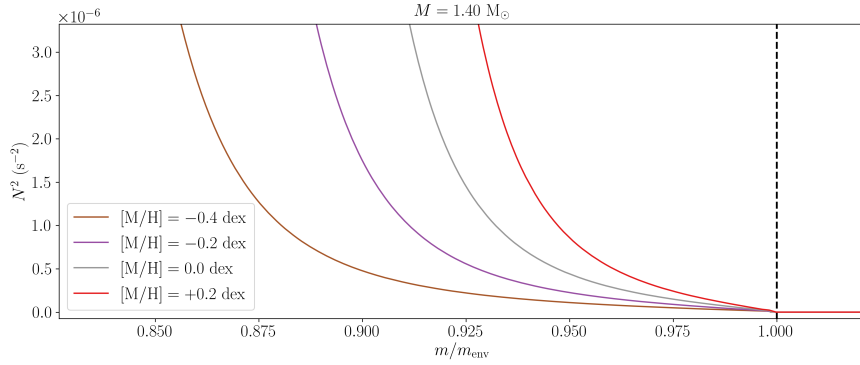


Figure 4.17: Squared Brunt-Väisälä frequency profiles for a $1.40 M_{\odot}$ model, with different metallicities: -0.4 (brown), -0.2 (purple), 0.0 (grey), and $+0.2$ dex (red). The x -axis has been normalised by the position of the base of the convective envelope, indicated by the black dashed line.

i.e. the ratio of the potential energy for restoration of the boundary to the kinetic energy of turbulent eddies. The ‘stabilisation potential’ ($\Delta B \mathcal{L}$) is similar to the work done by the boundary against convective motions. \mathcal{L} is a length scale associated with the turbulent motions; ΔB is the buoyancy jump over some distance Δr either side of the boundary position r_B :

$$\Delta B = \int_{r_B - \Delta r}^{r_B + \Delta r} N^2 dr , \quad (4.5)$$

where $\Delta B = \Delta B(N_T^2) + \Delta B(N_{\mu}^2)$ is the sum of its thermal and compositional components and N is the Brunt-Väisälä frequency; and v_c is the convective velocity. A high Ri_B (e.g. $\sim 10^4$) would correspond to a stiff boundary acting strongly against and thus suppressing convective boundary mixing, whereas a low Ri_B (e.g. ~ 10) would rather be a soft boundary more susceptible to convective boundary mixing. One of [Cristini et al. \(2016\)](#)’s main findings is that during the initial growth stage of the convective region, the buoyancy jump over the boundary is thermally dominated; as the burning stage progresses, the convective boundary recedes, a chemical composition gradient builds up, and the buoyancy jump becomes gradually dominated by a molecular weight gradient.

In this regard, we could try to relate and estimate these physical quantities in the context of the 1D stellar evolution models used in our analysis of the bump, and see if we make similar observations concerning the efficiency of mixing below the convective envelope of red-giant branch stars. One first step would be to compute the bulk Richardson number in our models, and see how it varies with metallicity along the evolution. A further step would be to define a different flavour of instantaneous or diffusive mixing, whereby the overshooting parameter would be a function of Ri_B (as the entrainment law itself might be challenging to implement). For instance, instead of having a fixed fraction of the pressure scale height (e.g. $0.2 H_P$), we could use an expression with the following form: $0.2 H_P \left(\frac{\text{Ri}_{B,\text{ref}}}{\text{Ri}_B} \right)^\alpha$, where $\text{Ri}_{B,\text{ref}}$ and α would be equivalent to A and n in Eq. 4.3.

4.4.2 Pratt et al. (2017) Diffusion Coefficient

Pratt et al. (2016, 2017) proposed a new form for the diffusion coefficient for stellar interiors in the large Péclet number (Pe) regime:

$$D(r) = D_0 \text{Pe}_B^{1/2} \left(1 - \exp \left(- \exp \left(- \frac{(r_B - r)/R - \mu}{\lambda} \right) \right) \right), \quad (4.6)$$

where the prefactor $D_0 \text{Pe}_B^{1/2}$ is representative of diffusion in the convection zone, r is the radial coordinate, R is the total stellar radius, r_B is the radial position of the convective boundary, and μ and λ are coefficients obtained from Pratt et al. (2017)'s numerical simulations. Using mixing length theory, the diffusion in the convection zone is defined as $D_c = 1/3 \alpha_{\text{MLT}} H_P v_c$, in which the convective velocity intervenes. The latter might show a dependence on stellar metallicity. At the moment, μ and λ are free parameters that have been derived in the context of a pre-main sequence model. Thus, if it turns out that similar hydrodynamical simulations can be developed for red giants, it would be intriguing to see how the implementation of this diffusion coefficient in 1D stellar evolution codes (see Baraffe et al., 2017) reproduces the possible dependence of overshooting on metallicity.

Chapter 5

Asteroseismology and *Gaia*

*The entirety of the text in Sec. 5.1 is taken verbatim from the published paper [Khan et al. \(2019\)](#), of which I was first author. In terms of individual work performed, I completed the majority of the work. Andrea Miglio performed the grid-modelling analysis, using the **PARAM** code. Anthony Brown shared an ipython notebook explaining how to simulate spatial covariances for *Gaia* DR2 sources. Ben M. Rendle provided me with the crossmatched tables for the K2 campaigns, containing both asteroseismic and photometric/spectroscopic data.*

If we are using asteroseismology to obtain stellar ages, a strong correlation between the inferences of mass and radius is present. Thus, by comparing asteroseismic and independent measurements, one can assess if significant biases are present in the seismically-determined masses and radii. The *Gaia* mission offers the opportunity to do this, with precise parallaxes being available for over 1.4 billion sources in the latest data release. Hence, this chapter presents a comparison of distances obtained with asteroseismology and those from the *Gaia* DR2 (Sec. 5.1) and *Gaia* eDR3 (Sec. 5.2) data releases.

There is also the possibility to combine seismic masses with luminosities derived using *Gaia* to have a full characterisation of the red-giant branch bump. However, as we will see later in this chapter, the accuracy and precision of *Gaia* DR2 parallaxes

were not sufficient for such an analysis — this might be considered again for *Gaia* EDR3 and later releases.

5.1 *Gaia* DR2 Parallax Zero-Point in the *Kepler*/*K2* fields

The importance of studying the *Gaia* DR2 parallax zero-point by external means was underlined by [Lindegren et al. \(2018\)](#), and initiated by several works making use of Cepheids, eclipsing binaries, and asteroseismology. Despite a very efficient elimination of basic-angle variations, a small fluctuation remains and shows up as a small offset in the *Gaia* DR2 parallaxes. By combining astrometric, asteroseismic, spectroscopic, and photometric constraints, we undertake a new analysis of the *Gaia* parallax offset for nearly 3000 red-giant branch (RGB) and 2200 red clump (RC) stars observed by *Kepler*, as well as about 500 and 700 red giants (both RGB and RC) selected by the *K2* Galactic Archaeology Program in campaigns 3 and 6. Engaging into a thorough comparison of the astrometric and asteroseismic parallaxes, we are able to highlight the influence of the asteroseismic method, and measure parallax offsets in the *Kepler* field that are compatible with independent estimates from literature and open clusters. Moreover, adding the *K2* fields to our investigation allows us to retrieve a clear illustration of the positional dependence of the zero-point, in general agreement with the information provided by quasars. Lastly, we initiate a two-step methodology to make progress in the simultaneous calibration of the asteroseismic scaling relations and of the *Gaia* DR2 parallax offset, which will greatly benefit from the gain in precision with the third Data Release of *Gaia*.

5.1.1 Introduction

Masses and radii of solar-like oscillating stars can be estimated from the global asteroseismic observables that characterise their oscillation spectra, namely the average large frequency separation ($\langle\Delta\nu\rangle$) and the frequency corresponding to the maximum

observed oscillation power (ν_{\max}). The large frequency spacing is predicted by theory to approximately scale as the square root of the mean density of the star (see, e.g., [Vandakurov, 1967](#); [Tassoul, 1980](#)):

$$\langle \Delta\nu \rangle \propto \sqrt{\langle \rho \rangle} \propto \sqrt{\frac{M}{R^3}}, \quad (5.1)$$

where M and R are the stellar mass and radius, respectively.

The frequency of maximum power follows to good approximation a proportional relation with the acoustic cut-off frequency, and can provide a direct measure of the surface gravity (g) when the effective temperature (T_{eff}) is known (see, e.g., [Brown et al., 1991](#); [Kjeldsen & Bedding, 1995](#); [Belkacem et al., 2011](#)):

$$\nu_{\max} \propto \frac{g}{\sqrt{T_{\text{eff}}}} \propto \frac{M}{R^2 \sqrt{T_{\text{eff}}}}. \quad (5.2)$$

Equations 5.1 and 5.2 imply that if $\langle \Delta\nu \rangle$ and ν_{\max} are available, together with an independent estimate of T_{eff} , a “direct” estimation of the stellar mass and radius is possible. This direct method is particularly attractive because it provides, in principle, estimates that are independent of stellar models.

Alternatively, one may also use $\langle \Delta\nu \rangle$ and ν_{\max} as inputs to a grid-based estimation of the stellar properties, matching the observations to stellar evolutionary tracks — either using the scalings at face value or stellar pulsation calculations to obtain $\langle \Delta\nu \rangle$ (e.g. [Stello et al., 2009](#); [Basu et al., 2010](#); [Gai et al., 2011](#); [Rodrigues et al., 2017](#)). Whether it be with the direct or the grid-based approach, a plethora of studies have compared asteroseismic measurements of radii (or distances) with independent ones, such as clusters ([Miglio et al., 2012b, 2016](#); [Stello et al., 2016](#); [Handberg et al., 2017](#)), interferometry ([Huber et al., 2012](#)), eclipsing binaries ([Gaulme et al., 2016](#); [Brogaard et al., 2016, 2018](#)), and astrometry ([Silva Aguirre et al., 2012](#); [De Ridder et al., 2016](#); [Davies et al., 2017](#); [Huber et al., 2017](#); [Sahlholdt et al., 2018](#); [Zinn et al., 2019](#)). All these works indicated that stellar radius estimates from asteroseismology

are accurate to within a few percent.

On the astrometric side, before the *Gaia* data, the asteroseismic distances — arising from the combination of seismic constraints with effective temperature and apparent photometric magnitudes — of stars in the solar neighbourhood had only been compared a posteriori with HIPPARCOS values, with limitations due to the HIPPARCOS uncertainties being large for most of the *Kepler* and CoRoT targets (Miglio et al., 2012b; Silva Aguirre et al., 2012; Lagarde et al., 2015). The announcement of the first *Gaia* Data Release opened the gates to the *Gaia* era (Gaia Collaboration et al., 2016b,a). Parallaxes and proper motions were available for the 2 million brightest sources in *Gaia* DR1, as part of the *Tycho-Gaia* Astrometric Solution (TGAS; Lindegren et al., 2016). As the TGAS parallaxes considerably improved the HIPPARCOS values, a new comparison between astrometric and asteroseismic parallaxes was appropriate. Some works took the path of the model-independent method, i.e. using asteroseismic distances based on the use of the raw scaling relations. Using assumptions about the luminosity of the red clump, Davies et al. (2017) found the TGAS sample to overestimate the distance, with a median parallax offset of -0.1 mas. For 2200 *Kepler* stars, from the main sequence to the red-giant branch, Huber et al. (2017) obtained a qualitative agreement, especially if they adopted a hotter effective temperature scale for dwarfs and subgiants. The latter suggestion was corroborated by Sahlholdt et al. (2018). In contrast, De Ridder et al. (2016) used seismic modelling methods to analyse two samples of stars observed by *Kepler*: 22 nearby dwarfs and subgiants showing an excellent overall correspondence; and 938 red giants for which the TGAS parallaxes were significantly smaller than the seismic ones. Given the different seismic approaches and the various outcomes, the situation as regards to the *Gaia* DR1 parallax offset, as probed by asteroseismology, was left unclear.

The second Data Release of *Gaia* was published on April 25th, 2018 (Gaia Collaboration et al., 2018), based on the data collected during the first 22 months of the

nominal mission lifetime (Gaia Collaboration et al., 2016a). *Gaia* DR2 represents a major advance with respect to the first intermediate *Gaia* Data Release, containing parallaxes and proper motions for over 1.3 billion sources. Unlike the TGAS, the *Gaia* DR2 astrometric solution does not incorporate any information from HIPPARCOS and *Tycho-2*. However, with less than two years of observations and preliminary calibrations, a few weaknesses in the quality of the astrometric data remain, and were identified by Arenou et al. (2018) and Lindegren et al. (2018). Among these caveats, the latter study underlined the importance of investigating the parallax zero-point by external means, and did so through the use of quasars which are a quasi-ideal means in this matter: negligibly small parallaxes, large number, and availability over most of the celestial sphere. A global zero-point of about $-30 \mu\text{as}$ was found by Lindegren et al. (2018), in the sense that *Gaia* parallaxes are too small, with variations — in the order of several tens of μas — depending on a given combination of magnitude, colour, and position. Quasars have their own specific properties, such as their faintness and blue colour, which should be kept in mind when interpreting these results. For this reason, a direct correction of individual parallaxes from the global parallax zero-point is discouraged (Arenou et al., 2018).

In this context, several works have confirmed the existence of a parallax offset by independent means. The study of 50 Cepheids by Riess et al. (2018) suggested a zero-point offset of $-46 \pm 13 \mu\text{as}$. Stassun & Torres (2018) presented evidence of a systematic offset of about $-82 \pm 33 \mu\text{as}$ with 89 eclipsing binaries. And, finally, Zinn et al. (2019) inferred a systematic error of -52.8 ± 2.4 (statistical) ± 1 (systematic) μas for 3500 first-ascent giants in the *Kepler* field, using asteroseismic and spectroscopic constraints from Pinsonneault et al. (2018) who used model-predicted corrections to the $\langle \Delta\nu \rangle$ scaling relation. Very little difference was found with 2500 red-clump stars: -50.2 ± 2.5 (statistical) ± 1 (systematic) μas , which is expected from the astrometric point of view since *Gaia*, unlike seismology, does not make any distinction between shell-hydrogen and core-helium burning stars.

These various outcomes demonstrate the need to independently solve the parallax zero-point within the framework of an analysis having its own specificities, i.e. magnitude, colour, and spatial distributions. In the case of asteroseismology, the findings of a comparison with *Gaia* DR2 cannot be dissociated from the seismic method employed. With this in mind, we engage into a thorough investigation of the *Gaia* DR2 parallax offset in the *Kepler* field, by taking an incremental approach — starting with the scaling relations taken at face value and gradually working towards a Bayesian estimation of stellar properties using a grid of models (Sect. 5.1.4). Also, looking at the broader picture and considering two fields of the repurposed *Kepler* mission, *K2*, allows us to investigate the positional dependence of the zero-point (Sect. 5.1.5). Lastly, *Gaia* DR2 offers scope for development in the calibration of the scaling relations, and we initiate a two-step methodology allowing us to constrain the *Gaia* DR2 offset at the same time (Sect. 5.1.6).

5.1.2 Observational Framework

Description of the datasets

One part of our sample consists of red-giant stars observed by *Kepler* and with APOGEE spectra available (APOKASC collaboration; [Abolfathi et al., 2018](#)). From the initial list of stars, we select those that are classified as RGBs and RCs (including secondary clump stars as well) using the method by [Elsworth et al. \(2017\)](#). We consider the global asteroseismic parameters $\langle \Delta\nu \rangle$ and ν_{\max} . We use the frequency of maximum oscillation power, ν_{\max} , from [Mosser et al. \(2011a\)](#). Two methods for providing relevant estimates of $\langle \Delta\nu \rangle$ are discussed in Sect. 5.1.2. We also make use of the spectroscopically measured effective temperature T_{eff} , surface gravity $\log g$ (calibrated against asteroseismic surface gravities), and of constraints on the photospheric chemical composition $[\text{Fe}/\text{H}]$ and $[\alpha/\text{Fe}]$ from SDSS DR14, as determined by the APOGEE Pipeline ([Abolfathi et al., 2018](#)). This leads us to 3159 RGB stars and 2361 RC stars in the *Kepler* field.

Our *Kepler* subsample is then complemented with red giants selected by the *K2* Galactic Archaeology Program (GAP; [Howell et al., 2014](#); [Stello et al., 2015, 2017](#)) in campaigns 3 (south Galactic cap) and 6 (north Galactic cap), that have SkyMapper photometric constraints ([Casagrande et al., 2019](#)). We make use of the asteroseismic analysis method from [Mosser et al. \(2011a\)](#) for the vast majority and from [Elsworth et al. \(2017\)](#) for a very small fraction of stars ($\sim 5\%$), and we refer the reader to [Rendle et al. \(2019b\)](#) for details about additional tests of the seismic results’ reliability. For T_{eff} and $[\text{Fe}/\text{H}]$, we use the photometric estimates originating from the SkyMapper survey ([Casagrande et al., 2019](#)), and $\log g$ comes from asteroseismically-derived estimates. This *K2* subsample falls into two parts: 505 and 723 red giants in C3 and C6, respectively.

For the full sample, stellar masses and extinctions are inferred using the Bayesian tool PARAM ([Rodrigues et al., 2014, 2017](#)). Asteroseismic constraints $\langle\Delta\nu\rangle$ and ν_{max} are included in the modelling procedure in a self-consistent manner, whereby $\langle\Delta\nu\rangle$ is calculated from a linear fitting of the individual radial-mode frequencies of the models in the grid. PARAM also requires photometry, and uses its own set of bolometric corrections (described at length in [Girardi et al., 2002](#)), to estimate distances and extinctions. In addition, we calculate extinctions via the [Green et al. \(2015\)](#) dust map and the RJCE method ([Majewski et al., 2011](#)) for comparison purposes. The bolometric corrections are derived using the code written by [Casagrande et al. \(2014\)](#); [Casagrande & Vandenberg \(2018a,b\)](#), taking T_{eff} , $\log g$, and $[\text{Fe}/\text{H}]$ as input parameters. The second Data Release of *Gaia* ([Gaia Collaboration et al., 2016a, 2018](#)) then provides us with astrometric and photometric constraints: parallaxes (using the external parallax uncertainty as described by Lindegren et al. in their overview of *Gaia* DR2 astrometry¹, and made available by the *Gaia* team at the GEPI, Observatoire de Paris²), G -band magnitudes — which are corrected following [Casagrande & Vandenberg \(2018a\)](#), i.e. $G_{\text{corr}} = 0.0505 + 0.9966 G$ — and $G_{\text{BP}} - G_{\text{RP}}$

¹<https://www.cosmos.esa.int/web/gaia/dr2-known-issues>

²<https://gaia.obspm.fr/tap-server/tap>

colour indices. The 2MASS (Skrutskie et al., 2006) *K*-band photometry is used as well.

Consistency in the definition of $\langle \Delta\nu \rangle$

For the *Kepler* field (Sect. 5.1.4), we explore different seismic methods, which have to be matched with a consistent definition of $\langle \Delta\nu \rangle$. To use $\langle \Delta\nu \rangle$ in the scaling relations, one would want to adopt a measure which is as close as possible to the asymptotic limit (on which the scaling is based). This implies, e.g., correcting for acoustic glitches (regions of sharp sound-speed variation in the stellar interior related to a rapid change in the chemical composition, the ionisation of major chemical elements, or the transition from radiative to convective energy transport; see, e.g., Miglio et al., 2010; Vradar et al., 2015). In that case, the $\langle \Delta\nu \rangle$ measured by Mosser et al. (2011a) is appropriate since their method mitigates the perturbation on $\langle \Delta\nu \rangle$ due to glitches. On the other hand, one could abandon scalings and use $\langle \Delta\nu \rangle$ from models which can, e.g., be based on individual frequencies as in PARAM, which also takes into account departures from homology (regarding the assumption of scaling with density, i.e. Eq. (5.1)). Then, it is more adequate to combine PARAM with $\langle \Delta\nu \rangle$ estimates from individual radial-mode frequencies. While the latter are currently available only for a small subset (697 RGB and 783 RC stars), following the approach presented in Davies et al. (2016), we notice a qualitative agreement with $\langle \Delta\nu \rangle$ from Yu et al. (2018) which are also derived from the frequencies. On the contrary, the $\langle \Delta\nu \rangle$ as determined by Mosser et al. (2011a) has a different definition, closer to the analytical asymptotic relation, and its value for RGB stars is systematically larger by $\sim 1\%$ compared to the one from individual mode frequencies, as shown on Fig. 5.1. Meanwhile, there is no specific trend in the difference between the two $\langle \Delta\nu \rangle$ estimates for RC stars.

Therefore, in Sect. 5.1.4, we use raw scaling relations in combination with $\langle \Delta\nu \rangle$ from Mosser et al. (2011a); while, in Sects. 5.1.4 and 5.1.4 where theoretically-motivated corrections to the $\langle \Delta\nu \rangle$ scaling are used, we adopt $\langle \Delta\nu \rangle$ from Yu et al.

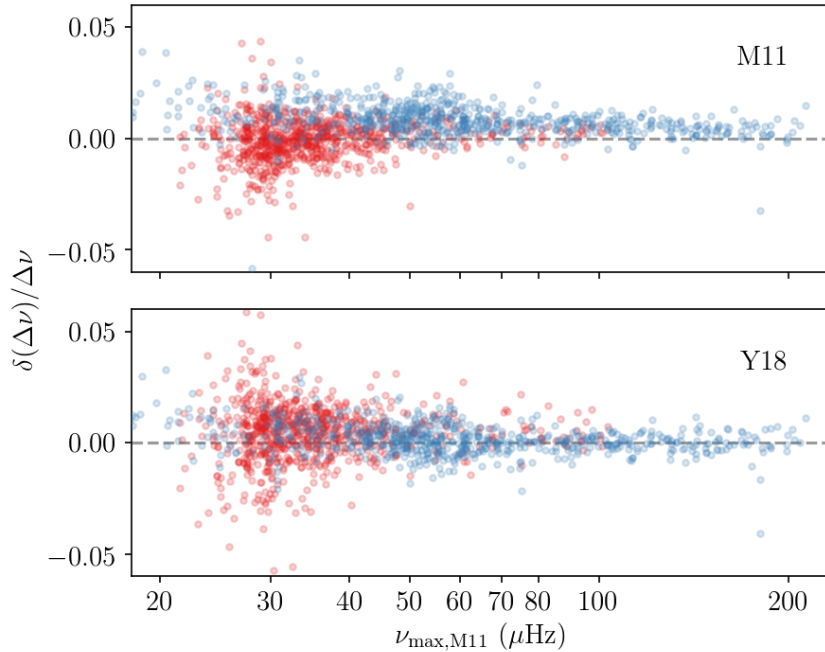


Figure 5.1: Relative difference in $\langle\Delta\nu\rangle$, $\delta(\Delta\nu)/\Delta\nu = (\Delta\nu_{\text{other}} - \Delta\nu_{\text{D16}})/\Delta\nu_{\text{D16}}$, between individual frequencies following [Davies et al. \(2016\)](#) (D16) and another method, as a function of ν_{\max} as estimated by [Mosser et al. \(2011a\)](#). The comparison is done with [Mosser et al. \(2011a\)](#) (M11; top) and [Yu et al. \(2018\)](#) (Y18; bottom). RGB and RC stars are in blue and red, respectively. Here, $\Delta\nu$ is used, instead of $\langle\Delta\nu\rangle$, to simplify the notation.

(2018) instead.

5.1.3 Detailed Objectives

In order to simplify the statistical analysis of our results, we formulate the problem in the astrometric data space, i.e. parallax space. Significant biases can arise from the inversion of parallaxes into distances and from sample truncation, such as the removal of negative parallaxes and / or parallaxes with a relative error above a given threshold ([Luri et al., 2018](#)). Thus, in the current investigation, we avoid doing any of these. On the other hand, it is quite reasonable to invert asteroseismic distances to obtain parallaxes because their uncertainties are typically lower than a few percent (see, e.g., [Rodrigues et al., 2014](#)).

If one wishes to express the parallax as a function of the apparent and intrinsic

luminosity of a star, this can be done using the Stefan-Boltzmann law, as follows:

$$\varpi = c_\lambda \left(\frac{R_{\text{bb}}}{R_\odot} \right)^{-1} \left(\frac{T_{\text{eff}}}{T_{\text{eff},\odot}} \right)^{-2}, \quad (5.3)$$

where R_{bb} is the radius of the black body of effective temperature T_{eff} , i.e. the photospheric radius, and $c_\lambda = 10^{-0.2(m_\lambda + BC_\lambda + 5 - A_\lambda - M_{\text{bol},\odot})}$. m_λ , BC_λ , and A_λ are the magnitude, bolometric correction, and extinction in a given band λ , and we adopt $M_{\text{bol},\odot} = 4.75$ for the Sun's bolometric magnitude. Thereafter, we will resort to the 2MASS K -band magnitude properties (m_K , BC_K , and A_K), whenever we need to estimate the coefficient c_λ .

Asteroseismic parallax

Engaging in such a parallax comparison requires a way to express the seismic information in terms of parallax, to be compared to the *Gaia* astrometric measurements. Seismic parallaxes are also based on the Stefan-Boltzmann law. Going back to the foundations of ensemble asteroseismology, seismic scaling relations provide relevant estimates of the stellar masses and radii. From Eqs. (5.1) and (5.2), their expressions are as follows:

$$\left(\frac{M}{M_\odot} \right) \approx \left(\frac{\nu_{\text{max}}}{\nu_{\text{max},\odot}} \right)^3 \left(\frac{\langle \Delta\nu \rangle}{\langle \Delta\nu \rangle_\odot} \right)^{-4} \left(\frac{T_{\text{eff}}}{T_{\text{eff},\odot}} \right)^{3/2}, \quad (5.4)$$

$$\left(\frac{R}{R_\odot} \right) \approx \left(\frac{\nu_{\text{max}}}{\nu_{\text{max},\odot}} \right) \left(\frac{\langle \Delta\nu \rangle}{\langle \Delta\nu \rangle_\odot} \right)^{-2} \left(\frac{T_{\text{eff}}}{T_{\text{eff},\odot}} \right)^{1/2}, \quad (5.5)$$

involving both global asteroseismic observables $\langle \Delta\nu \rangle$ and ν_{max} , and T_{eff} . The solar references are taken as $\langle \Delta\nu \rangle_\odot = 135 \mu\text{Hz}$, $\nu_{\text{max},\odot} = 3090 \mu\text{Hz}$, and $T_{\text{eff},\odot} = 5777 \text{ K}$. It is assumed here that the seismic radius, R , and the black-body radius, R_{bb} , are the same. Finally, using Eqs. (5.3) and (5.5), the seismic parallax ensuing from the

scaling relations can be written as

$$\varpi_{\text{scaling}} = c_{\lambda} \left(\frac{\nu_{\text{max}}}{\nu_{\text{max},\odot}} \right)^{-1} \left(\frac{\langle \Delta\nu \rangle}{\langle \Delta\nu \rangle_{\odot}} \right)^2 \left(\frac{T_{\text{eff}}}{T_{\text{eff},\odot}} \right)^{-5/2}. \quad (5.6)$$

The seismic scaling relations have been widely used, even though it is known that they are not precisely calibrated yet. Testing their validity has become a very active topic in asteroseismology, and has been addressed in several ways. It may take the form of a comparison between asteroseismic radii and independent measurements of stellar radii (e.g. [Huber et al., 2012](#); [Gaulme et al., 2016](#); [Miglio et al., 2016](#); [Huber et al., 2017](#)). An alternative approach consists in validating the relation between the average large frequency separation and the stellar mean density from model calculations ([Ulrich, 1986](#)). The asymptotic approximation for acoustic oscillation modes tells us that $\langle \Delta\nu \rangle$ is directly related to the sound travel-time in the stellar interior, and therefore depends on the stellar structure ([Tassoul, 1980](#)). As mentioned in Sect. 5.1.1, Eq. (5.1) is approximate and assumes that stars, in general, are homologous to the Sun and that the measured $\langle \Delta\nu \rangle$ corresponds to $\langle \Delta\nu \rangle$ in the asymptotic limit; in practice, that is not the case (for further details see, e.g., [Belkacem et al., 2013](#)). The sound speed in their interior (hence the total acoustic travel-time) does not simply scale with mass and radius only. In particular, whether a red-giant star is burning hydrogen in a shell or helium in a core, its internal temperature (hence sound speed) distribution will be different. This led several authors to quantify any deviation from the $\langle \Delta\nu \rangle$ scaling relation these differences could cause (e.g. [White et al., 2011](#); [Miglio, 2012](#); [Belkacem et al., 2012](#); [Guggenberger et al., 2016](#); [Sharma et al., 2016](#); [Rodrigues et al., 2017](#)). Stellar evolution calculations show that the deviation varies by a few percent with mass, chemical composition, and evolutionary state. That is why the seismic parallax can also be estimated from the large separation determined with grid-based modelling, i.e. statistical methods taking into account stellar theory predictions (e.g. allowed combinations of mass, radius,

Ev. state	ϖ_{Gaia} (μas)	G	ν_{max} (μHz)	$G_{\text{BP}} - G_{\text{RP}}$	M_{PARAM} (M_{\odot})	[Fe/H]
RGB	708	12.2	72.7	1.35	1.14	-0.036
RC	625	11.8	40.0	1.29	1.34	-0.0045

Table 5.1: Values of \bar{X} (mean value of the stellar parameter X) for RGB (top) and RC stars (bottom).

effective temperature, and metallicity) as well as other kinds of prior information (e.g. duration of evolutionary phases, star formation rate, initial mass function). In particular, the Bayesian tool PARAM uses $\langle\Delta\nu\rangle$, ν_{max} , T_{eff} , $\log g$, [Fe/H], $[\alpha/\text{Fe}]$ (when available), and photometric measurements to derive probability density functions for fundamental stellar parameters, including distances (Rodrigues et al., 2014, 2017).

The asteroseismic results thus depend on the method employed. This aspect is explored in more detail in Sect. 5.1.4, where three distinct seismic methods are tested (with the appropriate $\langle\Delta\nu\rangle$, as discussed in Sect. 5.1.2): the raw scaling relations, a relative correction to the $\langle\Delta\nu\rangle$ scaling between RGB and RC stars, and a model-grid-based Bayesian approach defining $\langle\Delta\nu\rangle$ from individual frequencies. Furthermore, in Sect. 5.1.6, we combine asteroseismic and astrometric data to simultaneously calibrate the scaling relations and the *Gaia* zero-point.

Method

Our study is based on the analysis of the absolute, rather than relative, difference between *Gaia* and seismic parallaxes: $\Delta\varpi = \varpi_{\text{Gaia}} - \varpi_{\text{seismo}}$. This is for two reasons: first, the global zero-point offset in *Gaia* parallaxes is absolute (Lindegren et al., 2018); second, working in terms of relative difference can amplify trends, e.g. due to offsets having a greater impact on small parallaxes.

We explore the trends of the measured offset ($\Delta\varpi$) for a set of stellar parameters: the *Gaia* parallax ϖ_{Gaia} , the G -band magnitude, the frequency of maximum oscillation ν_{max} , the $G_{\text{BP}} - G_{\text{RP}}$ colour index, the mass inferred from PARAM (M_{PARAM}), and the metallicity [Fe/H]. Each of these relations is described with a linear fit

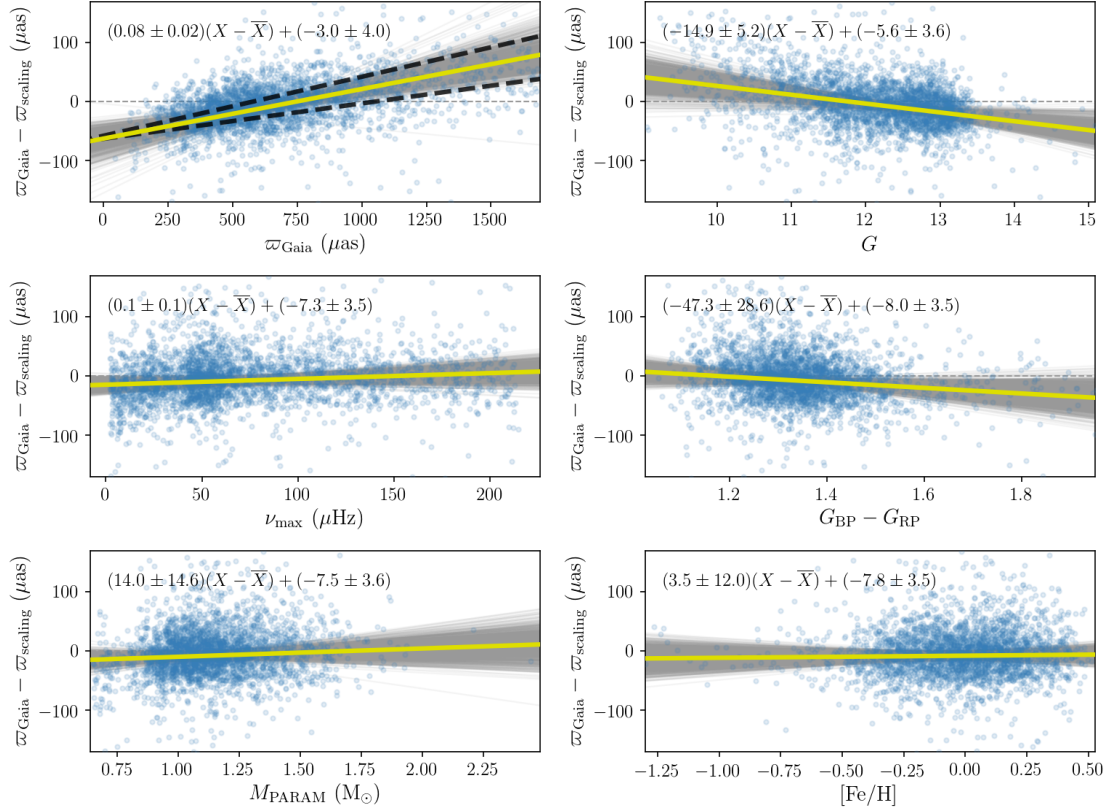


Figure 5.2: Parallax difference $\varpi_{\text{Gaia}} - \varpi_{\text{seismo}}$ for RGB stars, with the asteroseismic parallax derived from the raw scaling relations, as a function of ϖ_{Gaia} , G , ν_{max} , $G_{\text{BP}} - G_{\text{RP}}$, M_{PARAM} , and $[\text{Fe}/\text{H}]$. The distribution of the N realisations of the RANSAC algorithm is indicated by the grey-shaded region and the yellow line displays the average linear fit, for which the relation is given at the top of each subplot. The values of \bar{X} for RGB stars are given in Table 5.1. The summary statistics are: $(\overline{\Delta\varpi})_{\text{m}} = -6.2 \pm 1.3 \mu\text{as}$, $(\overline{\Delta\varpi})_{\text{w}} = -7.9 \pm 0.8 \mu\text{as}$, and $z = 0.89$. The black dashed lines correspond to the average linear fits when a ± 100 K shift in T_{eff} is applied. An increase in ϖ_{Gaia} corresponds to a decrease in distance, while an increase in G is equivalent to an increase in distance (at fixed absolute magnitude): this means that the two top panels possibly show the same trend but in the opposite direction.

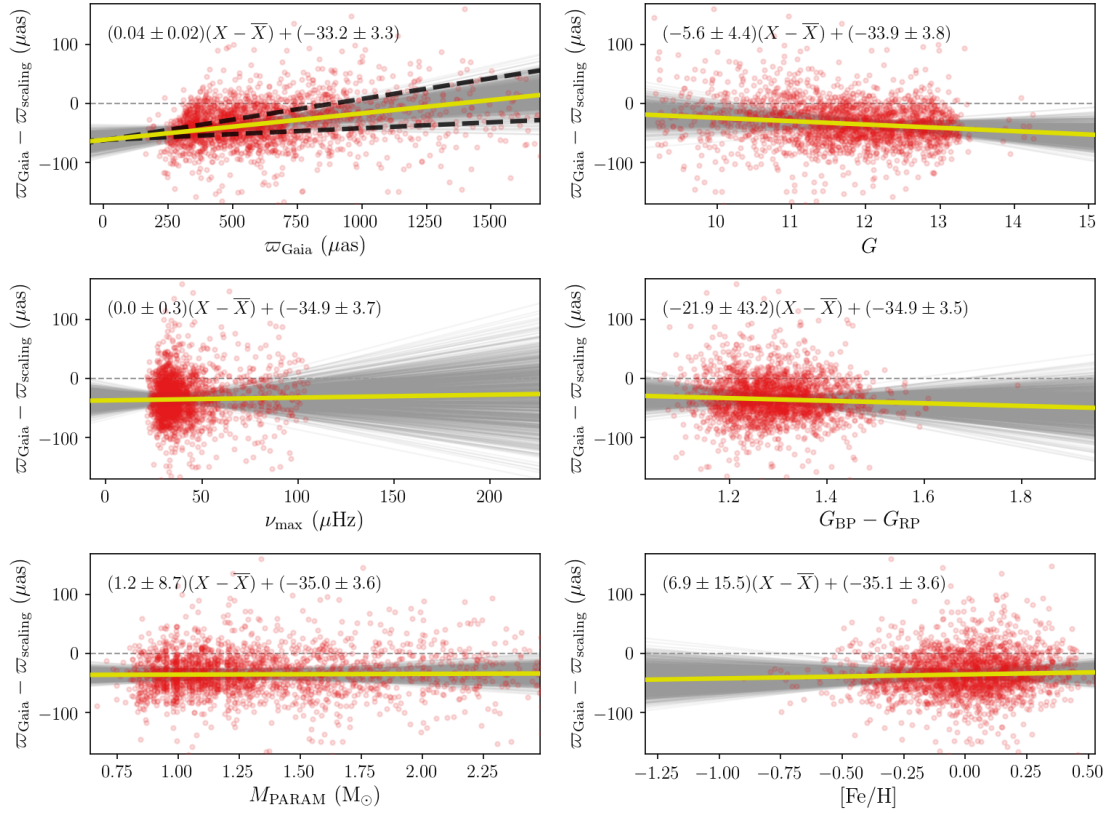


Figure 5.3: Same as Fig. 5.2 for RC stars. The values of \bar{X} for RC stars are given in Table 5.1. The summary statistics are: $(\Delta\varpi)_{\text{m}} = -34.6 \pm 1.4 \mu\text{as}$, $(\Delta\varpi)_{\text{w}} = -35.6 \pm 0.9 \mu\text{as}$, and $z = 0.84$.

obtained through a RANSAC algorithm (Fischler & Bolles, 1981). The fitting parameters' uncertainties are estimated by making $N = 1000$ realisations of the set of parameters analysed with RANSAC, where a normally distributed noise is added using the observed uncertainties on $\Delta\varpi$ and the different stellar parameters. Because the fitting parameters are strongly dependent on the range of values covered by the independent variable X (the stellar parameter considered), the fits are expressed in the following form: $\Delta\varpi(X) = \alpha_X(X - \bar{X}) + \beta_X$. α_X is the slope, β_X is the intercept from which $\alpha_X\bar{X}$ was subtracted, and \bar{X} is the mean value of the stellar parameter X (Table 5.1).

As part of the analysis, some summary statistics are also given:

- the median parallax difference $(\overline{\Delta\varpi})_m$ and the associated uncertainty $\sigma_{(\overline{\Delta\varpi})_m}$;
- the weighted average parallax difference

$$(\overline{\Delta\varpi})_w = \frac{\sum_{i=1}^N \Delta\varpi_i / \sigma_{\Delta\varpi_i}^2}{\sum_{i=1}^N 1 / \sigma_{\Delta\varpi_i}^2}, \quad (5.7)$$

for which the uncertainty quoted is the weighted standard deviation, which gives a measure of the spread and also takes into account the individual (formal) uncertainties in $\Delta\varpi$, i.e.

$$\sigma_{(\overline{\Delta\varpi})_w} = \sqrt{\frac{\sum_{i=1}^N (\Delta\varpi_i - (\overline{\Delta\varpi})_w)^2 / \sigma_{\Delta\varpi_i}^2}{(N - 1) \sum_{i=1}^N 1 / \sigma_{\Delta\varpi_i}^2}}; \quad (5.8)$$

- and the ratio $z = \sigma_{(\overline{\Delta\varpi})_w} / \overline{\sigma_{(\overline{\Delta\varpi})_w}}$, where $\overline{\sigma_{(\overline{\Delta\varpi})_w}} = 1 / \sqrt{\sum_{i=1}^N 1 / \sigma_{\Delta\varpi_i}^2}$ is the uncertainty of the weighted mean estimated from the formal uncertainties on $\Delta\varpi$, which allows one to assess how well the formal fitting uncertainties reflect the scatter in the data; if the $\Delta\varpi$ scatter is dominated by random errors and the formal uncertainties reflect the true observational uncertainties, then z is close to unity.

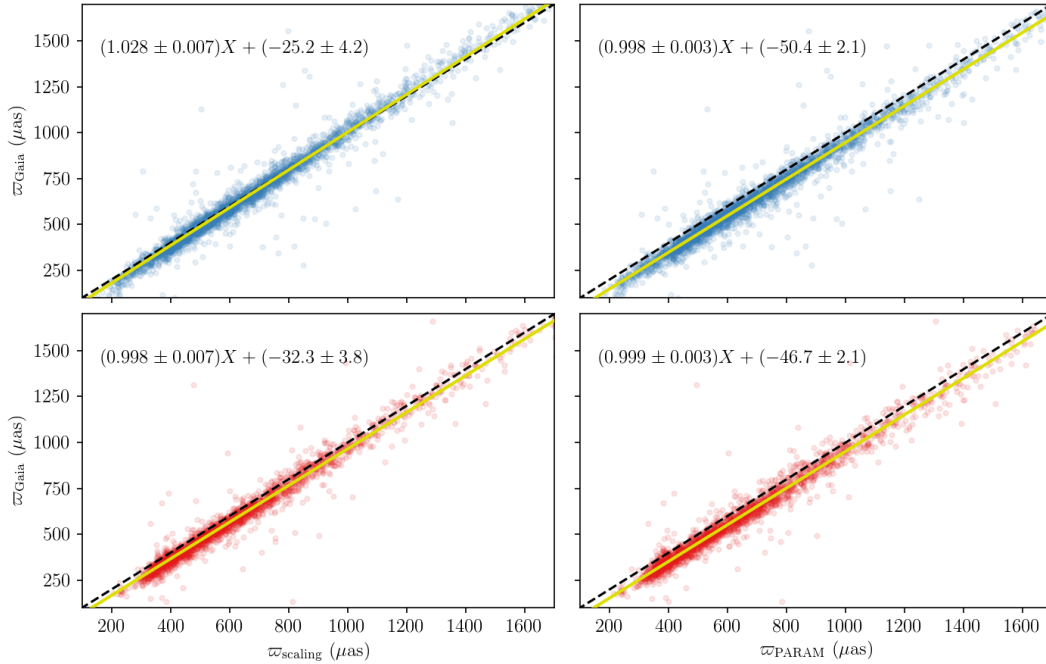


Figure 5.4: ϖ_{Gaia} as a function of ϖ_{scaling} (left) and ϖ_{PARAM} (right), for RGB (top) and RC (bottom) stars. The yellow line displays the linear fit, averaged over N realisations, for which the relation is given at the top of each subplot. The black dashed line indicates the 1:1 relation.

In the following, unless stated otherwise, the weighted average parallax difference estimator will be used for the offsets quoted in the text.

5.1.4 Analysis of the *Kepler* Field

In this section, we focus on the comparison between *Gaia* DR2 and asteroseismology for red giants in the *Kepler* field. We take advantage of [Elsworth et al. \(2017\)](#)'s classification method, based on the structure of the dipole-mode oscillations of mixed character, to distinguish between shell-hydrogen burning stars, on the red-giant branch, and core-helium burning stars, in the red clump (including secondary clump stars as well). From the asteroseismic perspective, three different approaches are employed in order to emphasise the influence of the seismic method on the measured parallax zero-point.

Raw scaling relations

We start with the raw scaling relations, to which no correction has been applied: the seismic parallax is directly estimated from Eq. (5.6), using $\langle \Delta\nu \rangle$ from Mosser et al. (2011a). The comparison with *Gaia* parallaxes is shown on Figs. 5.2 and 5.3 for RGB and RC stars, respectively. At first sight, we observe a strong dependence of the RGB parallax difference with ϖ_{Gaia} : as the latter increases, $\Delta\varpi$ significantly increases as well (Fig. 5.2, top left panel). Such a trend also appears for RC stars, but to a much lesser extent. In fact, the parallax zero-point is expected to show variations depending on position, magnitude and colour (Lindegren et al., 2018) but not on parallax, unless we consider stars with the same intrinsic luminosity (e.g. RC stars; see Fig. 5.3). In such a case, the dependence on apparent magnitude would manifest itself as a dependence on parallax. In addition, for core-helium burning stars, one can see that there is a cut-off at low astrometric parallaxes ($\varpi_{\text{Gaia}} < 350 \mu\text{as}$; Fig. 5.3, top left panel). This is most likely related to the selection in magnitude in *Kepler* (see, e.g., Farmer et al., 2013), which translates into a limit on distance. *Gaia* parallaxes, having larger uncertainties compared to their asteroseismic counterparts, can lead to distances greater than this limit and, when represented on the x -axis, create a horizontal structure (adding to the vertical structure caused by the scatter of the parallax difference) as observed. On the contrary, if we had the seismic parallax on the x -axis instead, such a structure would disappear and the slope would become flatter. Still, we note that these trends might either come from the seismic parallax or from the correlation between the parallax difference and the *Gaia* parallax. Having a deeper look at the summary statistics, there seems to be a considerable difference in the measured offset: that of RGB stars reaches up to $-8 \mu\text{as}$, compared to RC stars displaying an average value of $-36 \mu\text{as}$. On their own, these results could be interpreted as a minimal difference between astrometric and asteroseismic measurements for stars along the RGB, but there remains the issue of the apparent trends of $\Delta\varpi$ with parallax.

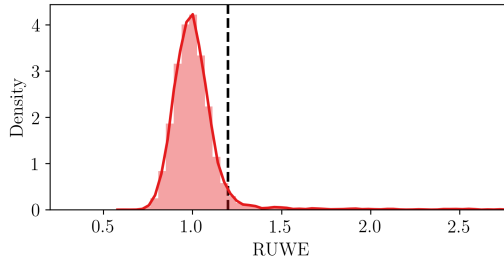


Figure 5.5: Renormalised Unit Weight Error distribution for *Kepler* RGB and RC stars. The vertical dashed line indicates the threshold adopted: $\text{RUWE} \leq 1.2$.

To clarify this situation, we show on Fig. 5.4 the relation between the seismic and *Gaia* parallaxes, separately for RGB and RC stars. While the latter display a relation nearly parallel to the 1:1 line, RGB stars show a slope of 1.028 ± 0.007 , which is significantly different from 1 and is not solely due to a correlation effect. Because all sources are treated as single stars in *Gaia* DR2, the results for resolved binaries may sometimes be spurious due to confusion of the components (Lindegren et al., 2018). The Renormalised Unit Weight Error (RUWE) is recommended as a goodness-of-fit indicator for *Gaia* DR2 astrometry (see the technical note *GAIA-C3-TN-LU-LL-124-01* available from the DPAC Public Documents page³). It is computed from the following quantities:

- $\chi^2 = \text{astrometric_chi2_al}$;
- $N = \text{astrometric_n_good_obs_al}$;
- G ;
- and $G_{\text{BP}} - G_{\text{RP}}$.

Figure 5.5 shows the distribution of the RUWE for stars in the *Kepler* field, including both RGB and RC evolutionary phases (their distinction does not affect the shape of the distribution). Because there seems to be a breakpoint around $\text{RUWE} = 1.2$ between the expected distribution for well-behaved solutions and the

³<https://www.cosmos.esa.int/web/gaia/public-dpac-documents>

long tail towards higher values, we adopt $\text{RUWE} \leq 1.2$ as a criterion for “acceptable” solutions. By imposing this condition, the scatter is reduced, but the slope appearing in Fig. 5.4 is still present and the offset remains unchanged. Therefore, this steep slope could potentially be a symptom of biases in the seismic scaling relations. To a good approximation, the changes in the slope due to changes in T_{eff} , or modifications in the scaling relations, can be obtained as linear perturbations of Eq. (5.6). The question of their calibration using *Gaia* data is addressed in Sect. 5.1.6. In addition, the similar distributions of the RUWE for RGB and RC stars also point in favour of the fact that the quality of *Gaia* parallaxes is not responsible for the different behaviour of these stars in Figs. 5.2 and 5.3.

A fairly strong trend also appears for the parallax difference as a function of the G -band magnitude, especially in the case of RGB stars (Fig. 5.2, top middle panel). Within *Gaia* itself, observations are acquired in different instrumental configurations and need to be calibrated separately depending on, e.g., the window class and the gate activation (for further details see, e.g., [Riello et al., 2018](#)). In the range of magnitudes covered by red-giant stars, several changes occur:

- at $G = 11.5$, the BP/RP (Blue Photometer/Red Photometer) window class switches from 2D to 1D;
- at $G = 12$, there is the transition between gated (to avoid saturation affecting bright sources) and ungated observations;
- at $G = 13$, the AF (Astrometric Field) window class changes from 2D to 1D.

In order to separate the different effects, we divide the RGB and RC samples in bins of G as follows: $G \leq 11.5$, $G \in [11.5, 12]$, $G \in [12, 13]$, and $G > 13$. Doing so results in an offset decreasing from 16 to $-21 \mu\text{as}$ between the lowest and the highest bins for RGB stars, and from -28 to $-44 \mu\text{as}$ for RC stars. We remark that the trend of the offset with increasing magnitude is negative in both cases, but stronger for RGB stars than for RC stars (see top middle panels in Figs. 5.2 and 5.3), which

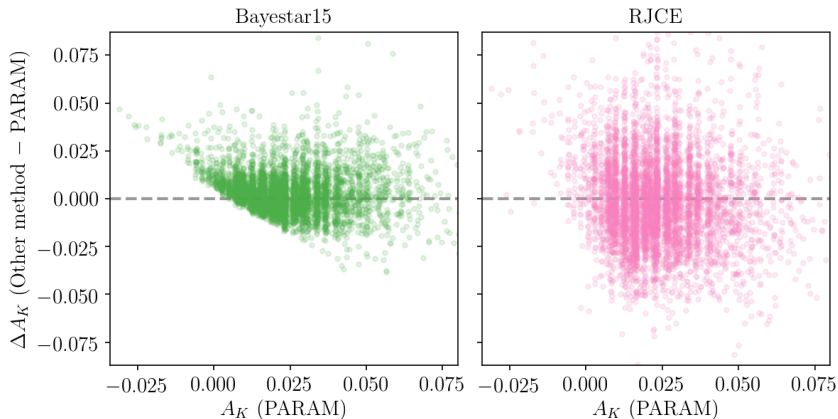


Figure 5.6: Absolute difference in A_K between the [Green et al. \(2015\)](#) map (left) / RJCE method (right) and PARAM, as a function of PARAM’s extinctions.

might again indicate a problem regarding the raw scaling relations. $\Delta\varpi$ does not seem to exhibit any noteworthy relation with the other stellar parameters. Hence, they will not be shown throughout the rest of the paper, apart from ν_{\max} which is an important asteroseismic indicator of the evolutionary stages.

Despite the above, a considerable advantage of using the raw scaling relations is to give us the agility and flexibility to have a direct test of potential systematic effects. Besides, later we will show that a lot of the departures of the slopes from unity can be removed by using grid-based modelling (Sect. 5.1.4). Here, we explore the influence that other non-seismic inputs, i.e. the effective temperature scale and the extinctions, may have on the comparison. T_{eff} appears explicitly in Eq. (5.6), but also implicitly through the bolometric correction contained in the coefficient c_λ , the definition of which is given in Sect. 5.1.3. The combination of these two factors leads to an increase (decrease) of both the $\varpi_{\text{scaling}} - \varpi_{\text{Gaia}}$ slope coefficient and the offset with increasing (decreasing) T_{eff} : a ± 100 K shift results in a ± 10 - $15 \mu\text{s}$ variation in the parallax difference. Reducing the effective temperature by 100 K is almost enough to obtain a slope of ~ 1 , but not to have an offset in agreement with the red clump. On the other hand, setting the extinctions to zero or doubling their values barely affects the parallax difference, at the order of $\pm 6 \mu\text{s}$ at the most. As a check, in Fig. 5.6, we compare our extinction values with those

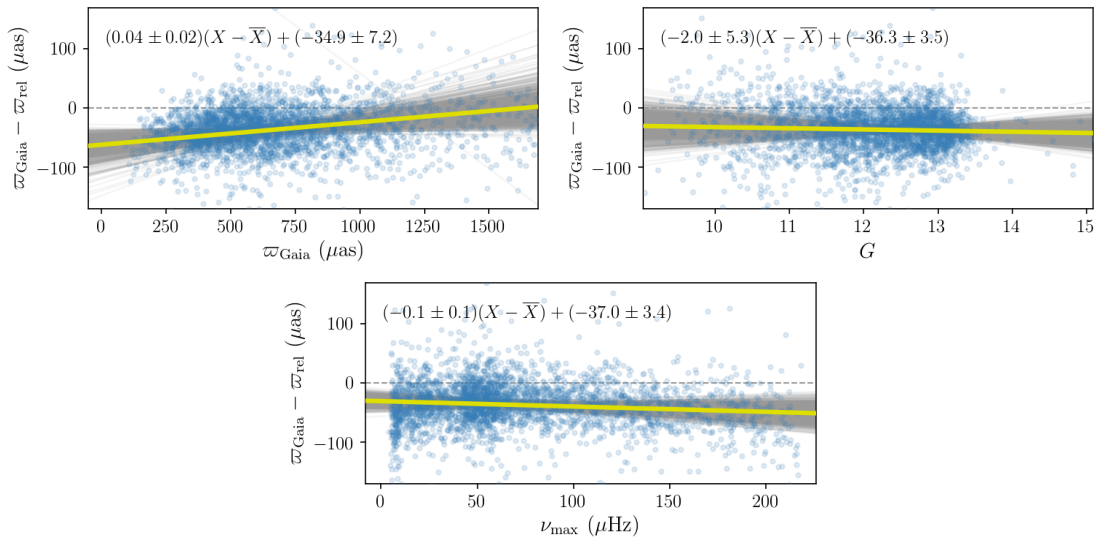


Figure 5.7: Same as Fig. 5.2 with the asteroseismic parallax derived from the scaling relations, where a 2.7% correction factor has been applied to the $\langle \Delta\nu \rangle$ scaling. The summary statistics are: $(\overline{\Delta\varpi})_m = -35.8 \pm 1.3 \mu\text{as}$, $(\overline{\Delta\varpi})_w = -35.5 \pm 0.8 \mu\text{as}$, and $z = 0.88$.

derived by [Green et al. \(2015\)](#) (Bayestar15) and from the RJCE method ([Majewski et al., 2011](#)), to see if they are consistent with each other. For the most part, the differences are within the ± 0.02 level, with a larger scatter on the RJCE’s side. The typical (median) uncertainties on the extinctions are 0.007, 0.002, and 0.025 for PARAM, Bayestar15, and RJCE, respectively. At low extinction values ($A_K < 0.025$), Bayestar15’s extinctions are systematically larger, introducing a diagonal shape in the distribution: this is most likely a truncation effect caused by the fact that Bayestar15 only provides strictly non-negative extinction estimates, while PARAM derives both positive and negative A_K ([Rodrigues et al., 2014](#)). Such differences are not expected to significantly affect our comparison, as already implied by the above tests: the parallax offsets measured with these extinctions only differ by approximately $\pm 2 \mu\text{as}$. This is also partly due to the fact that we are using an infrared passband, which reduces the impact of reddening.

Corrected $\langle \Delta\nu \rangle$ scaling relation

From theoretical models, one expects that deviations from the $\langle \Delta\nu \rangle$ scaling relation depend on mass, chemical composition, and evolutionary state, as discussed in Sect.

5.1.3. Nevertheless, at fixed mass and metallicity (e.g. for a cluster), one can derive a relative correction to the scaling between RGB and RC stars, modifying Eq. (5.1) as follows: $\langle \Delta\nu \rangle' = \mathcal{C}_{\langle \Delta\nu \rangle} \langle \Delta\nu \rangle$, where $\mathcal{C}_{\langle \Delta\nu \rangle}$ is a correction factor. This was done for the open cluster NGC 6791: [Miglio \(2012\)](#) compared asteroseismic and photometric radii, while [Sharma et al. \(2016\)](#) estimated $\mathcal{C}_{\langle \Delta\nu \rangle}$ along each stellar track of a grid of models (see also [Rodrigues et al., 2017](#)). Both found a relative correction of $\sim 2.7\%$ between the two evolutionary stages, $\mathcal{C}_{\langle \Delta\nu \rangle}$ being larger and closer to unity for RC stars. The value of 2.7% corresponds to the low-mass end ($M \sim 1.1 M_{\odot}$); the relative correction would be of the order of 2.5% for $1.2\text{-}1.3 M_{\odot}$ stars.

Hence, as a first-order approximation, we apply this correction to our RGB sample: namely, for each star, we reduce $\langle \Delta\nu \rangle$ from the scaling relation by 2.7% . As this correction is based on a definition of $\langle \Delta\nu \rangle$ from individual frequencies, it makes sense to use $\langle \Delta\nu \rangle$ from [Yu et al. \(2018\)](#) to ensure consistency. Fig. 5.7 shows how the inclusion of this correction from modelling affects the comparison for stars along the RGB. After applying the relative correction, the estimated offset becomes $-35 \mu\text{as}$, which is much closer to what was obtained with RC stars (Fig. 5.3), possibly indicating the relevance of the correction. However, even if the relations of $\Delta\varpi$ with the *Gaia* parallax and the *G*-band magnitude seem flatter, the $\varpi_{\text{rel}} - \varpi_{\text{Gaia}}$ relation now displays a slope of 0.984 ± 0.007 . This is most likely due to the application of an average correction initially derived for NGC 6791, and not quite suitable for the wide range of masses and metallicities covered by the sample. Finally, to help quantifying the effect of this correction, we also estimate the slope and the parallax offset using $\langle \Delta\nu \rangle$ from [Mosser et al. \(2011a\)](#), as in the previous section, and we obtain 0.974 and $-43 \mu\text{as}$. Thus, the dominant effect here is that of the correction, rather than the change of $\langle \Delta\nu \rangle$.

$\langle \Delta\nu \rangle$ from individual frequencies: grid-modelling

With their Bayesian tool PARAM, [Rodrigues et al. \(2017\)](#) replaced the $\langle \Delta\nu \rangle$ scaling relation with an average large frequency definition stemming from a linear fitting

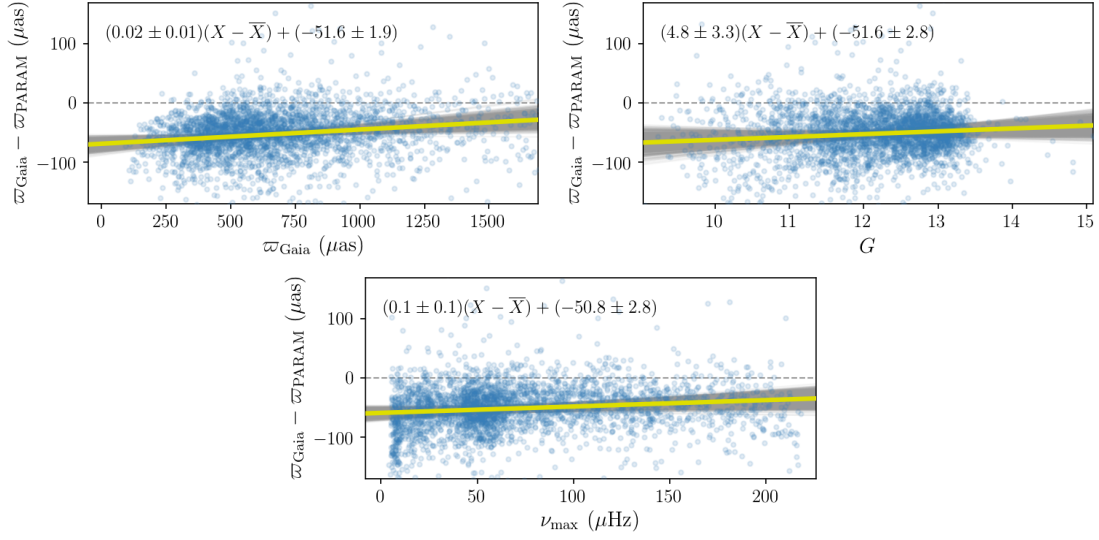


Figure 5.8: Same as Fig. 5.2 with the asteroseismic parallax derived from PARAM (Rodrigues et al., 2017). The summary statistics are: $(\overline{\Delta\varpi})_{\text{m}} = -51.4 \pm 1.0 \mu\text{as}$, $(\overline{\Delta\varpi})_{\text{w}} = -51.7 \pm 0.8 \mu\text{as}$, and $z = 1.24$.

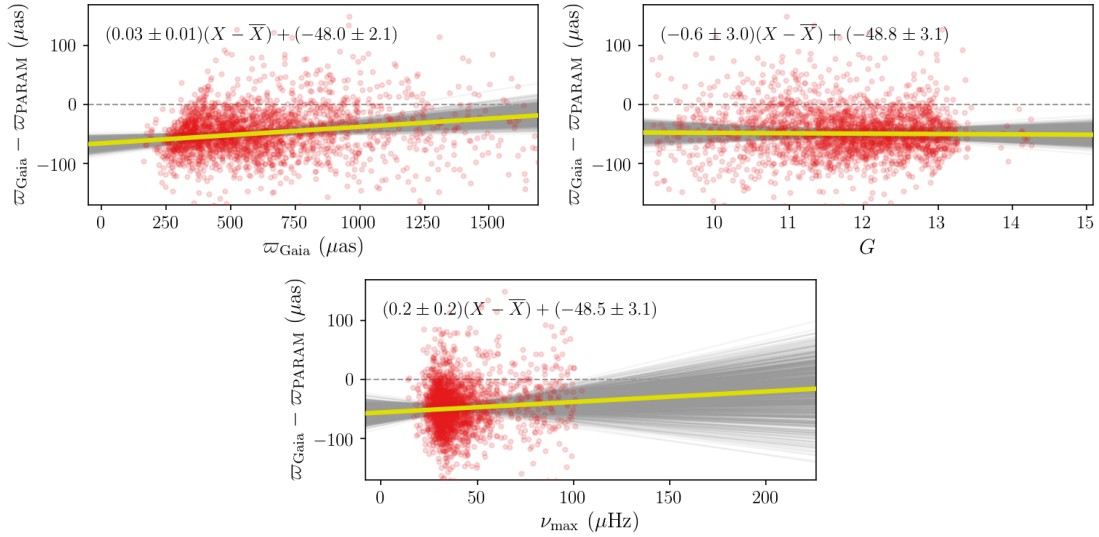


Figure 5.9: Same as Fig. 5.8 for RC stars. The summary statistics are: $(\overline{\Delta\varpi})_{\text{m}} = -48.3 \pm 1.1 \mu\text{as}$, $(\overline{\Delta\varpi})_{\text{w}} = -47.9 \pm 0.9 \mu\text{as}$, and $z = 1.23$.

of the individual radial-mode frequencies computed along the evolutionary tracks of the grid. Similarly, and as stated above, we use $\langle\Delta\nu\rangle$ as estimated by [Yu et al. \(2018\)](#) for consistency with the $\langle\Delta\nu\rangle$ definition adopted in the models in PARAM. At this time, this approach has yielded masses / radii that show no systematic deviations to within a few percent of independent estimates (see, e.g., [Miglio et al. 2016](#); [Handberg et al. 2017](#); [Rodrigues et al. 2017](#); [Brogaard et al. 2018](#), who partially revisited the work by [Gaulme et al. 2016](#)). This method requires the use of a grid of models covering the complete relevant range of masses, ages, and metallicities. It is worth emphasising that the physical inputs of the models play a crucial role in the determination of stellar parameters via a Bayesian grid-based method. There is no absolute set of stellar models, and a few changes in their ingredients may also affect the outcome of an investigation such as ours. For details about the models considered here, we refer the reader to [Rodrigues et al. \(2017\)](#), with the exception that we include element diffusion.

The comparison of the *Gaia* parallaxes with the seismic ones estimated with PARAM appears on Figs. 5.8, for RGB stars, and 5.9, for RC stars. Both evolutionary phases have a flattened relation with ϖ_{Gaia} , such that they now display similar slopes. In the RGB sample, the $\varpi_{\text{PARAM}}-\varpi_{\text{Gaia}}$ relation has a slope nearly equal to unity: 0.998 ± 0.003 ; that of RC stars is largely unchanged (see Fig. 5.4). These effects bring the parallax zero-points really close: -52 and $-48 \mu\text{as}$ for RGB and RC stars, respectively. The trends with G are also relatively flat, resulting in small fluctuations as we move from low to high G magnitudes: from -58 to $-51 \mu\text{as}$ for stars on the RGB, and from -46 to $-52 \mu\text{as}$ in the clump. These findings are reassuring in the sense that, if we were to find a trend with parallax or an evolutionary-state dependent offset, the issue would be down to seismology. Since we do not observe such effects, it seems relevant to use PARAM with appropriate constraints to derive asteroseismic parallaxes. If we were to combine PARAM with $\langle\Delta\nu\rangle$ estimates from [Mosser et al. \(2011a\)](#) instead, the RGB and RC offsets would become -62 and

$-46 \mu\text{as}$, respectively. This introduces a significant RGB / RC relative difference in the parallax zero-point, which is neither due to the presence of secondary clump stars, nor to the different ν_{max} ranges covered by RGB and RC stars. Furthermore, the effect on the slopes is a decrease for RGB stars (0.986) and a very mild increase for RC stars (1.002). Again, these findings highlight the importance of ensuring consistency in the $\langle\Delta\nu\rangle$ definition between observations and models.

What follows below aims at quantifying how sensitive the findings with PARAM are on additional systematic biases such as changes in the T_{eff} and $[\text{Fe}/\text{H}]$ scales, and the use of different model grids. We tested that a ± 100 K shift in T_{eff} affects $\Delta\varpi$ by $\pm 3 \mu\text{as}$ for RGB stars, but this left the results largely unchanged for RC stars. It is not surprising that the order of magnitude of these variations is lower compared to when we used the scaling relations at face value ($\pm 10\text{-}15 \mu\text{as}$). The grid of models restricts the possible range of T_{eff} values for a star with a given mass and metallicity, even more so when dealing with the very localised core-helium burning stars. Then, a ± 0.1 dex shift in $[\text{Fe}/\text{H}]$ affects $\Delta\varpi$ by ∓ 4 and $\mp 2 \mu\text{as}$ for RGB and RC stars, respectively. Finally, when considering models computed without diffusion (described in [Rodrigues et al., 2017](#)), the parallax zero-point slightly increases for RGB stars ($\Delta\varpi \sim -57 \mu\text{as}$) and decreases for RC stars ($\Delta\varpi \sim -41 \mu\text{as}$), enhancing the discrepancy between the two evolutionary phases. Grids of models computed with and without diffusion differ, e.g., in terms of the mixing-length parameter, and of the initial helium and heavy-elements mass fractions obtained during the calibration of a solar model. Because of these combined effects, it is complex to interpret the respective impacts on RGB and RC stars. Since models with diffusion are in better agreement with, e.g., the helium abundance estimated in the open cluster NGC 6791 ([Brogaard et al., 2012](#)) and constraints on the Sun from helioseismology ([Christensen-Dalsgaard, 2002](#)), they are our preferred choice for the current study. However, we stress that, at this level of precision, uncertainties related to stellar models are non-negligible (see [Miglio et al. 2021](#)).

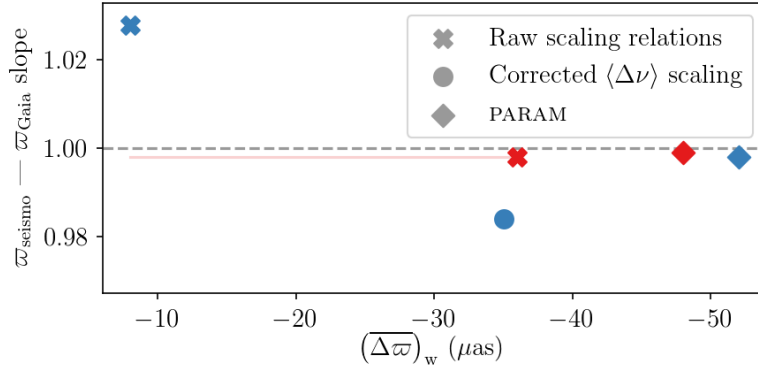


Figure 5.10: Slope of the various $\varpi_{\text{seismo}} - \varpi_{\text{Gaia}}$ relations — using raw scaling relations (crosses; Sect. 5.1.4), a corrected $\langle\Delta\nu\rangle$ scaling relation (circles; Sect. 5.1.4), and PARAM (diamonds; Sect. 5.1.4) — as a function of the weighted average parallax difference for RGB (blue) and RC (red) stars. For RC stars, the line is extended to lower offset values for a better visualisation of how the slope compares with RGB stars when using scaling relations at face value.

As a summary, Fig. 5.10 shows how the $\varpi_{\text{seismo}} - \varpi_{\text{Gaia}}$ slopes and parallax offsets (weighted average parallax difference) evolve as we move from the scaling relations taken at face value to grid-based modelling, illustrating the convergence of RGB and RC stars both in terms of slope and offset when using PARAM.

External validation with open clusters

We perform an external validation of our findings by using independent measurements for the open clusters NGC 6791 and NGC 6819, both in the *Kepler* field. We adopt the distances given by eclipsing binaries: $d_{\text{NGC 6791}} = 4.01 \pm 0.14$ kpc (Brogaard et al., 2011) and $d_{\text{NGC 6819}} = 2.52 \pm 0.15$ kpc (Handberg et al., 2017). The comparison with *Gaia* DR2 parallax measurements (Cantat-Gaudin et al., 2018) gives offsets of -60.6 ± 8.9 μas and -40.4 ± 23.6 μas for the former and the latter, respectively. This is reassuring as it is in line with the results obtained with PARAM.

Influence of spatial covariances

As discussed by Lindegren et al. (2018) (see also Arenou et al., 2018), spatial correlations are present in the astrometry, leading to small-scale systematic errors. The latter have a size comparable to that of the focal plane of *Gaia*, i.e. $\sim 0.7^\circ$. In

comparison, the *Kepler* field, with an approximate radius of 7° , is very large. The uncertainty on the inferred parallax offset may be largely underestimated, unless one takes these spatial correlations into account. For this reason, we perform a few tests in order to quantify how the various quantities derived in this work (average parallax difference and slope of the linear fits) and their uncertainties would be affected by the presence of spatial covariances. To be as representative as possible, in terms of spatial and distance distributions, we choose to work with our *Kepler* sample.

We first consider the seismic parallaxes estimated with PARAM as the “true” parallaxes (ϖ_{true}). This is an arbitrary choice and, thereafter, ϖ_{true} has to be viewed as a synthetic set of true parallaxes, completely independent from seismology. From there, we have to compute synthetic seismic and astrometric parallaxes. The former are calculated using the observed uncertainties on PARAM parallaxes ($\sigma_{\varpi_{\text{seismo}}}$):

$$\varpi_{\text{seismo}} = \varpi_{\text{true}} + \mathcal{N}(0, \sigma_{\varpi_{\text{seismo}}}^2), \quad (5.9)$$

where $\mathcal{N}(0, \sigma_{\varpi_{\text{seismo}}}^2)$ is a normal distribution with mean zero and variance $\sigma_{\varpi_{\text{seismo}}}^2$. Then, two sets of astrometric parallaxes are simulated, using the observed uncertainties on *Gaia* parallaxes ($\sigma_{\varpi_{\text{Gaia}}}$):

$$\varpi_{\text{Gaia}}^{\text{unc}} = \varpi_{\text{true}} + \mathcal{N}(0, \sigma_{\varpi_{\text{Gaia}}}^2) + \mathcal{O}_{\text{Gaia}}, \quad (5.10)$$

$$\varpi_{\text{Gaia}}^{\text{cor}} = \varpi_{\text{true}} + \mathcal{N}(0, \sigma_{\varpi_{\text{Gaia}}}^2) + \mathcal{N}(\mathcal{O}_{\text{Gaia}}, \mathcal{S}), \quad (5.11)$$

where $\mathcal{O}_{\text{Gaia}} = -50 \mu\text{as}$ represents the *Gaia* parallax zero-point and is set arbitrarily following our findings (Sect. 5.1.4), and $\mathcal{N}(\mathcal{O}_{\text{Gaia}}, \mathcal{S})$ is a multivariate normal distribution with mean $\mathcal{O}_{\text{Gaia}}$ and covariance matrix \mathcal{S} . These two parallaxes contain the same random error component ($\mathcal{N}(0, \sigma_{\varpi_{\text{Gaia}}}^2)$), but different systematic error components. $\varpi_{\text{Gaia}}^{\text{unc}}$ (Eq. (5.10)) has a systematic error that is simply equal to the *Gaia* zero-point; while $\varpi_{\text{Gaia}}^{\text{cor}}$ (Eq. (5.11)) has a systematic error centred on $\mathcal{O}_{\text{Gaia}}$

but also accounts for spatial correlations between the sources.

The spatially-correlated errors are assumed to be independent from the random errors, and the corresponding covariance matrix can be written as:

$$\mathcal{S} = E[(\varpi_i - \mathcal{O}_{\text{Gaia}})(\varpi_j - \mathcal{O}_{\text{Gaia}})] = \begin{cases} V_{\varpi}(0) & \text{if } i = j \\ V_{\varpi}(\theta_{ij}) & \text{if } i \neq j \end{cases}, \quad (5.12)$$

where $V_{\varpi}(\theta)$ is the spatial covariance function which solely depends on the angular distance between sources i and j (θ_{ij}). [Lindegren et al. \(2018\)](#) suggested

$$V_{\varpi}(\theta) \simeq (285 \mu\text{as}^2) \times \exp(-\theta/14^\circ) \quad (5.13)$$

as the spatial correlation function for the systematic parallax errors. To capture the variance at the smallest scales (see Fig. 14 of [Lindegren et al., 2018](#)), an additional exponential term can be added:

$$V_{\varpi}(\theta) \simeq (285 \mu\text{as}^2) \times \exp(-\theta/14^\circ) + (1565 \mu\text{as}^2) \times \exp(-\theta/0.3^\circ), \quad (5.14)$$

where the number $1565 \mu\text{as}^2$ is chosen to get a total $V_{\varpi}(0)$ of $1850 \mu\text{as}^2$, appearing in the overview of *Gaia* DR2 astrometry by [Lindegren et al.](#)⁴. This value was obtained for quasars, with faint magnitudes ($G \geq 13$); for brighter magnitudes (Cepheids), there are indications that a total $V_{\varpi}(0)$ of $440 \mu\text{as}^2$ would be required instead. However, owing to the uncertainty regarding the exact value that would be suitable for our sample, we prefer to be conservative by using Eq. (5.14). Lastly, we also try the description of spatial covariances following [Zinn et al. \(2019\)](#), namely:

$$V_{\varpi}(\theta) \simeq (135 \mu\text{as}^2) \times \exp(-\theta/14^\circ). \quad (5.15)$$

As the term $\mathcal{N}(\mathcal{O}_{\text{Gaia}}, \mathcal{S})$ in Eq. (5.11) is subject to important variations between

⁴<https://www.cosmos.esa.int/web/gaia/dr2-known-issues> (slide 35)

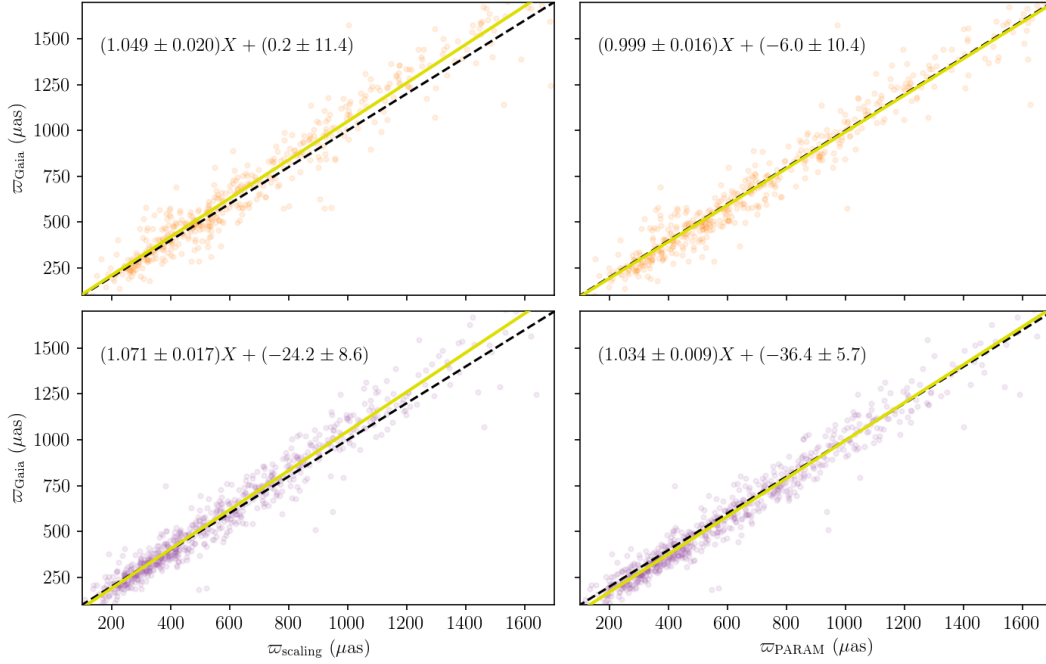


Figure 5.11: ϖ_{Gaia} as a function of ϖ_{scaling} (left) and ϖ_{PARAM} (right), for red giants in the *K2* Campaign 3 (top) and 6 (bottom) fields. The yellow line displays the linear fit, averaged over N realisations, for which the relation is given at the top of each subplot. The black dashed line indicates the 1:1 relation. The summary statistics are: $(\overline{\Delta\varpi})_{\text{m}} = 28.9 \pm 5.2 \mu\text{as}$, $(\overline{\Delta\varpi})_{\text{w}} = 24.6 \pm 4.0 \mu\text{as}$, and $z = 1.16$ for C3 (scaling); $(\overline{\Delta\varpi})_{\text{m}} = 11.9 \pm 3.6 \mu\text{as}$, $(\overline{\Delta\varpi})_{\text{w}} = 9.5 \pm 2.6 \mu\text{as}$, and $z = 1.01$ for C6 (scaling); $(\overline{\Delta\varpi})_{\text{m}} = -8.1 \pm 4.4 \mu\text{as}$, $(\overline{\Delta\varpi})_{\text{w}} = -6.4 \pm 3.8 \mu\text{as}$, and $z = 1.30$ for C3 (PARAM); $(\overline{\Delta\varpi})_{\text{m}} = -18.6 \pm 3.3 \mu\text{as}$, $(\overline{\Delta\varpi})_{\text{w}} = -16.9 \pm 2.4 \mu\text{as}$, and $z = 1.11$ for C6 (PARAM).

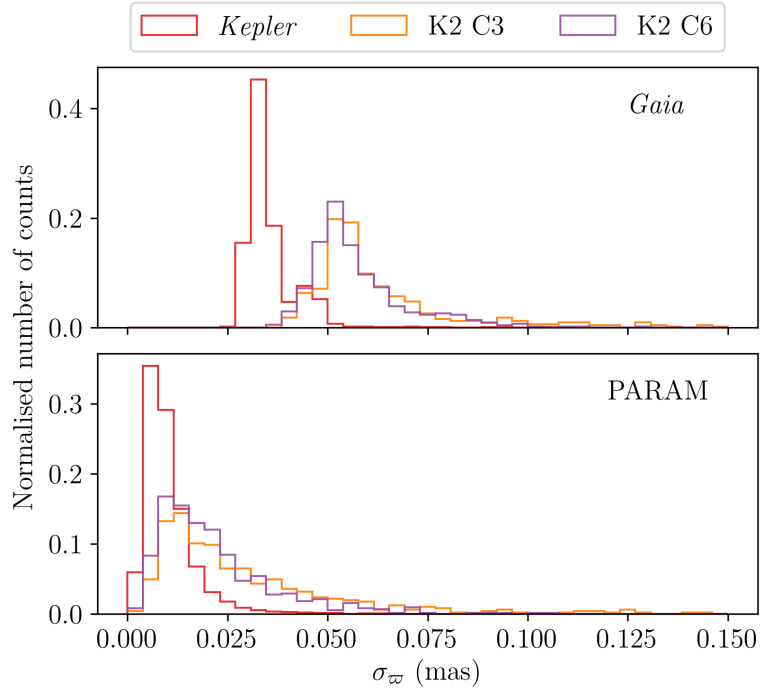


Figure 5.12: Distribution of the parallax uncertainties in *Gaia* DR2 (top) and in PARAM (bottom) for the *Kepler* (red), C3 (orange), and C6 (purple) fields.

different simulations, we draw $N_{\text{sims}} = 1000$ realisations of $\varpi_{\text{Gaia}}^{\text{cor}}$ in order to obtain statistically significant results. Furthermore, because it is computationally expensive to calculate the covariance matrix for a large number of sources, we randomly select 60% of the RGB and RC samples beforehand. This allows us to calculate the median parallax difference between the astrometric and seismic synthetic values, as well as its uncertainty. Whether spatial covariances are included or not, we obtain a similar offset, very close to the parallax zero-point applied ($\mathcal{O}_{\text{Gaia}} = -50 \mu\text{as}$), for both RGB and RC stars. The difference becomes apparent when one looks at the uncertainty on the median offset. Without spatial correlations, we find an uncertainty of approximately $1 \mu\text{as}$, which is compatible with our results. However, when spatial correlations are included, the uncertainty increases up to $\sim 14 \mu\text{as}$ using Eqs. (5.13) and (5.14), and it is slightly lower with Eq. (5.15) ($\sim 10 \mu\text{as}$). A similar threshold on the uncertainty of the parallax offset, due to spatial covariances, was recently found by [Hall et al. \(2019\)](#), who used hierarchical Bayesian modelling and assumptions about the red clump to compare *Gaia* and asteroseismic parallaxes

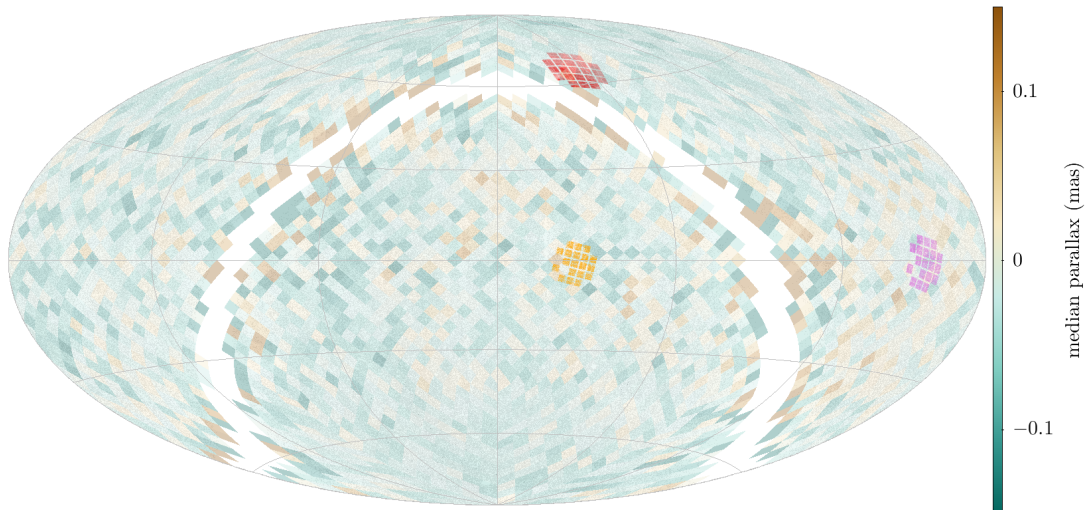


Figure 5.13: Sky map in ecliptic coordinates of the median parallaxes for the full quasar sample, showing large-scale variations of the parallax zero-point. The *Kepler* (red), C3 (orange), and C6 (purple) fields are displayed. Median values are calculated in cells of $3.7 \times 3.7 \text{ deg}^2$.

in the *Kepler* field. Then, studying the relation between the simulated seismic and *Gaia* parallaxes (in a similar way as on Fig. 5.4), we find that, regardless of the spatial covariance function applied, the value and uncertainty of the slope parameter are barely affected. This is reassuring since it means that the slopes we obtained in Sects. 5.1.4, 5.1.4, and 5.1.4 are significant, and that the argument whereby PARAM displays a slope closer to unity compared to the raw scaling relations is still valid.

5.1.5 Positional Dependence of the Parallax Zero-Point

This section aims at highlighting how the position constitutes one of the sources of the variations in the *Gaia* DR2 parallax zero-point. After measuring the offset in the *Kepler* field, we undertake a similar analysis for two of the *K2* Campaign fields: C3 and C6, corresponding to the south and north Galactic caps respectively (Howell et al., 2014). A difference lies in the fact that there is no distinction between the RGB and the RC evolutionary stages here. In the following, we are concerned with the results given by raw scaling relations and PARAM, using the method developed by Mosser et al. (2011a) for $\langle \Delta\nu \rangle$ for both as there is no $\langle \Delta\nu \rangle$ available following the approach by Yu et al. (2018). After that, we also analyse the information given

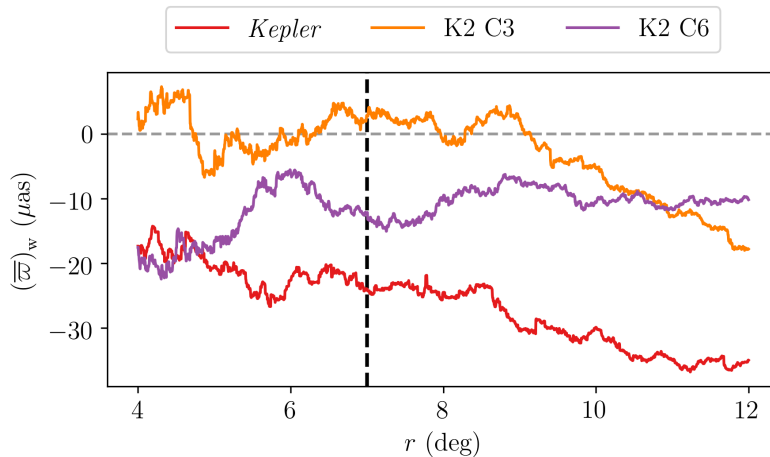


Figure 5.14: Weighted average parallax of the quasars selected within a given radius around the central coordinates of the *Kepler* (red), C3 (orange), and C6 (purple) fields. The black dashed line indicates the average radius of the fields.

by quasars regarding the three fields considered in our investigation.

***K2* fields: C3 and C6**

The comparison of parallaxes using the raw scalings with parallaxes from *Gaia* DR2 is displayed on Fig. 5.11, and the measured offsets are of the order of 25 ± 4 and $9 \pm 3 \mu\text{as}$ for C3 and C6, respectively. Both have a $\varpi_{\text{scaling}} - \varpi_{\text{Gaia}}$ relation with a slope substantially different from unity, i.e. 1.049 ± 0.020 for C3 and 1.071 ± 0.017 for C6. Besides, T_{eff} shifts of ± 100 K affect the parallax difference by $\pm 10\text{-}15 \mu\text{as}$, as is the case for *Kepler*.

For PARAM, the outcome of the comparison is also illustrated on Fig. 5.11. C3 displays a parallax difference close to zero ($\Delta\varpi \simeq -6 \pm 4 \mu\text{as}$), while C6 shows a value of about $-17 \pm 2 \mu\text{as}$. In the case of C3, the trend with parallax is entirely suppressed: the slope is equal to 0.999 ± 0.016 . It is also reduced for C6, but a fairly steep slope of 1.034 ± 0.009 remains. In absolute terms, these offsets are much lower compared to the *Kepler* field even though we are dealing with red-giant stars, either in the RGB or the RC phase, in both cases. Thus, in the position-magnitude-colour dependence of the parallax zero-point, the position prevails in the current analysis. As to whether these differences are caused by the inhomogeneity in the

effective temperatures and metallicities in use between the *Kepler* and *K2* samples, [Casagrande et al. \(2019\)](#) checked the reliability of their photometric metallicities against APOGEE DR14 and found an offset of -0.01 dex with an RMS of 0.25 dex, i.e. SkyMapper’s $[\text{Fe}/\text{H}]$ are lower. T_{eff} from SkyMapper agree with APOGEE DR14 within few tens of K and a typical RMS of 100 K. These small deviations should not affect our findings. Also, we compare the extinctions from PARAM, adopted in this work, to those from SkyMapper, which are used to determine T_{eff} and $[\text{Fe}/\text{H}]$, and find that they are consistent with each other, with differences in A_K only at the level of ± 0.01 . Finally, we investigate the potential origin of the differing slopes between C3 and C6, by considering the different parallax distributions (with respect to each other, and also to the *Kepler* field), the decreased quality of the *K2* seismic data compared to *Kepler* ([Howell et al., 2014](#)), and the use of $\langle \Delta\nu \rangle$ from [Mosser et al. \(2011a\)](#) (instead of [Yu et al., 2018](#), as for *Kepler*). Nevertheless, the interplay between these different elements as well as the limited number of stars in the *K2* samples prevent us from drawing any firm conclusion with regards to the slopes. As for the offsets, the effect of such differences seems to be at the level of $\sim \pm 7 \mu\text{as}$ at most. In addition, the fairly good agreement between SkyMapper and APOGEE does not exclude the possibility that the photometric T_{eff} and $[\text{Fe}/\text{H}]$ may be influenced differently in different fields (e.g. C3 and C6) by external factors such as, e.g., the extinction.

A further point we would like to raise concerns the apparent larger scatter in the *K2* fields. In that respect, we identify the order of magnitude of the *Gaia* and seismic (PARAM) parallax uncertainties (Fig. 5.12). The asteroseismic uncertainties are slightly larger in the case of *K2*. This can mainly be explained by the fact that the original mission, *Kepler*, continuously monitored stars for four years, whereas each campaign of *K2* is limited to a duration of approximately 80 days ([Howell et al., 2014](#)). Despite this, photometric systematics in the *K2* data leading to, e.g., spurious frequencies are now well understood, and the pipelines used to produce lightcurves

have been developed over time to remove or mitigate these effects. As a result, we do not expect the global seismic parameters to show any significant bias due to the *K2* artefacts (see also [Hekker et al., 2012](#), and the *Kepler* and *K2* Science Center website⁵). Nonetheless, the astrometric uncertainties are also substantially larger for *K2*, almost doubled compared to *Kepler*. A possible reason for this would be that the regions around the ecliptic plane (such as C3 and C6) are observed less frequently, as a result of the *Gaia* scanning law, and also under less favourable scanning geometry, with the scan angles not distributed evenly ([Gaia Collaboration et al., 2016a](#)). To test this hypothesis, we use the quantity `visibility_periods_used`: the number of visibility periods, i.e. a group of observations separated from other groups by a gap of at least 4 days, used in the astrometric solution. This way, we can assess if a source is astrometrically well-observed. This variable exhibits significantly higher values for *Kepler*, ranging from 12 to 17. The number of visibility periods for *K2* are lower or equal to ten, indicating that the parallaxes could be more vulnerable to errors. The predicted uncertainty contrast between the *Kepler* and *K2* fields is about a factor⁶ of 1.6, which is indeed consistent with the location of the histogram peaks in the top panel of Fig. 5.12.

Quasars and Colour-Magnitude Diagram

[Lindgren et al. \(2018\)](#) investigated the parallax offset using quasars, and obtained a global zero-point of about $-30 \mu\text{as}$. It is no surprise that this value differs from the ones we obtain in the current work. Indeed, this parallax offset depends on magnitude and colour, in addition to position: quasars generally are blue-coloured with faint magnitudes. Red giants are substantially different objects, hence the importance to solve the parallax zero-point independently. We investigate the information provided by quasars to estimate the parallax zero-point in the different fields considered here (see Fig. 5.13). To this end, we select quasars within a given

⁵<https://keplerscience.arc.nasa.gov/pipeline.html>

⁶<https://www.cosmos.esa.int/web/gaia/science-performance>

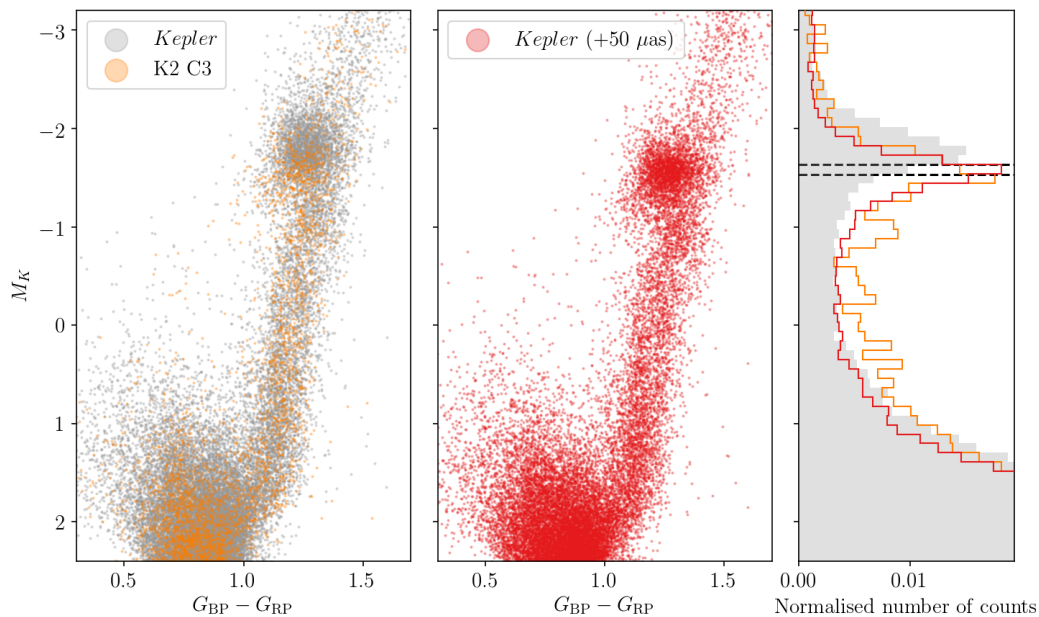


Figure 5.15: Colour-Magnitude Diagrams (CMDs; left and middle) and absolute magnitude M_K normalised histograms (right), where M_K is estimated by means of the *Gaia* parallax at face value for the *Kepler* (grey) and C3 (orange) fields. Another CMD, including a shift in parallax, is shown for *Kepler* (red). We removed stars having a parallax with a relative error above 10% for *Kepler*, and 15% for C3. The black dashed lines indicate the expected range of values for the magnitude of the clump in the K band.

radius around the central coordinates of each field and compute the weighted average parallax (following Eq. (5.7)). The variation of this quantity with radius is shown on Fig. 5.14. This allows us to assess its sensitivity on the size of the region considered. The mean offsets associated to the size of the fields ($r \sim 7^\circ$) are -24 ± 8 , 3 ± 9 , and $-12 \pm 7 \mu\text{as}$ for *Kepler*, C3, and C6, respectively. It should be kept in mind, however, that spatial covariances in the parallax errors (Sect. 5.1.4) prevent one from drawing strong conclusions regarding the offsets, especially at the smallest scales, and the main purpose of Fig. 5.14 is to illustrate the trends. Despite exhibiting different values, the pattern whereby the *Gaia* parallax offset is lowest for C3 and highest for *Kepler*, in keeping with our results, is potentially reproduced.

For illustrative purposes, we show on Fig. 5.15 two Colour-Magnitude Diagrams (CMDs) for the entire *Kepler* field: one where the absolute magnitude is calculated without applying a shift in the *Gaia* parallax, another one where we use the zero-

point measured with PARAM ($\sim -50 \mu\text{as}$ for both RGB and RC stars) to “correct” the parallaxes. In addition, owing to the near-zero offset in C3, the latter is also displayed for comparison. We only keep stars with a relative parallax error below 10 % for *Kepler*, and 15 % for C3. Beyond the magnitude values being affected, the shape of the RGB structures, e.g. the red-giant branch bump and the red clump, become clearer when a shift is applied. This is a sensible change, because a constant shift in parallax is not equivalent to a constant shift in luminosity. The parallax shift has a different relative effect on each star’s distance, hence luminosity, which may explain how features in the CMD can become sharper. In particular, the red clump becomes more sharply-peaked in the absolute magnitude distribution and its mean value is about $M_K^{\text{RC}} \sim -1.57$, versus $M_K^{\text{RC}} \sim -1.78$ when *Gaia* parallaxes are taken at face value. Independent determinations of M_K^{RC} range between -1.63 and -1.53 (see Table 1 of Girardi, 2016; Chen et al., 2017; Hawkins et al., 2017). Furthermore, population effects at a level of several hundredths of a magnitude are expected but are not enough to explain the difference in M_K^{RC} , especially considering that the use of the *K* band partly mitigates them (see, e.g., Girardi, 2016, and references therein).

5.1.6 Joint Calibration of the Seismic Scaling Relations and of the Zero-Point in the *Gaia* Parallaxes

In Sect. 5.1.4, we used the scaling relations (Eqs. (5.4) and (5.5)) at face value in the context of a comparison with *Gaia* DR2. These relations are not precisely calibrated yet, and testing their validity has been a very active topic in the field of asteroseismology (e.g. Huber et al., 2012; Miglio et al., 2012b; Gaulme et al., 2016; Sahlholdt et al., 2018). In this vein, *Gaia* DR2 ensures the continuity of the research effort carried out to test the scaling relations’ accuracy. After the work conducted in Sect. 5.1.4 and 5.1.5, it is clear that the scalings’ calibration by means of *Gaia* requires the parallax zero-point to be characterised at the same time. Hence, the

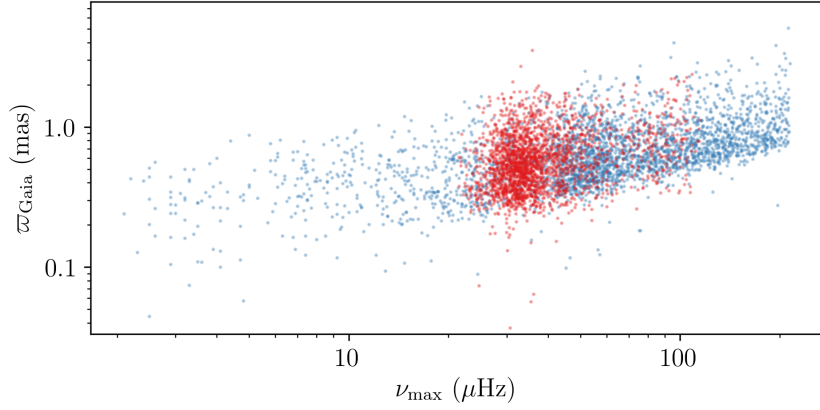


Figure 5.16: ϖ_{Gaia} as a function of ν_{\max} for RGB (blue) and RC (red) stars in the *Kepler* sample.

current investigation reflects two main developments: constraining the calibration of the seismic scaling relations and quantifying the parallax offset in *Gaia* DR2.

We take the seismic calibration issue into account by introducing the scaling factors $\mathcal{C}_{\langle\Delta\nu\rangle}$ and $\mathcal{C}_{\nu_{\max}}$ in the expressions of $\langle\Delta\nu\rangle$ and ν_{\max} (Eqs. (5.1) and (5.2)):

$$\left(\frac{\langle\Delta\nu\rangle}{\langle\Delta\nu\rangle_{\odot}}\right) = \mathcal{C}_{\langle\Delta\nu\rangle} \left(\frac{M}{M_{\odot}}\right)^{1/2} \left(\frac{R}{R_{\odot}}\right)^{-3/2}, \quad (5.16)$$

$$\left(\frac{\nu_{\max}}{\nu_{\max,\odot}}\right) = \mathcal{C}_{\nu_{\max}} \left(\frac{M}{M_{\odot}}\right) \left(\frac{R}{R_{\odot}}\right)^{-2} \left(\frac{T_{\text{eff}}}{T_{\text{eff},\odot}}\right)^{-1/2}. \quad (5.17)$$

In terms of mass and radius (Eqs. (5.4) and (5.5)), this translates into:

$$\left(\frac{M}{M_{\odot}}\right) = \mathcal{C}_{\nu_{\max}}^{-3} \mathcal{C}_{\langle\Delta\nu\rangle}^4 \left(\frac{\nu_{\max}}{\nu_{\max,\odot}}\right)^3 \left(\frac{\langle\Delta\nu\rangle}{\langle\Delta\nu\rangle_{\odot}}\right)^{-4} \left(\frac{T_{\text{eff}}}{T_{\text{eff},\odot}}\right)^{3/2}, \quad (5.18)$$

$$\left(\frac{R}{R_{\odot}}\right) = \mathcal{C}_{\nu_{\max}}^{-1} \mathcal{C}_{\langle\Delta\nu\rangle}^2 \left(\frac{\nu_{\max}}{\nu_{\max,\odot}}\right) \left(\frac{\langle\Delta\nu\rangle}{\langle\Delta\nu\rangle_{\odot}}\right)^{-2} \left(\frac{T_{\text{eff}}}{T_{\text{eff},\odot}}\right)^{1/2}. \quad (5.19)$$

Finally, the seismic parallax (Eq. (5.6)) is modified as follows:

$$\varpi'_{\text{scaling}} = c_{\lambda} \mathcal{C}_{\nu_{\max}} \mathcal{C}_{\langle\Delta\nu\rangle}^{-2} \left(\frac{\nu_{\max}}{\nu_{\max,\odot}}\right)^{-1} \left(\frac{\langle\Delta\nu\rangle}{\langle\Delta\nu\rangle_{\odot}}\right)^2 \left(\frac{T_{\text{eff}}}{T_{\text{eff},\odot}}\right)^{-5/2}. \quad (5.20)$$

In this context, the comparison between the *Gaia* (Eq. (5.3)) and asteroseismic

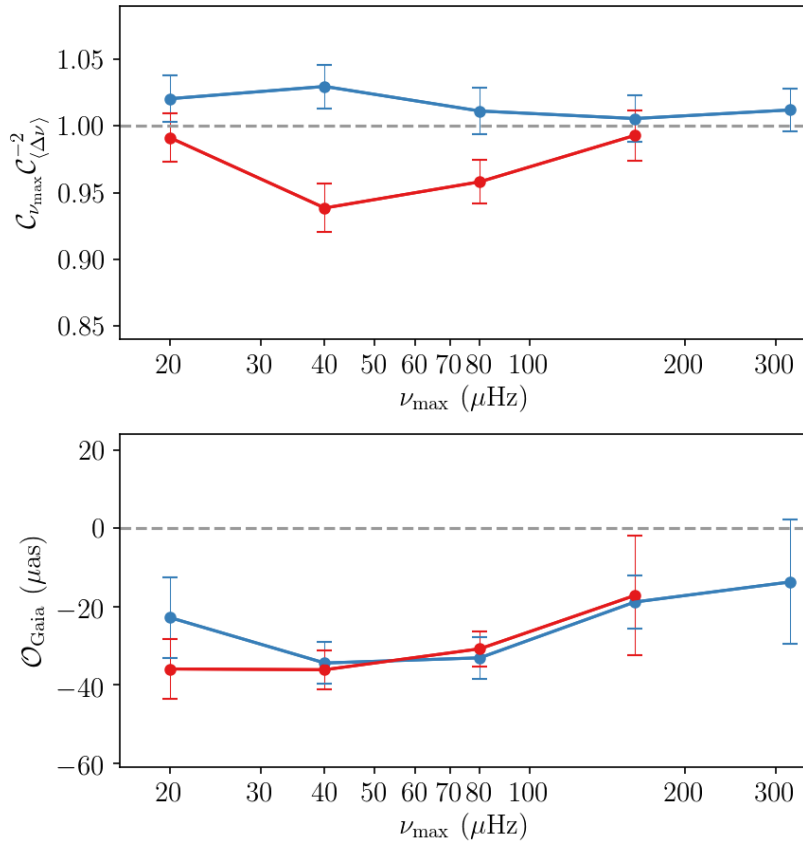


Figure 5.17: Coefficients (left) and offsets (right) determined via our two-step calibration methodology for RGB (blue) and RC (red) stars, as a function of ν_{\max} .

(Eq. (5.20)) expressions for the parallax gives the following equality

$$\varpi_{\text{Gaia}} - \mathcal{O}_{\text{Gaia}} = \mathcal{C}_{\nu_{\text{max}}} \mathcal{C}_{\langle \Delta \nu \rangle}^{-2} \varpi_{\text{scaling}}, \quad (5.21)$$

where $\mathcal{O}_{\text{Gaia}}$ represents the parallax zero-point in *Gaia* DR2 to be determined. Fitting Eq. (5.21) with a RANSAC algorithm allows us to determine the coefficient $\mathcal{C}_{\nu_{\text{max}}} \mathcal{C}_{\langle \Delta \nu \rangle}^{-2}$, accounting for the scaling relations' calibration, and also provides an offset $\mathcal{O}_{\text{Gaia}}$, which we can interpret as a bias in the *Gaia* parallaxes. The main assumption that we make here is that the asteroseismic calibration, in the form of a multiplication factor, and the astrometric calibration, in the form of an addition factor, can be considered independently and do not affect each other. For this reason, it is crucial to make efficient use of both asteroseismic and astrometric data. On the one hand, because corrections to the scaling relations are expected to depend on ν_{max} (see, e.g., Fig. 3 of [Rodrigues et al., 2017](#)), we divide our *Kepler* RGB and RC samples in frequency ranges of ν_{max} values: [8, 32], [16, 64], [32, 128], [64, 256], [128, 512] μHz . On the other hand, nearby stars have more reliable parallaxes (less affected, in relative terms, by the *Gaia* offset) and may, as such, be used to calibrate the scalings. In practice, we implement a two-step methodology to, firstly, calibrate the seismic scaling relations and, secondly, use the calibration coefficients obtained from the first step to determine the *Gaia* zero-point. To do so, we start by selecting stars with large parallaxes in each bin of ν_{max} . As illustrated by Fig. 5.16, the high-parallax threshold has to be chosen differently depending on the ν_{max} bin considered, in order to keep enough stars. Here, the limit is chosen in such a way that at least 500 stars remain in the different ν_{max} ranges. We then interpolate in ν_{max} to estimate the scaling factors and individually correct each seismic parallax. The latter is then compared again to the *Gaia* parallax, this time on the full range of parallaxes, to measure the parallax offset.

During the calibration process, we apply linear fits expressed in the following

form: $\varpi_{\text{Gaia}} = \gamma \varpi_{\text{scaling}} + \delta$, where $\gamma = \mathcal{C}_{\nu_{\text{max}}} \mathcal{C}_{\langle \Delta \nu \rangle}^{-2}$ is the calibration parameter and $\delta = \mathcal{O}_{\text{Gaia}}$ is the offset parameter. The parameters' uncertainties are estimated by repeating RANSAC $N = 1000$ times, where we add a normally distributed noise knowing the observed uncertainties on ϖ_{Gaia} and ϖ_{scaling} . The coefficients, obtained in step 1, and offsets, obtained in step 2, are shown as a function of ν_{max} for RGB and RC stars on Fig. 5.17. The offsets $\mathcal{O}_{\text{Gaia}}$ point in the right direction — *Gaia* parallaxes are smaller — and are in the same order of magnitude for the two evolutionary stages, which validates the calibration of the scaling relations. These offsets do not depend on ν_{max} , and their mean values are $-24 \pm 9 \mu\text{as}$ for RGB stars and $-31 \pm 7 \mu\text{as}$ for RC stars. In regard to the scaling factors, we can make a qualitative comparison with the $\mathcal{C}_{\langle \Delta \nu \rangle}$ estimated from models if we assume $\mathcal{C}_{\nu_{\text{max}}}$ to be equal to unity (uncertainties related to modelling the driving and damping of oscillations prevented theoretical tests of the ν_{max} scaling relation; see, e.g., [Belkacem et al., 2011](#)). According to [Rodrigues et al. \(2017\)](#) (see their Fig. 3), $\mathcal{C}_{\langle \Delta \nu \rangle}$ takes values slightly lower / higher than one for RGB / RC stars in the ranges of mass and metallicity concerning our sample. Additionally, from RGB models, $\mathcal{C}_{\langle \Delta \nu \rangle}$ is expected to decrease before increasing again as we go towards increasing ν_{max} values, with a minimum at $\nu_{\text{max}} \sim 15 \mu\text{Hz}$ depending on mass and metallicity. A similar trend is expected for RC stars but the other way around: $\mathcal{C}_{\langle \Delta \nu \rangle}$ increases before decreasing, and has a maximum at $\nu_{\text{max}} \sim 30 \mu\text{Hz}$ which depends again on M and $[\text{Fe}/\text{H}]$. Also, larger variations of $\mathcal{C}_{\langle \Delta \nu \rangle}$ are expected for RGB stars, which seems in conflict with our findings. Nevertheless, we remind that we derive scaling factors that are averaged in bins of ν_{max} , and it appears that the current results are still in general agreement with expectations from models. At this point, the third Data Release of *Gaia*, coming along with smaller uncertainties, will provide the means to pursue this work, and to derive precise and accurate corrections to the scaling relations.

5.1.7 Conclusions

We combined *Gaia* and *Kepler* data to investigate the *Gaia* DR2 parallax zero-point, showing how the measured offsets depend on the asteroseismic method employed, having a direct illustration of the positional dependence of the zero-point thanks to the *K2* fields, and, finally, introducing a way to address the seismic and astrometric calibrations at the same time.

First of all, the application of three distinct asteroseismic methods, in the course of the comparison with the astrometric parallaxes delivered by the second Data Release of *Gaia*, reveals that there is no absolute standard within asteroseismology. The determination of a zero-point in the *Gaia* parallaxes extensively depends on the seismic approach used, and cannot be dissociated from it. As a matter of fact, the conclusions we draw are not the same whether we use the seismic scaling relations at face value or a grid-based method such as PARAM: the former would suggest a near-zero offset for RGB stars, significantly different from that of RC stars; in contrast, the latter implies a similar deviation with respect to *Gaia* DR2 parallaxes for RGB and RC stars. That said, the offsets measured when using PARAM, ranging from ~ -45 to $-55 \mu\text{as}$ — considering the substantial uncertainties induced by spatially-correlated errors — can be related to previous investigations, especially the one conducted by [Zinn et al. \(2019\)](#) who calibrated seismic radii against eclipsing binary data in clusters and used model-predicted corrections to the $\langle \Delta\nu \rangle$ scaling relation. They obtained very similar offsets of about $-50 \mu\text{as}$ for RGB and RC stars observed by *Kepler*. Our external validation via the measurements from eclipsing binaries in the open clusters NGC 6791 and NGC 6819 also confirms the existence of a parallax offset in that range. The proximity of the PARAM results with these independent tests reaffirms previous findings about the necessity to go beyond the $\langle \Delta\nu \rangle$ scaling for the estimation of stellar properties. Furthermore, the use of different sets of $\langle \Delta\nu \rangle$ values has a non-negligible impact on the inferred offsets, of the order of $\sim 10 \mu\text{as}$. In particular, attention should be paid to the consistency in the definition of $\langle \Delta\nu \rangle$

between the observations and the models. Other systematic effects can arise from, e.g., shifts in the effective temperature and metallicity scales, and changes in the physical inputs of the models, with variations up to $\pm 7 \mu\text{as}$ according to our tests but very likely larger than that due to uncertainties related to stellar models.

We also bring to light the positional dependence of the *Gaia* DR2 parallax zero-point, as demonstrated by [Lindegren et al. \(2018\)](#), by analysing two of the *K2* Campaign fields, C3 and C6, in addition to the *Kepler* field. These fields, corresponding to the south and north Galactic caps, display parallax offsets which are substantially different from *Kepler*'s. A small fraction of these differences may be due, e.g, to the parallax distribution, the quality of the seismic data, and the use of different seismic constraints. But, as of now, it remains difficult to reach a firm conclusion, and the future possibility of extending this analysis to other *K2* Campaign fields may help shedding light on this matter. Also, despite the measured values being slightly different, the offset suggested by quasars reproduces the trend towards the increasing discrepancy with *Gaia* for C3, C6, and *Kepler* (in ascending order). The difference in the calculated zero-point is to be expected because quasars have their own peculiarities (e.g. faint magnitude, blue colour) that are not representative of red-giant stars. Furthermore, such a colour dependence also emerges from the study of δ Scuti stars in the *Kepler* field by [Murphy et al. \(2019\)](#), who found that applying an offset (as high as $30 \mu\text{as}$) resulted in unrealistically low luminosities. Looking forward, having a uniform set of spectroscopic constraints would be very valuable.

Lastly, we initiate a two-step model-independent method to simultaneously calibrate the asteroseismic scaling relations and measure the *Gaia* DR2 parallax zero-point, based on the assumption that these two corrections are fully decoupled. This leads us to promising findings whereby the computed calibration coefficients are qualitatively comparable to those that are derived from models, and the estimated offsets are in the same order of magnitude for RGB and RC stars and suggest that *Gaia* parallaxes are too small — as expected. However, given the non-negligible un-

certainties and the close correlation between the calibration and offset parameters, it is still too soon to draw strong conclusions. In this regard, the third Data Release of *Gaia*, with improved parallax uncertainties and reduced systematics, will offer exciting prospects to continue along the path of calibrating the scaling relations.

5.2 *Gaia* EDR3 Parallax Zero-Point in the *Kepler/K2* and TESS-SCVZ fields

5.2.1 Introduction

In December 2020, the early third intermediate data release of *Gaia* (*Gaia* EDR3; [Gaia Collaboration et al. 2021](#)) - based on 34 months of input data - was published, with updated source list, astrometry, and broad-band photometry in the G , G_{BP} , and G_{RP} bands. This latest release represents a significant improvement in both the precision and accuracy of the astrometry and broad-band photometry, with respect to *Gaia* DR2.

While quasars in DR2 yielded a median parallax of $-29 \mu\text{as}$, this is now reduced to about $-17 \mu\text{as}$ in *Gaia* EDR3, with systematic variations at a level of $\sim 10 \mu\text{as}$ depending on magnitude and colour. Position-dependent variations are also seen on all angular scales, although with smaller amplitudes than in DR2 ([Lindegren et al., 2021a](#)). Furthermore, [Lindegren et al. \(2021b\)](#) (L21) proposed two offset functions $Z_5(G, \nu_{\text{eff}}, \beta)$ and $Z_6(G, \hat{\nu}_{\text{eff}}, \beta)$ applicable to 5- and 6-parameter solutions (`astrometric_params_solved` = 31 and 95), respectively, that give an estimate of the systematics in the parallax measurement as a function of the magnitude in the G -band, the effective wavenumber or astrometrically-estimated effective wavenumber (also known as pseudo-colour), and ecliptic latitude. Their zero-point correction model is based on quasars, and complemented with indirect methods involving physical binaries and stars in the Large Magellanic Cloud. The bias function Z_5 or Z_6 should be *subtracted* from the value (`parallax`) given in the archive. Python im-

plementations of both functions are available in the *Gaia* web pages ⁷.

Despite the availability of such a correction, which will in general reduce systematics in the parallaxes, [Lindegren et al. \(2021b\)](#) still encourages users of *Gaia* EDR3 data to derive their own zero-point estimates, whenever possible, and to keep a critical eye on the relevance of the correction for specific use cases. Hence, as for *Gaia* DR2, a lot of studies have already been comparing parallaxes from EDR3 and from independent measurements. [Riess et al. \(2021\)](#) inferred an offset of $-14 \pm 5 \mu\text{as}$, such that corrected *Gaia* parallaxes are larger than Cepheid photometric parallaxes, using a sample of classical Cepheids ($G \lesssim 11$, $1.35 \mu\text{m}^{-1} \lesssim \nu_{\text{eff}} \lesssim 1.6 \mu\text{m}^{-1}$). Based on a sample of blue RR Lyrae stars ($\nu_{\text{eff}} > 1.5 \mu\text{m}^{-1}$), [Bhardwaj et al. \(2021\)](#) found an offset with corrected *Gaia* parallaxes of $-25 \pm 5 \mu\text{as}$ in the same direction. [Stassun & Torres \(2021\)](#) showed that no statistically significant parallax residuals remain after correction according to the *Gaia* parallax zero-point correction model ($+15 \pm 18 \mu\text{as}$), using 76 bright, blue eclipsing binaries ($5 \lesssim G \lesssim 12$, $\nu_{\text{eff}} > 1.5 \mu\text{m}^{-1}$). Moreover, an analysis using photometric parallaxes of red clump stars in LAMOST indicated a median offset of $\sim -26 \mu\text{as}$, that is largely reduced after application of the zero-point correction model although variations of the order of $10 \mu\text{as}$ persist depending on the position in the sky ([Huang et al., 2021](#)). [Ren et al. \(2021\)](#) derived offsets of $-28.6 \pm 0.6 \mu\text{as}$ and $4.2 \pm 0.5 \mu\text{as}$ before and after correction respectively, based on $\sim 110\,000$ W Ursae Majoris(EW)-type eclipsing binary systems. Finally, using a sample of over 2000 first-ascent RGB stars with asteroseismic parallaxes in the *Kepler* field ($9 \lesssim G \lesssim 13$, $1.4 \mu\text{m}^{-1} \lesssim \nu_{\text{eff}} \lesssim 1.5 \mu\text{m}^{-1}$), [Zimm \(2021\)](#) found an over-correction for $G \lesssim 10.8$ such that Z_5 -corrected EDR3 parallaxes are larger than asteroseismic ones by $15 \pm 3 \mu\text{as}$; while, for $G \gtrsim 10.8$, EDR3 and asteroseismic parallaxes agree up to a constant consistent with expected spatial variations in *Gaia* after a linear, colour-dependent adjustment.

We revisit the *Gaia* EDR3 parallax zero-point using asteroseismic data in the

⁷<https://www.cosmos.esa.int/web/gaia/edr3-code>

Kepler (Sec. 5.2.3), *K2* (Sec. 5.2.4), and TESS fields (Sec. 5.2.5). Since the methods are the same as those used in Khan et al. (2019) (Sec. 5.1), they are not detailed here. Furthermore, based on the conclusions of this study, we only focus our interest on asteroseismic parallaxes estimated with PARAM. Sec. 5.2.6 presents a summary of our analysis in each field, and includes independent validations based on quasars, the magnitude of the red clump, and synthetic populations from TRILEGAL.

5.2.2 Observational Framework

Our sample is divided into three main parts. We first have first-ascent red-giant branch stars and red clump stars observed by *Kepler* and with APOGEE DR14 spectra (Abolfathi et al., 2018). These stars have information available about their evolutionary state, which was determined using the approach defined in Elsworth et al. (2019), hence we can distinguish RGB from RC stars. Both asteroseismic, i.e. ν_{\max} and $\langle \Delta\nu \rangle$ (from Mosser et al. 2011a and Yu et al. (2018), respectively), and classical constraints, i.e. T_{eff} , $\log g$, $[\text{Fe}/\text{H}]$ and $[\alpha/\text{Fe}]$, are considered. The *Kepler* subsample is finally made of ~ 3200 RGB stars and 2300 RC stars.

The second part of our sample contains red giants observed by *K2*, namely *Kepler*'s follow-up mission. Compared to the two campaigns analysed in our previous study (Khan et al., 2019), we now have data available for 17 campaigns: C01-C08, C10-18. In its campaign 9, *K2* observed dense regions towards the Galactic bulge in order to constrain the microlensing parallaxes and probe for free-floating planets, while campaign 19 observed nearby planet systems (including TRAPPIST-1) - hence, these two campaigns were not considered for our analysis. Both asteroseismic constraints from Mosser et al. (2011a) and from Elsworth et al. (2019) are considered, and will be compared throughout the study. Three choices are available for T_{eff} and $[\text{Fe}/\text{H}]$: spectroscopic estimates from APOGEE DR16 (Ahumada et al., 2020); from GALAH DR3 (Buder et al., 2021); or photometric estimates from SkyMapper (Casagrande et al., 2019). In total, there are nearly 2600, 6000, and 7000 red-giant

stars (RGB and RC) respectively with asteroseismology in each survey. Because *K2* data is noisier than *Kepler*, we used comparisons among pipelines to define a high-quality sample (similar as what was done in [Rendle et al., 2019b](#)).

Lastly, our sample is complemented with very bright ($G < 11$) red-giant stars in the TESS southern continuous viewing zone (TESS-SCVZ), based on the first year of TESS data. Asteroseismic properties were extracted in [Mackereth et al. \(2021\)](#) for these stars. Constraints on the photospheric chemical compositions are available from APOGEE DR16 ([Ahumada et al., 2020](#)) and SkyMapper ([Casagrande et al., 2019](#)), which then leaves us with subsamples of 150 and 1800 red giants respectively, only keeping stars for which ν_{\max} and $\langle \Delta\nu \rangle$ are consistent within 3σ across all pipelines considered in [Mackereth et al. \(2021\)](#).

5.2.3 Analysis of the *Kepler* field

We start our analysis with the *Kepler* field. We study trends of the parallax difference $\varpi_{\text{EDR3}} - \varpi_{\text{PARAM}}$ as a function of the ecliptic latitude, the G magnitude, the effective wavenumber, the frequency of maximum oscillation, the mass inferred from PARAM, and the metallicity (see top panel of Fig. 5.18 for the case of 5-parameter solutions). Most trends are fairly flat, except for the G magnitude which displays a curvy feature. This relation with G is expected (see Fig. 17 in [Fabricius et al. 2021](#)), and removed if we apply the zero-point correction (Fig. 5.18, bottom panel).

Without correcting *Gaia* parallaxes, *Kepler* shows a parallax offset of $\sim -30 \mu\text{as}$, in the sense that *Gaia* parallaxes are too small. After applying the correction, this is reduced to $\sim -10 \mu\text{as}$. These values remain unchanged when considering RGB and RC stars separately, or when selecting the 6-parameter solutions only.

5.2.4 Analysis of the *K2* fields

For the *K2* fields, six different combinations are considered depending on the asteroseismic constraints (Mosser or Elsworth) and the spectroscopic survey (APOGEE, GALAH, or SkyMapper). We look again at the trends with the different param-

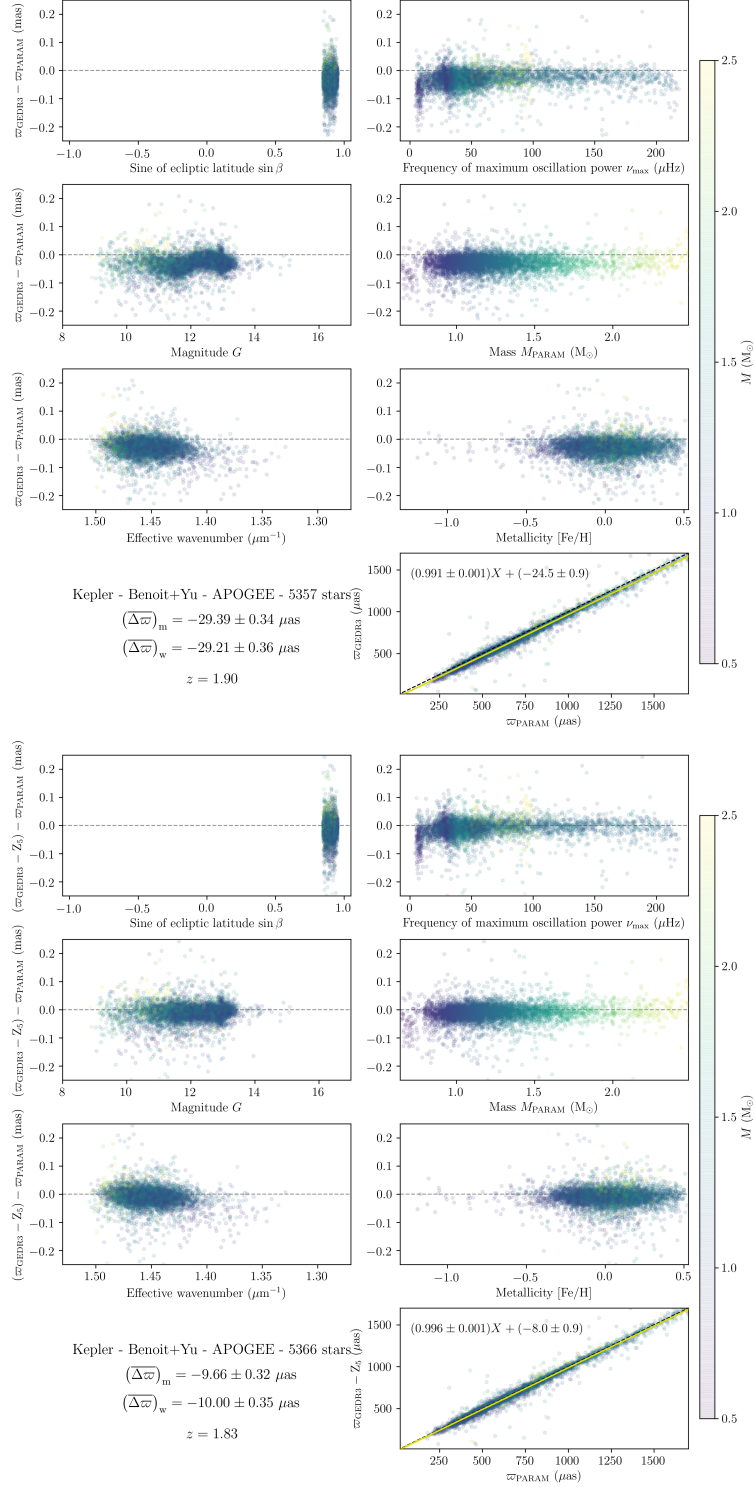


Figure 5.18: Trends of the parallax difference $\varpi_{\text{EDR3}} - \varpi_{\text{PARAM}}$ with the ecliptic latitude, the G magnitude, the effective wavenumber, the frequency of maximum oscillation, the mass inferred from PARAM, and the metallicity, without (top panel) and with the inclusion of the zero-point correction (bottom panel). The colour scale indicates the mass from PARAM.

eters. For a good number of these fields (and independently of the spectroscopy), we observe a fairly strong trend of the parallax difference with the stellar mass. This trend remains, even if we use raw scaling relations to compute the mass and the asteroseismic parallax, instead of PARAM. We suspect that this trend with mass could be related to, e.g., different noise levels in the various *K2* campaigns but, as of now, this is still being investigated by Mosser and Elsworth. We also note that there is a larger scatter for bright stars, i.e. $G < 13$.

The offsets measured for the different datasets span a range between -60 and $20 \mu\text{as}$, if we ignore very uncertain estimates (e.g. C15 in Mosser+APOGEE). If we include the L21 correction, it over-corrects the parallax difference most of the time and results in positive offsets that can go as large as $40 \mu\text{as}$. This is evidence that the [Lindegren et al. \(2021b\)](#) is not universally suited for different types of sources, spanning a wide range of positions, magnitudes, and colours. Furthermore, it is not possible to estimate these offsets for the 6-parameter solutions samples as these have too few stars.

5.2.5 Analysis of the TESS-SCVZ field

Two datasets are available for TESS, one with APOGEE and another one with SkyMapper. They do not show any specific trends with the different parameters considered (see Fig. 5.19). However, they suggest offsets that are quite different: $\sim -30 \mu\text{as}$ for APOGEE, and -1 (weighted mean) or $-18 \mu\text{as}$ (median) for SkyMapper. Including the L21 correction increases these values by $5-10 \mu\text{as}$, which seems to slightly improve the agreement with *Gaia*. Results based on 6-parameter solutions suggest similar offsets as the above.

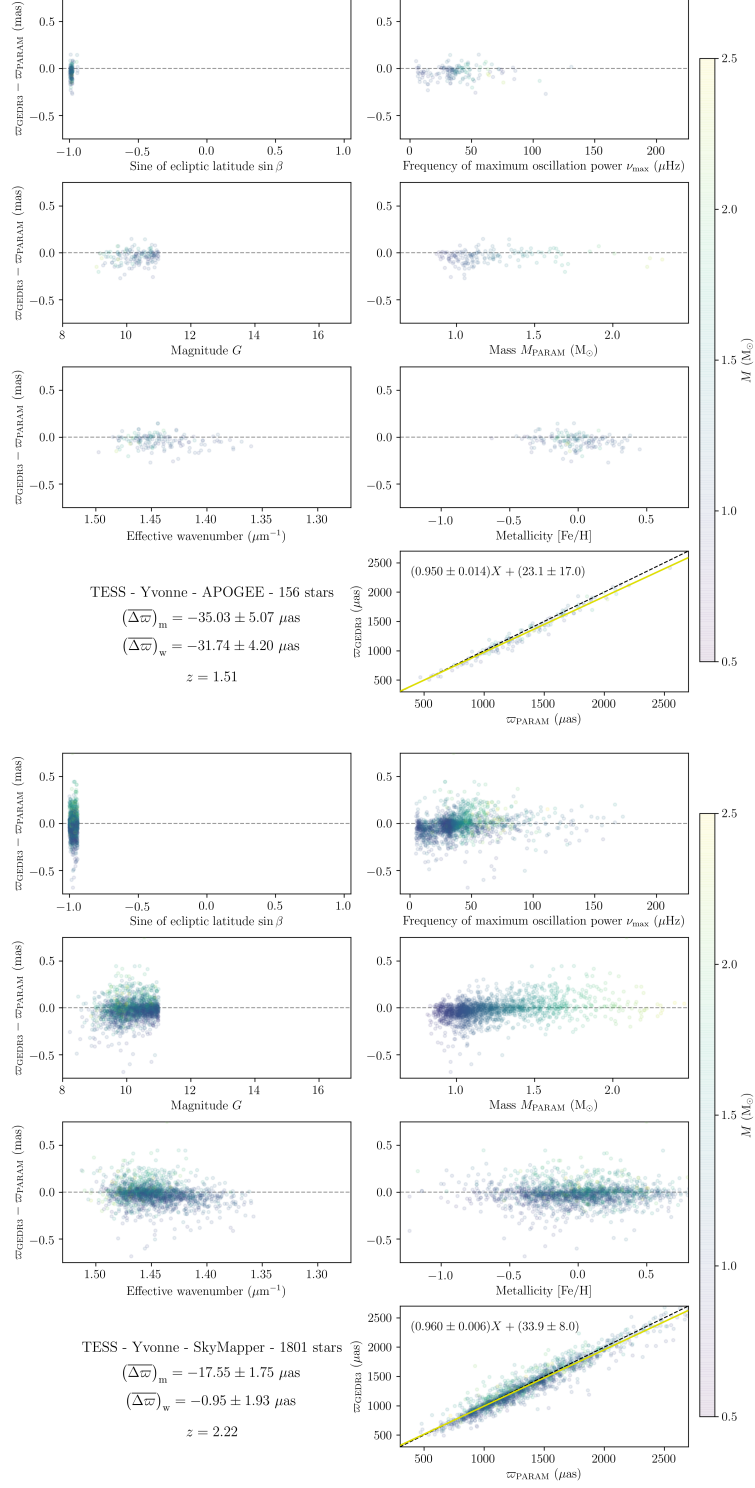


Figure 5.19: Trends of the parallax difference $\varpi_{\text{EDR3}} - \varpi_{\text{PARAM}}$ with the ecliptic latitude, the G magnitude, the effective wavenumber, the frequency of maximum oscillation, the mass inferred from PARAM, and the metallicity, using APOGEE (top panel) or SkyMapper constraints (bottom panel). The colour scale indicates the mass from PARAM.

5.2.6 A Global Picture of the *Gaia* EDR3 Parallax Zero-Point

Parallax Offsets

In the top panel of Fig. 5.20, we put together our offsets estimate from our different asteroseismic samples, as well as the values suggested by [Lindgren et al. \(2021b\)](#) and quasars. For *Kepler* and TESS, the zero-points obtained using APOGEE spectroscopic constraints are shown, while for *K2* we show all available offsets (four or six estimates, depending on whether SkyMapper has observed the field) to have an idea of possible sample biases. For [Lindgren et al. \(2021b\)](#), we compute the median offset based on the full sample with asteroseismic constraints (not dependent on the availability of spectroscopy). And finally, we select quasars in a radius of 7° (*Kepler/K2*) or 12° (TESS) around the central coordinates of each field, applying a couple of *Gaia* flags to remove spurious sources (`ruwe` < 1.4 , `ipd_frac_multi_peak` ≤ 2 , and `ipd_gof_harmonic_amplitude` < 0.1). This removes many sources near the galactic plane, where quasar properties become less reliable.

First of all, we note that our measured offsets from asteroseismology are in very good agreement with the zero-point correction model and quasars. Differences are only in the order of a few tens of μas , which is already quite spectacular and highlights the progress that is made possible through the analysis of solar-like oscillators. Furthermore, Fig. 5.20 (top panel) illustrates a clear trend of the parallax offset with the galactic latitude, whereby fields near the galactic plane ($\sin \beta \sim 0$) have a more negative offset.

Magnitude of the Red Clump

As a way to validate our findings, we also analysed the information provided by the magnitude of the red clump. In the bottom panel of Fig. 5.20, we show the absolute magnitude of the clump as suggested by our asteroseismic samples, a selection of *Gaia* EDR3 sources in each field, and TRILEGAL simulations. For the

asteroseismic datasets, we use the K -band absolute magnitude computed by PARAM. Then, we select *Gaia* EDR3 sources centred around the central coordinates of each field and with $1 < G < 15$, which provides us with a sample that is independent of asteroseismology (see Fig. 5.22). At last, we simulate synthetic populations that are representative of K2 fields, using TRILEGAL (Girardi et al., 2005).

For each dataset, we compute the mode of the magnitude of the red clump using a Kernel Density Estimation (KDE) with a fixed bandwidth (equal to 0.1) on the corresponding histogram. With regards to the *Gaia* EDR3 sample, two different estimates are given, depending on whether we include or not the L21 correction to the inverted *Gaia* raw parallaxes, and extinctions are calculated with the combined map (Marshall et al., 2006; Green et al., 2019; Drimmel et al., 2003) from `mw dust`⁸ (Bovy et al., 2016).

The trend with the galactic latitude observed for parallax offsets is also present for the magnitude of the red clump (see Fig. 5.20, bottom panel). Near the galactic plane ($\sin \beta \sim 0$), the red clump becomes brighter as one would expect from a negative parallax offset. The relation with galactic latitude is essentially reproduced by the seismic samples, the *Gaia* EDR3 sample without the L21 parallax correction, and the TRILEGAL simulations. The only case where it is not followed is that of the *Gaia* EDR3 sample including the correction, which again supports the idea that the Lindegren et al. (2021b) zero-point model is not suited to every kind of stars (see also Sec. 5.2.4).

5.2.7 Conclusions

We carried out a follow-up of our 2019 study (Khan et al., 2019) to investigate the *Gaia* EDR3 parallax zero-point, for a significantly larger number of asteroseismic fields: *Kepler*, 17 *K2* campaigns, and TESS-SCVZ.

First, we are able to nicely illustrate the positional dependence of the *Gaia* parallax zero-point: *Kepler* suggests an offset of $\sim -30 \mu\text{as}$, *K2* campaigns span

⁸<https://github.com/jobovy/mwdust>

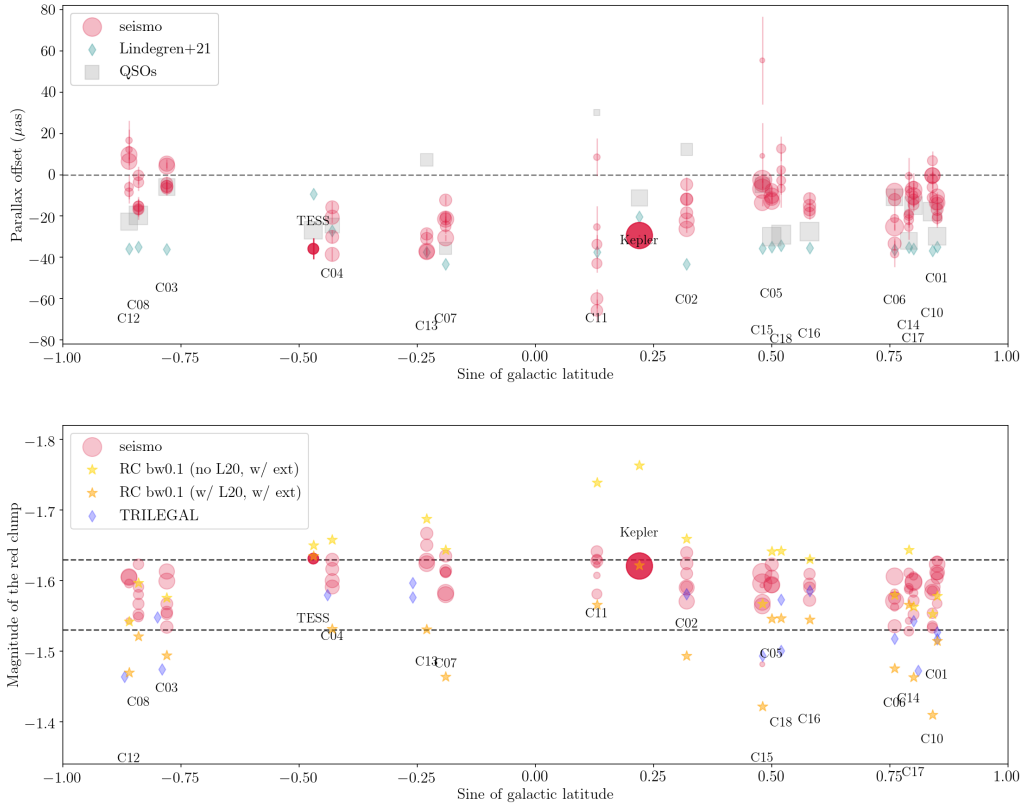


Figure 5.20: Top panel: Parallax offsets as estimated from asteroseismology (red circles), the [Lindegren et al. \(2021b\)](#) zero-point correction model (green diamonds), and quasars in each field (grey squares), as a function of the sine of the galactic latitude. Bottom panel: K -magnitude of the red clump as estimated from asteroseismic samples (red circles), *Gaia* EDR3 samples without (yellow stars) and with the L21 correction (orange stars), and TRILEGAL synthetic populations (purple diamonds), as a function of the sine of the galactic latitude. The black dashed lines show the expected range of values for the magnitude of the clump in the K band. A larger circle (square) size indicates a greater number of stars in the asteroseismic (quasars) samples.

K2C15

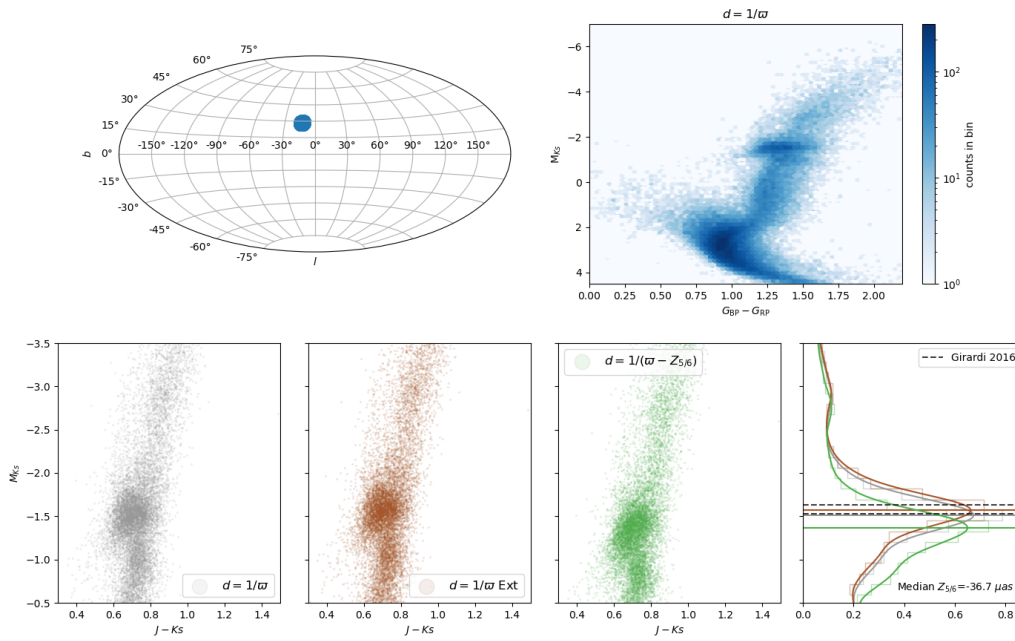


Figure 5.21: Top left: Sky map showing the location of the C15 field. Top right: CMD with the colour scale showing the density of stars. Bottom: Three different CMDs with the absolute magnitude calculated: by inverting the raw *Gaia* parallax (left), and adding the extinction (middle), or by applying the L21 correction (right); and the corresponding histograms and KDEs. The brown and green lines show the modes that are taken as references for the magnitude of the clump. The black dashed lines indicate the range of magnitudes that is expected from models.

a wide range between ~ -60 and $+20 \mu\text{as}$ depending on the field location and the combination of asteroseismic and spectroscopic constraints used, and TESS shows an offset that is similar to *Kepler*'s if also using APOGEE parameters. For *Kepler* and TESS, similar offsets are found for both 5- and 6-parameter solutions; however, we are unable to confirm this for the *K2* fields as the 6-parameter solutions samples are too small.

The inclusion of the [Lindegren et al. \(2021b\)](#) zero-point estimates slightly improves the agreement between *Gaia* and asteroseismology in the case of *Kepler* and TESS. However, in most *K2* fields, it can significantly over-correct the parallax difference, sometimes resulting in large positive parallax offsets. This underlines the importance of estimating the *Gaia* EDR3 parallax zero-point independently of this correction model, which is based on quasars, physical binaries and stars in the Large Magellanic Cloud.

Lastly, by compiling our results obtained with the different fields, we show that the asteroseismic offsets are in very reasonable agreement with estimates suggested by [Lindegren et al. \(2021b\)](#) and quasars. We also demonstrate the dependence of the *Gaia* parallax offset with the galactic latitude, whereby fields located near the galactic plane display a more negative offset estimation. Moreover, we undertake an external validation analysis that focuses instead on the magnitude of the red clump, and find a similar trend with the galactic latitude (except when applying the L21 correction).

All of these demonstrate the high potential of asteroseismology to constrain biases in the *Gaia* parallaxes but also, to a larger extent, to study the distance scale that has important implications for, e.g., the Hubble constant. More related to my PhD research would be the possibility to study the red-giant branch bump, using *Gaia* EDR3 distances. In that respect, Fig. 5.22 shows the Hertzsprung-Russell Diagrams obtained for the *Kepler* field, when using distances from *Gaia* DR2, EDR3, or asteroseismology (PARAM). This illustrates the significant improvement between

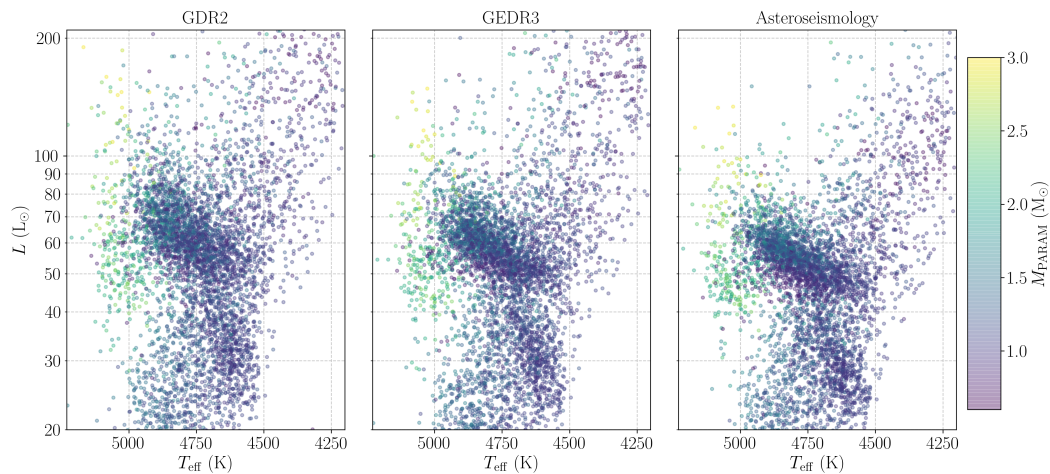


Figure 5.22: Hertzsprung-Russell Diagrams of red-giant stars in the *Kepler* field, using distance estimates from *Gaia* DR2 (left panel), *Gaia* EDR3 (middle panel), and PARAM (right panel). The colour scale indicates the mass as inferred from PARAM.

the second and early third data releases of *Gaia*: features such as the red-giant branch bump and red clump are more nicely defined in EDR3. The addition of many *K2* fields should prove to be extremely exciting for further analyses of the bump, and working towards improved descriptions of convective boundary mixing in stellar evolution models (as discussed in Chap. 4).

Chapter 6

Conclusions and Future Prospects

In this thesis, we worked towards the objective of improving the physical picture of convective boundary mixing processes below the envelopes of red-giant stars.

Novel constraints on the luminosity bump as a diagnostic for extra-mixing processes were achievable thanks to the study of stellar oscillations. In Chap. 4, we revisited the red-giant branch bump by combining asteroseismic and spectroscopic constraints from *Kepler* and APOGEE. This allowed us to confirm expected trends from theory, namely that the red-giant branch bump becomes brighter with increasing mass and decreasing metallicity. Most importantly, our envelope overshooting calibration indicates that: for low-mass stars ($M \leq 1.3 M_{\odot}$), the extra-mixing efficiency increases as the metallicity decreases. As this result had potential to improve the physical background behind envelope overshooting, we extended our analysis to clusters in our Galaxy and in the Magellanic Clouds observed by the Hubble Space Telescope. Preliminary comparisons between Galactic globular clusters and best-fitting isochrones also seem to support the idea whereby a higher overshooting efficiency is required to reproduce the magnitude of the bump in the most metal-poor clusters. Future analyses with the inclusion of Magellanic Clouds clusters and more detailed synthetic populations simulated with TRILEGAL will give us the opportunity to strengthen these preliminary findings. Moreover, a different overshooting efficiency could be related to a change in the stiffness of the convective boundary:

this could be a major step forward and mean that we are really testing convection, as a physical process.

Studies of stellar evolution theory, such as that of the bump, rely on the precision and accuracy of asteroseismic constraints that are used. Since asteroseismic masses and radii are correlated, it is of utmost importance to check their reliability through comparisons with independent measurements. With distances being available for over 1.4 billion sources, the *Gaia* mission offers very rich datasets to do this. Hence, in Chap. 5, we compared distances from asteroseismology and *Gaia* DR2, and later EDR3, in the *Kepler*, *K2*, and TESS-SCVZ fields, to constrain biases both in the asteroseismic and the astrometric sides. These works both prove the strong potential of asteroseismology to estimate distances (hence radii), as the offsets measured with respect to *Gaia* are in the order of a few tens of μas , and provide an illustration of the positional dependence of the *Gaia* parallax zero-point, thanks to the many asteroseismic fields located in different parts of the sky.

Future Prospects

The continuation of the analysis of the red-giant branch bump in star clusters, expanding our calibration to lower metallicities and younger ages, should give us hints about not only the efficiency but also the physical nature of additional mixing processes occurring along the red-giant branch. Based on the results provided by field stars and clusters, we should be able to implement and test advanced mixing parameterisations that have been inspired from 2D and 3D hydrodynamical simulations. Linking the observed trends of the extra-mixing (e.g. with metallicity) with parameters constituting the various mixing coefficients is the way forward to providing a stronger physical foundation to the large concept that is convective overshooting.

An independent way to constrain the envelope overshooting efficiency and mixing timescale would be to use asteroseismic diagnostics provided by individual oscillation frequencies: buoyancy glitches. Mixed modes are sensitive to the central radiative structure, and can thus provide information on the properties of the chem-

ical composition gradient inside the star (see, e.g., [Montalbán et al., 2013](#)). The presence of mixed modes significantly modifies the oscillation spectrum, compared to less evolved stars on the main sequence (e.g. [Mosser, 2015](#)). One could look at the oscillation spectra of stars close to the bump, and search for any complementary seismic signature that could arise from the chemical discontinuity. Fitting individual mixed modes might be challenging for stars as luminous as the bump, but the situation is potentially better for low-mass, metal-rich stars (e.g. in cluster NGC 6791). Besides, to aid in interpreting the observed oscillation spectra, one can also simultaneously analyse the evolution of a theoretical oscillation spectrum along the luminosity bump.

As demonstrated by our analyses based on *Gaia* DR2 and EDR3 data, asteroseismology provides an excellent means to estimate stellar distances and contribute to the calibration of the *Gaia* parallax zero-point, that keep evolving with the data releases. Hence, it is crucial to continue our efforts in this direction, and to provide updated investigations of the offset with the future *Gaia* data releases. With a proper characterisation of the offset, and as it gets smaller with more recent releases, a new study of the red-giant branch bump based on *Gaia* distances is also foreseen.

Bibliography

- Abolfathi B., et al., 2018, [ApJS](#), **235**, 42
- Aerts C., Christensen-Dalsgaard J., Kurtz D. W., 2010, *Asteroseismology*. Springer Netherlands
- Ahumada R., et al., 2020, [ApJS](#), **249**, 3
- Albareti F. D., et al., 2017, [ApJS](#), **233**, 25
- Alongi M., Bertelli G., Bressan A., Chiosi C., 1991, *A&A*, **244**, 95
- Arenou F., et al., 2018, [A&A](#), **616**, A17
- Arnett W. D., Meakin C., Viallet M., Campbell S. W., Lattanzio J. C., Mocák M., 2015, [ApJ](#), **809**, 30
- Asplund M., Grevesse N., Sauval A. J., Scott P., 2009, [ARA&A](#), **47**, 481
- Asplund M., Amarsi A. M., Grevesse N., 2021, arXiv e-prints, p. [arXiv:2105.01661](#)
- Baglin A., Auvergne M., Barge P., Deleuil M., Michel E., CoRoT Exoplanet Science Team 2009, in Pont F., Sasselov D., Holman M. J., eds, Vol. 253, *Transiting Planets*. pp 71–81, [doi:10.1017/S1743921308026252](#)
- Baraffe I., Pratt J., Goffrey T., Constantino T., Folini D., Popov M. V., Walder R., Viallet M., 2017, [ApJ](#), **845**, L6
- Basu S., Chaplin W. J., Elsworth Y., 2010, [ApJ](#), **710**, 1596
- Batalha N. M., et al., 2011, [ApJ](#), **729**, 27
- Baumgardt H., 2017, [MNRAS](#), **464**, 2174
- Baumgardt H., Hilker M., 2018, [MNRAS](#), **478**, 1520
- Beck P. G., et al., 2011, [Science](#), **332**, 205
- Bedding T. R., 2014, *Solar-like oscillations: An observational perspective*. p. 60
- Bedding T. R., et al., 2011, [Nature](#), **471**, 608
- Belkacem K., 2012, in Boissier S., de Laverny P., Nardetto N., Samadi R., Valls-Gabaud D., Wozniak H., eds, *SF2A-2012: Proceedings of the Annual meeting of the French Society of Astronomy and Astrophysics*. pp 173–188 ([arXiv:1210.3505](#))

- Belkacem K., Samadi R., Goupil M. J., Dupret M. A., Brun A. S., Baudin F., 2009, [A&A](#), 494, 191
- Belkacem K., Goupil M. J., Dupret M. A., Samadi R., Baudin F., Noels A., Mosser B., 2011, [A&A](#), 530, A142
- Belkacem K., Dupret M. A., Baudin F., Appourchaux T., Marques J. P., Samadi R., 2012, [A&A](#), 540, L7
- Belkacem K., Samadi R., Mosser B., Goupil M.-J., Ludwig H.-G., 2013, in Shibahashi H., Lynas-Gray A. E., eds, *Astronomical Society of the Pacific Conference Series Vol. 479, Progress in Physics of the Sun and Stars: A New Era in Helio- and Asteroseismology*. p. 61 ([arXiv:1307.3132](#))
- Bergbusch P. A., Vandenberg D. A., 2001, [ApJ](#), 556, 322
- Bhardwaj A., et al., 2021, [ApJ](#), 909, 200
- Bjork S. R., Chaboyer B., 2006, [ApJ](#), 641, 1102
- Böhm-Vitense E., 1958, [ZAp](#), 46, 108
- Bono G., Castellani V., 1992, [A&A](#), 258, 385
- Bono G., Cassisi S., Zoccali M., Piotto G., 2001, [ApJ](#), 546, L109
- Borucki W. J., et al., 2010, [Science](#), 327, 977
- Bovy J., Rix H.-W., Green G. M., Schlafly E. F., Finkbeiner D. P., 2016, [ApJ](#), 818, 130
- Bressan A. G., Chiosi C., Bertelli G., 1981, [A&A](#), 102, 25
- Bressan A., Marigo P., Girardi L., Salasnich B., Dal Cero C., Rubele S., Nanni A., 2012, [MNRAS](#), 427, 127
- Bressan A., Girardi L., Marigo P., Rosenfield P., Tang J., 2015, in *Asteroseismology of Stellar Populations in the Milky Way*. p. 25 ([arXiv:1409.2268](#)), [doi:10.1007/978-3-319-10993-0_3](#)
- Brogaard K., Bruntt H., Grundahl F., Clausen J. V., Frandsen S., Vandenberg D. A., Bedin L. R., 2011, [A&A](#), 525, A2
- Brogaard K., et al., 2012, [A&A](#), 543, A106
- Brogaard K., et al., 2016, [Astronomische Nachrichten](#), 337, 793
- Brogaard K., et al., 2018, [MNRAS](#), 476, 3729
- Brown A. G. A., 2021, arXiv e-prints, p. [arXiv:2102.11712](#)
- Brown T. M., Gilliland R. L., Noyes R. W., Ramsey L. W., 1991, [ApJ](#), 368, 599
- Buder S., et al., 2021, [MNRAS](#),
- Cabrera-Ziri I., et al., 2020, [MNRAS](#), 495, 375

Cantat-Gaudin T., et al., 2018, [A&A](#), **618**, [A93](#)

Carretta E., Bragaglia A., Gratton R., D’Orazi V., Lucatello S., 2009, [A&A](#), **508**, [695](#)

Carretta E., Bragaglia A., Gratton R. G., Recio-Blanco A., Lucatello S., D’Orazi V., Cassisi S., 2010, [A&A](#), **516**, [A55](#)

Casagrande L., VandenBerg D. A., 2018a, [MNRAS](#), **475**, [5023](#)

Casagrande L., VandenBerg D. A., 2018b, [MNRAS](#), **479**, [L102](#)

Casagrande L., et al., 2014, [MNRAS](#), **439**, [2060](#)

Casagrande L., Wolf C., Mackey A. D., Nordlander T., Yong D., Bessell M., 2019, [MNRAS](#), **482**, [2770](#)

Cassisi S., Salaris M., 1997, [MNRAS](#), **285**, [593](#)

Cassisi S., degl’Innocenti S., Salaris M., 1997, [MNRAS](#), **290**, [515](#)

Cassisi S., Salaris M., Bono G., 2002, [ApJ](#), **565**, [1231](#)

Cassisi S., Marín-Franch A., Salaris M., Aparicio A., Monelli M., Pietrinferni A., 2011, [A&A](#), **527**, [A59](#)

Castellani V., Giannone P., Renzini A., 1971, [Ap&SS](#), **10**, [340](#)

Cenadelli D., 2010, *Archive for History of Exact Sciences*, **64**, [203](#)

Chaplin W. J., Miglio A., 2013, [ARA&A](#), **51**, [353](#)

Chaplin W. J., et al., 2010, [ApJ](#), **713**, [L169](#)

Chen Y. Q., Casagrande L., Zhao G., Bovy J., Silva Aguirre V., Zhao J. K., Jia Y. P., 2017, [ApJ](#), **840**, [77](#)

Christensen-Dalsgaard J., 2002, [Reviews of Modern Physics](#), **74**, [1073](#)

Christensen-Dalsgaard J., 2015, [MNRAS](#), **453**, [666](#)

Christensen-Dalsgaard J., Monteiro M. J. P. F. G., Rempel M., Thompson M. J., 2011, [MNRAS](#), **414**, [1158](#)

Christensen-Dalsgaard J., et al., 2020, [A&A](#), **635**, [A165](#)

Cristini A., Meakin C., Hirschi R., Arnett D., Georgy C., Viallet M., 2016, *Physica Scripta*, **91**, [034006](#)

Cristini A., Hirschi R., Meakin C., Arnett D., Georgy C., Walkington I., 2019, [MNRAS](#), **484**, [4645](#)

Davies G. R., Miglio A., 2016, [Astronomische Nachrichten](#), **337**, [774](#)

Davies G. R., et al., 2016, [MNRAS](#), **456**, [2183](#)

Davies G. R., et al., 2017, [A&A](#), **598**, [L4](#)

De Ridder J., Molenberghs G., Eyer L., Aerts C., 2016, [A&A](#), **595**, L3

Deheuvels S., et al., 2010, [A&A](#), **515**, A87

Demarque P., Woo J.-H., Kim Y.-C., Yi S. K., 2004, [The Astrophysical Journal Supplement Series](#), **155**, 667

Di Cecco A., et al., 2010, [ApJ](#), **712**, 527

Dirsch B., Richtler T., Gieren W. P., Hilker M., 2000, [A&A](#), **360**, 133

Dotter A., Chaboyer B., Jevremović D., Kostov V., Baron E., Ferguson J. W., 2008, [The Astrophysical Journal Supplement Series](#), **178**, 89

Drimmel R., Cabrera-Lavers A., López-Corredoira M., 2003, [A&A](#), **409**, 205

Elsworth Y., Hekker S., Basu S., Davies G. R., 2017, [MNRAS](#), **466**, 3344

Elsworth Y., et al., 2019, [MNRAS](#), **489**, 4641

Fabricius C., et al., 2021, [A&A](#), **649**, A5

Fagotto F., Bressan A., Bertelli G., Chiosi C., 1994, [A&AS](#), **104**, 365

Farmer R., Kolb U., Norton A. J., 2013, [MNRAS](#), **433**, 1133

Ferraro F. R., Messineo M., Fusi Pecci F., de Palo M. A., Straniero O., Chieffi A., Limongi M., 1999, [AJ](#), **118**, 1738

Fischler M. A., Bolles R. C., 1981, [Commun. ACM](#), **24**, 381

Foreman-Mackey D., Hogg D. W., Lang D., Goodman J., 2013, [Publications of the Astronomical Society of the Pacific](#), **125**, 306

Freytag B., Ludwig H.-G., Steffen M., 1996, [A&A](#), **313**, 497

Fu X., Bressan A., Marigo P., Girardi L., Montalbán J., Chen Y., Nanni A., 2018, [MNRAS](#), **476**, 496

Fusi Pecci F., Ferraro F. R., Crocker D. A., Rood R. T., Buonanno R., 1990, [A&A](#), **238**, 95

Gabriel A. H., et al., 1995, [Sol. Phys.](#), **162**, 61

Gabriel M., Noels A., Montalbán J., Miglio A., 2014, [A&A](#), **569**, A63

Gai N., Basu S., Chaplin W. J., Elsworth Y., 2011, [ApJ](#), **730**, 63

Gaia Collaboration et al., 2016a, [A&A](#), **595**, A1

Gaia Collaboration et al., 2016b, [A&A](#), **595**, A2

Gaia Collaboration et al., 2018, [A&A](#), **616**, A1

Gaia Collaboration et al., 2021, [A&A](#), **649**, A1

García R. A., Ballot J., 2019, [Living Reviews in Solar Physics](#), **16**, 4

Gaulme P., et al., 2016, [ApJ](#), **832**, 121

Gingerich O., 1995, in van der Kruit P. C., Gilmore G., eds, Vol. 164, *Stellar Populations*. p. 3

Girardi L., 2016, [Annual Review of Astronomy and Astrophysics](#), **54**, 95

Girardi L., Bertelli G., Bressan A., Chiosi C., Groenewegen M. A. T., Marigo P., Salasnich B., Weiss A., 2002, [A&A](#), **391**, 195

Girardi L., Groenewegen M. A. T., Hatziminaoglou E., da Costa L., 2005, [A&A](#), **436**, 895

Green G. M., et al., 2015, [ApJ](#), **810**, 25

Green G. M., Schlafly E., Zucker C., Speagle J. S., Finkbeiner D., 2019, [ApJ](#), **887**, 93

Guggenberger E., Hekker S., Basu S., Bellinger E., 2016, [MNRAS](#), **460**, 4277

Hall O. J., et al., 2019, [MNRAS](#), **486**, 3569

Handberg R., Brogaard K., Miglio A., Bossini D., Elsworth Y., Slumstrup D., Davies G. R., Chaplin W. J., 2017, [MNRAS](#), **472**, 979

Harris W. E., 1996, [AJ](#), **112**, 1487

Hawkins K., Leistedt B., Bovy J., Hogg D. W., 2017, [MNRAS](#), **471**, 722

Hekker S., Christensen-Dalsgaard J., 2017, [A&A Rev.](#), **25**, 1

Hekker S., et al., 2012, [A&A](#), **544**, A90

Hekker S., Angelou G. C., Elsworth Y., Basu S., 2020, [MNRAS](#), **492**, 5940

Herwig F., 2000, [A&A](#), **360**, 952

Hogg D. W., Bovy J., Lang D., 2010, preprint, ([arXiv:1008.4686](#))

Howell S. B., et al., 2014, [PASP](#), **126**, 398

Huang Y., Yuan H., Beers T. C., Zhang H., 2021, [ApJ](#), **910**, L5

Huber D., et al., 2012, [ApJ](#), **760**, 32

Huber D., et al., 2017, [ApJ](#), **844**, 102

Iben I., 1968, [Nature](#), **220**, 143

Jofré P., Weiss A., 2011, [A&A](#), **533**, A59

Joyce M., Chaboyer B., 2015, [ApJ](#), **814**, 142

Kallinger T., et al., 2010, [A&A](#), **522**, A1

Khan S., Hall O. J., Miglio A., Davies G. R., Mosser B., Girardi L., Montalbán J., 2018, [ApJ](#), **859**, 156

Khan S., et al., 2019, [A&A](#), **628**, [A35](#)

King C. R., Da Costa G. S., Demarque P., 1985, [ApJ](#), **299**, [674](#)

Kippenhahn R., Weigert A., 1990, *Stellar Structure and Evolution*

Kjeldsen H., Bedding T. R., 1995, [A&A](#), **293**, [87](#)

Kjeldsen H., Bedding T. R., Viskum M., Frandsen S., 1995, [AJ](#), **109**, [1313](#)

Kjeldsen H., et al., 2003, [AJ](#), **126**, [1483](#)

Lagarde N., et al., 2015, [A&A](#), **580**, [A141](#)

Lagioia E. P., et al., 2018, [MNRAS](#),

Lebreton Y., Goupil M. J., 2014, [A&A](#), **569**, [A21](#)

Lebreton Y., Montalbán J., Christensen-Dalsgaard J., Roxburgh I. W., Weiss A., 2008, [Ap&SS](#), **316**, [187](#)

Lindegren L., et al., 2016, [A&A](#), **595**, [A4](#)

Lindegren L., et al., 2018, [A&A](#), **616**, [A2](#)

Lindegren L., et al., 2021a, [A&A](#), **649**, [A2](#)

Lindegren L., et al., 2021b, [A&A](#), **649**, [A4](#)

Luri X., et al., 2018, [A&A](#), **616**, [A9](#)

Mackereth J. T., et al., 2021, [MNRAS](#), **502**, [1947](#)

Maeder A., 1975, [A&A](#), **40**, [303](#)

Magic Z., Weiss A., Asplund M., 2015, [A&A](#), **573**, [A89](#)

Majewski S. R., Zasowski G., Nidever D. L., 2011, [ApJ](#), **739**, [25](#)

Marigo P., Girardi L., 2007, [A&A](#), **469**, [239](#)

Marigo P., et al., 2017, [ApJ](#), **835**, [77](#)

Marshall D. J., Robin A. C., Reylé C., Schultheis M., Picaud S., 2006, [A&A](#), **453**, [635](#)

Meakin C. A., Arnett D., 2007, [ApJ](#), **667**, [448](#)

Meissner F., Weiss A., 2006, [A&A](#), **456**, [1085](#)

Miglio A., 2012, [Astrophysics and Space Science Proceedings](#), **26**, [11](#)

Miglio A., et al., 2010, [A&A](#), **520**, [L6](#)

Miglio A., Morel T., Barbieri M., Mosser B., Girardi L., Montalbán J., Valentini M., 2012a, in *European Physical Journal Web of Conferences*. p. 05012 ([arXiv:1111.4366](#)), [doi:10.1051/epjconf/20121905012](#)

- Miglio A., et al., 2012b, [MNRAS](#), **419**, 2077
- Miglio A., Chaplin W. J., Farmer R., Kolb U., Girardi L., Elsworth Y., Appourchaux T., Handberg R., 2014, [ApJ](#), **784**, L3
- Miglio A., et al., 2016, [MNRAS](#), **461**, 760
- Miglio A., et al., 2021, [A&A](#), **645**, A85
- Milone A. P., et al., 2012, [A&A](#), **540**, A16
- Montalbán J., Miglio A., Noels A., Scuflaire R., Ventura P., 2010, [ApJ](#), **721**, L182
- Montalbán J., Miglio A., Noels A., Dupret M.-A., Scuflaire R., Ventura P., 2013, [ApJ](#), **766**, 118
- Montalbán J., et al., 2021, [Nature Astronomy](#),
- Monteiro M. J. P. F. G., et al., 2006, in Fridlund M., Baglin A., Lochard J., Conroy L., eds, ESA Special Publication Vol. 1306, The CoRoT Mission Pre-Launch Status - Stellar Seismology and Planet Finding. p. 363 ([arXiv:astro-ph/0605685](#))
- Morel T., Miglio A., 2012, VizieR Online Data Catalog, **741**
- Mosser B., 2015, in EAS Publications Series. pp 3–110 ([arXiv:1509.08077](#)), [doi:10.1051/eas/1573002](#)
- Mosser B., et al., 2010, [A&A](#), **517**, A22
- Mosser B., et al., 2011a, [A&A](#), **525**, L9
- Mosser B., et al., 2011b, [A&A](#), **532**, A86
- Murphy S. J., Hey D., Van Reeth T., Bedding T. R., 2019, [MNRAS](#), **485**, 2380
- Nardiello D., et al., 2018, [MNRAS](#), **481**, 3382
- Nataf D. M., 2014, [MNRAS](#), **445**, 3839
- Nataf D. M., Gould A. P., Pinsonneault M. H., Udalski A., 2013, [ApJ](#), **766**, 77
- Paxton B., Bildsten L., Dotter A., Herwig F., Lesaffre P., Timmes F., 2011, [ApJS](#), **192**, 3
- Paxton B., et al., 2013, [ApJS](#), **208**, 4
- Paxton B., et al., 2015, [ApJS](#), **220**, 15
- Paxton B., et al., 2018, [ApJS](#), **234**, 34
- Piatti A. E., Bailin J., 2019, [AJ](#), **157**, 49
- Pietrinferni A., Cassisi S., Salaris M., Castelli F., 2004, [The Astrophysical Journal](#), **612**, 168
- Pinsonneault M. H., et al., 2014, [ApJS](#), **215**, 19

Pinsonneault M. H., et al., 2018, [ApJS](#), **239**, 32

Pratt J., et al., 2016, [A&A](#), **593**, A121

Pratt J., Baraffe I., Goffrey T., Constantino T., Viallet M., Popov M. V., Walder R., Folini D., 2017, [A&A](#), **604**, A125

Refsdal S., Weigert A., 1970, [A&A](#), **6**, 426

Reimers D., 1975, *Memoires of the Societe Royale des Sciences de Liege*, **8**, 369

Ren F., Chen X., Zhang H., de Grijs R., Deng L., Huang Y., 2021, [ApJ](#), **911**, L20

Rendle B. M., et al., 2019a, [MNRAS](#), **484**, 771

Rendle B. M., et al., 2019b, [MNRAS](#), **490**, 4465

Renzini A., 1987, [A&A](#), **188**, 49

Ricker G. R., et al., 2015, [Journal of Astronomical Telescopes, Instruments, and Systems](#), **1**, 014003

Riello M., et al., 2003, [A&A](#), **410**, 553

Riello M., et al., 2018, [A&A](#), **616**, A3

Riess A. G., et al., 2018, [ApJ](#), **861**, 126

Riess A. G., Casertano S., Yuan W., Bowers J. B., Macri L., Zinn J. C., Scolnic D., 2021, [ApJ](#), **908**, L6

Rodrigues T. S., et al., 2014, [MNRAS](#), **445**, 2758

Rodrigues T. S., et al., 2017, [MNRAS](#), **467**, 1433

Rubele S., Girardi L., Kozhurina-Platais V., Goudfrooij P., Kerber L., 2011, [MNRAS](#), **414**, 2204

Rubele S., Girardi L., Kozhurina-Platais V., Kerber L., Goudfrooij P., Bressan A., Marigo P., 2013, [MNRAS](#), **430**, 2774

Sahlholdt C. L., Silva Aguirre V., Casagrande L., Mosumgaard J. R., Bojsen-Hansen M., 2018, [MNRAS](#), **476**, 1931

Salaris M., Cassisi S., 2005, *Evolution of Stars and Stellar Populations*

Salaris M., Cassisi S., 2017, [Royal Society Open Science](#), **4**, 170192

Salaris M., Chieffi A., Straniero O., 1993, [ApJ](#), **414**, 580

Salaris M., Cassisi S., Weiss A., 2002, [PASP](#), **114**, 375

Salaris M., Pietrinferni A., Piersimoni A. M., Cassisi S., 2015, [A&A](#), **583**, A87

Salaris M., Cassisi S., Schiavon R. P., Pietrinferni A., 2018, [A&A](#), **612**, A68

Schönberg M., Chandrasekhar S., 1942, [ApJ](#), **96**, 161

Schwarzschild K., 1906, Nachrichten von der Königlichen Gesellschaft der Wissenschaften zu Göttingen. Math.-phys. Klasse, 195, p. 41-53, [195](#), 41

Scufflaire R., 1974, [A&A](#), **36**, 107

Sharma S., Stello D., Bland-Hawthorn J., Huber D., Bedding T. R., 2016, [ApJ](#), **822**, 15

Silva Aguirre V., et al., 2012, [ApJ](#), **757**, 99

Silva Aguirre V., et al., 2020, [A&A](#), **635**, A164

Skrutskie M. F., et al., 2006, [AJ](#), **131**, 1163

Staritsin E. I., 2013, [Astronomy Reports](#), **57**, 380

Staritsin E. I., 2014, [Astronomy Reports](#), **58**, 808

Stassun K. G., Torres G., 2018, [ApJ](#), **862**, 61

Stassun K. G., Torres G., 2021, [ApJ](#), **907**, L33

Stello D., et al., 2009, [ApJ](#), **700**, 1589

Stello D., et al., 2015, [ApJ](#), **809**, L3

Stello D., et al., 2016, [ApJ](#), **832**, 133

Stello D., et al., 2017, [ApJ](#), **835**, 83

Straniero O., Chieffi A., Salaris M., 1992, Mem. Soc. Astron. Italiana, **63**, 315

Sweigart A. V., Greggio L., Renzini A., 1990, [ApJ](#), **364**, 527

Tang J., Bressan A., Rosenfield P., Slemmer A., Marigo P., Girardi L., Bianchi L., 2014, [MNRAS](#), **445**, 4287

Tassoul M., 1980, [ApJS](#), **43**, 469

Tayar J., et al., 2017, [ApJ](#), **840**, 17

Thomas H.-C., 1967, [ZAp](#), **67**, 420

Townsend R. H. D., Teitler S. A., 2013, [MNRAS](#), **435**, 3406

Trampedach R., Stein R. F., Christensen-Dalsgaard J., Nordlund Å., Asplund M., 2014, [MNRAS](#), **445**, 4366

Troisi F., et al., 2011, [PASP](#), **123**, 879

Ulrich R. K., 1986, [ApJ](#), **306**, L37

Vandakurov Y. V., 1967, [AZh](#), **44**, 786

VandenBerg D. A., Bergbusch P. A., Dowler P. D., 2006, [The Astrophysical Journal Supplement Series](#), **162**, 375

- VandenBerg D. A., Brogaard K., Leaman R., Casagrande L., 2013, [ApJ](#), **775**, 134
- Vrard M., et al., 2015, [A&A](#), **579**, A84
- White T. R., Bedding T. R., Stello D., Christensen-Dalsgaard J., Huber D., Kjeldsen H., 2011, [ApJ](#), **743**, 161
- Yu J., Huber D., Bedding T. R., Stello D., Hon M., Murphy S. J., Khanna S., 2018, [ApJS](#), **236**, 42
- Zhang H., de Grijs R., Li C., Wu X., 2018, [ApJ](#), **853**, 186
- Zinn J. C., 2021, [AJ](#), **161**, 214
- Zinn J. C., Pinsonneault M. H., Huber D., Stello D., 2019, [ApJ](#), **878**, 136
- Zoccali M., Cassisi S., Piotto G., Bono G., Salaris M., 1999, [ApJ](#), **518**, L49

Publications and Contributions

Publications

First Author Publications:

Khan, S., Hall, O. J., Miglio, A., Davies, G. R., Mosser, B., Girardi, L., Montalbán, J.

The Red-giant Branch Bump Revisited: Constraints on Envelope Overshooting in a Wide Range of Masses and Metallicities

The Astrophysical Journal, 2018

Summary: Calibrated the envelope overshooting efficiency using the red-giant branch bump as seen by *Kepler* and APOGEE

[doi:10.3847/1538-4357/aabf90](https://doi.org/10.3847/1538-4357/aabf90), [arXiv:1804.06669](https://arxiv.org/abs/1804.06669)

Khan, S., Miglio, A., Mosser, B. and 15 co-authors

New light on the Gaia DR2 parallax zero-point: influence of the asteroseismic approach, in and beyond the Kepler field

Astronomy & Astrophysics, 2019

Summary: Constrained biases in the asteroseismic and *Gaia* DR2 parallaxes in the *Kepler* and *K2* fields

[doi:10.1051/0004-6361/201935304](https://doi.org/10.1051/0004-6361/201935304), [arXiv:1904.05676](https://arxiv.org/abs/1904.05676)

Contributing Author Publications:

Hall, O. J., Davies, G. R., Elsworth, Y. P. and 8 co-authors including **Khan, S.**

Testing asteroseismology with Gaia DR2: Hierarchical models of the Red Clump

Monthly Notices of the Royal Astronomical Society, 2019

Contribution: Provided stellar evolutionary tracks and compared results with our independent *Gaia* DR2 study

[doi:10.1093/mnras/stz1092](https://doi.org/10.1093/mnras/stz1092), [arXiv:1904.07919](https://arxiv.org/abs/1904.07919)

Anders, F., Khalatyan, A., Chiappini, C. and 19 co-authors including **Khan, S.**

Photo-astrometric distances, extinctions, and astrophysical parameters for Gaia DR2 stars brighter than $G = 18$

Astronomy & Astrophysics, 2019

Contribution: Provided data for the comparison with asteroseismology

[doi:10.1051/0004-6361/201935765](https://doi.org/10.1051/0004-6361/201935765), [arXiv:1904.11302](https://arxiv.org/abs/1904.11302)

Buldgen, G., Farnir, M., Pezzotti, C. and 10 co-authors including **Khan, S.**

Revisiting Kepler-444. I. Seismic modeling and inversions of stellar structure

Astronomy & Astrophysics, 2019

Contribution: Computed *Gaia* DR2 luminosities

[doi:10.1051/0004-6361/201936126](https://doi.org/10.1051/0004-6361/201936126), [arXiv:1907.10315](https://arxiv.org/abs/1907.10315)

Rendle, B. M., Miglio, A., Chiappini, C. and 21 co-authors including **Khan, S.**

The K2 Galactic Caps Project - going beyond the Kepler field and ageing the Galactic disc

Monthly Notices of the Royal Astronomical Society, 2019

Contribution: Provided *Gaia* DR2 offset values for the *K2* fields

[doi:10.1093/mnras/stz2454](https://doi.org/10.1093/mnras/stz2454), [arXiv:1906.07489](https://arxiv.org/abs/1906.07489)

Miglio, A., Chiappini, C., Mackereth, J. T. and 16 co-authors including **Khan, S.**

Age dissection of the Milky Way discs: Red giants in the Kepler field

Astronomy & Astrophysics, 2021

Contribution: Compared asteroseismic and *Gaia* DR2 parallaxes for the α -rich sample

[doi:10.1051/0004-6361/202038307](https://doi.org/10.1051/0004-6361/202038307), [arXiv:2004.14806](https://arxiv.org/abs/2004.14806)

Mackereth, J. T., Miglio, A., Elsworth, Y. and 30 co-authors including **Khan, S.**

Prospects for Galactic and stellar astrophysics with asteroseismology of giant stars in the TESS continuous viewing zones and beyond

Monthly Notices of the Royal Astronomical Society, 2021

Contribution: Participated in discussions of the work during group meetings

[doi:10.1093/mnras/stab098](https://doi.org/10.1093/mnras/stab098), [arXiv:2012.00140](https://arxiv.org/abs/2012.00140)

Hall, O. J., Davies, G. R., van Saders, J. and 9 co-authors including **Khan, S.**

Weakened magnetic braking supported by asteroseismic rotation rates of Kepler dwarfs

Nature Astronomy, 2021

Contribution: Provided stellar evolutionary tracks

[doi:10.1038/s41550-021-01335-x](https://doi.org/10.1038/s41550-021-01335-x), [arXiv:2104.10919](https://arxiv.org/abs/2104.10919)

Montalbán, J., Mackereth, J. T., Miglio, A. and 16 co-authors including **Khan, S.**

Chronologically dating the early assembly of the Milky Way

Nature Astronomy, 2021

Contribution: Worked on extracting mode parameters from the *Kepler* light-curves

[doi:10.1038/s41550-021-01347-7](https://doi.org/10.1038/s41550-021-01347-7), [arXiv:2006.01783](https://arxiv.org/abs/2006.01783)

Presentations and Posters

The red-giant branch bump, as seen from asteroseismology (*Kepler*, *K2*, *TESS*), photometry of star clusters (*HST*), and astrometry (*Gaia* DR2, EDR3)

Department seminar (invited), Stellar group meeting, 2021
Université de Genève, Switzerland (online)

The red-giant branch bump: towards a better understanding of convective boundary mixing

Contributed poster, Royal Astronomical Society Early Career Poster Exhibition, 2020
Royal Astronomical Society, United Kingdom (online)

Convection in low-mass stars

Contributed poster, Postgraduate Women in Physics Conference, 2020
University of Nottingham, United Kingdom

The RGB bump, from asteroseismology to clusters: towards the validation of new mixing prescriptions

Department seminar, astropizza, 2019
Osservatorio Astronomico di Padova, INAF, Italy

The red-giant branch bump as seen by *Kepler* + APOGEE: constraints on convective boundary mixing in a wide range of masses and metallicities

Contributed poster, Stellar Hydro Days V, 2019
University of Exeter, United Kingdom

New light on the *Gaia* DR2 parallax zero-point: influence of the asteroseismic approach, in and beyond the *Kepler* field

Contributed Talk, 53rd ESLAB symposium: the Gaia universe, 2019
ESTEC/ESA, The Netherlands

New light on the *Gaia* DR2 parallax zero-point: influence of the asteroseismic approach, in and beyond the *Kepler* field

asterochronometry (ERC) kick-off meeting, 2019
University of Birmingham, United Kingdom

New light on the *Gaia* DR2 parallax zero-point: influence of the asteroseismic approach, in and beyond the *Kepler* field

Action Fédératrice Etoile (AFE) day, 2018
Observatoire de Paris, France

The Red-Giant Branch Bump Revisited: Constraints on Envelope Overshooting in a Wide Range of Masses and Metallicities

Contributed talk, TASC4/KASC11 workshop: First Light in a new Era of Astrophysics, 2018

Aarhus University, Denmark

The Red-Giant Branch Bump Revisited: Constraints on Envelope Overshooting in a Wide Range of Masses and Metallicities

Department seminar, LESIA Pôle Etoile, 2018

Observatoire de Paris, France